

VOLUME 13

NUMBER 1

2022

ISSN 2218-7987
eISSN 2409-5508

International Journal of
Mathematics
and **Physics**



Al-Farabi Kazakh National University

The International Journal of Mathematics and Physics is a peer-reviewed international journal covering all branches of mathematics and physics. The Journal welcomes papers on modern problems of mathematics and physics, in particular, Applied Mathematics, Algebra, Mathematical Analysis, Differential Equations, Mechanics, Informatics, Mathematical Modeling, Applied Physics, Radio Physics, Thermophysics, Nuclear Physics, Nanotechnology, and etc.

International Journal of Mathematics and Physics is published twice a year by al-Farabi Kazakh National University, 71 al-Farabi ave., 050040, Almaty, Kazakhstan
website: <http://ijmph.kaznu.kz/>

Any inquiry for subscriptions should be send to:
Prof. Tlekkabul Ramazanov, al-Farabi Kazakh National University
71 al-Farabi ave., 050040, Almaty, Kazakhstan
e-mail: Tlekkabul.Ramazanov@kaznu.kz

EDITORIAL

The most significant scientific achievements are attained through joint efforts of different sciences, mathematics and physics are among them. Therefore, publication of the Journal, which shows results of current investigations in the field of mathematics and physics, will allow wider exhibition of scientific problems, tasks and discoveries. One of the basic goals of the Journal is to promote extensive exchange of information between scientists from all over the world. We propose publishing service for original papers and materials of Mathematical and Physical Conferences (by selection) held in different countries and in the Republic of Kazakhstan. Creation of the special International Journal of Mathematics and Physics is of great importance because a vast amount of scientists is willing to publish their articles and it will help to widen the geography of future dissemination. We will also be glad to publish papers of scientists from all the continents.

The Journal will publish experimental and theoretical investigations on Mathematics, Physical Technology and Physics. Among the subject emphasized are modern problems of Applied Mathematics, Algebra, Mathematical Analysis, Differential Equations, Mechanics, Informatics, Mathematical Modeling, Astronomy, Space Research, Theoretical Physics, Plasma Physics, Chemical Physics, Radio Physics, Thermophysics, Nuclear Physics, Nanotechnology, etc.

The Journal is issued on the base of al-Farabi Kazakh National University. Leading scientists from different countries of the world agreed to join the Editorial Board of the Journal. The Journal is published twice a year by al-Farabi Kazakh National University. We hope to receive papers from many laboratories, which are interested in applications of the scientific principles of mathematics and physics and are carrying out researches on such subjects as production of new materials or technological problems.

B. Rysbaiuly¹ , S.D. Alpar^{1*} 

International Information Technology University, Almaty, Kazakhstan,

*e-mail: rapla.natlus@gmail.com

(Received 17 March 2022; received in revised form 23 April 2022; accepted 07 June 2022)

Experimental Data and the Nonlinear Inverse Problem of Heat Transfer

Abstract. In the paper the development a method for finding the nonlinear heat-conducting characteristics of the soil is being presented. Two-layer container complexes have been created, the side faces of which are thermally insulated so that the 1D heat equation can be used. In order not to solve the boundary value problem with a contact discontinuity and lose the accuracy of the method's solution, a temperature sensor was placed at the junction of two media, and a mixed boundary value problem is solved in each area (container). To provide the initial data with an inverse coefficient problem, two temperature sensors are used: one sensor was placed at the open boundary of the container and recorded the soil temperature at this boundary, and the second sensor was placed at a short distance from the boundary, which recorded the air temperature. The measurements were carried out on the time interval $(0, t_{\max})$. First, the initial-boundary value problem of thermal conductivity with nonlinear coefficients of thermal conductivity, heat capacity, heat transfer, and material density are studied numerically. The nonlinear initial-boundary value problem is solved by the finite difference method. Based on the measured data of the complex, special functionals are constructed and the thermal conductivity coefficient k , density ρ , specific heat capacity c , heat transfer coefficient h are found, which depend on the temperature of the material. Based on the experimentally measured data, the corresponding functional is minimized on each time interval using the gradient descent method. All thermophysical characteristics for a container with clay were found with a relative error of 5%.

Key words: thermal conductivity, nonlinearity, difference problem, iteration, convergence, inverse problem.

Introduction

Heat transfer processes are one of the main sections of modern science and are of great practical importance in industrial energy. Determining the parameters of heat protection systems and obtaining a solution to the problem of thermal design are directly related to the calculations of thermal fields in the soil and ground. In turn, this requires knowledge of the thermophysical characteristics of the soil [1, 2]. The thermophysical properties of the soil play an essential role in the structure of the thermal field of the earth's crust. At the same time, the thermal field of the Earth is largely determined by the processes associated with prospecting, exploration, development of oil, gas and thermal water deposits, operation of main oil and gas pipelines and underground storage facilities. Optimization and analysis of thermal and moisture characteristics of building components is an important engineering tool [3]. In addition, studies of the thermophysical

parameters of soil are of great importance in the gas industry for solving thermodynamic problems related to temperature forecasting when drilling deep and ultra-deep wells, calculating gas reserves, predicting the temperature of fluids at the mouth of production wells, assessing reservoir filtration parameters, and thermal treatment. productive horizons, as well as for transportation and underground storage of gas [4]. Nowadays, theoretical models for finding the thermophysical characteristics of inhomogeneous composite media do not have sufficient accuracy. Therefore, the main source of information about thermophysical properties is the performance of a physical experiment [5,6]. For the theoretical basis of the method for finding the thermophysical characteristics of a medium, the law of conservation of energy is used, the consequence of which is a nonlinear differential equation of heat conduction [1, 7, 8]. Where the thermal conductivity coefficient χ , density ρ , specific heat capacity c , heat transfer coefficient h depends on the temperature of the

material and determine the process of heat transfer in the medium. Temperature is one of the main factors affecting the thermal conductivity of the soil. It has been established that the nature of the influence of temperature on the thermophysical parameters of the soil-soil is nonlinear [9-11]. In this regard, there is an urgent need to solve the inverse problem of the nonlinear heat equation.

Therefore, the purpose of the study is to conduct a thermophysical experiment and develop methodological support for determining thermophysical coefficients based on solving a nonlinear inverse problem of heat conduction [12, 13]. On the basis of the above mathematical model, the direct problem of heat transfer by input parameters is solved. Then the temperature field in the medium or in the material is determined. The physical-mathematical model and experimental temperature values at the accessible soil-ground boundary make it possible to find thermophysical characteristics in inverse coefficient problems of heat transfer [14-16]. The difficulty here is that the experimental temperature data are obtained from unknown thermophysical characteristics, which are calculated in the inverse problem with a predetermined accuracy. In addition, it should be taken into account that the initial approximations of the thermophysical coefficients specified in the iterative algorithm can differ significantly (several times) from the true values used to measure the experimental temperature data. On this basis, it is necessary to develop such algorithms that would eventually give almost zero functional discrepancy even with a significant deviation of the initial values of the unknown thermophysical characteristics from the true ones [17]. It is also necessary to verify the stability of the algorithm [18-21]. In turn, in this study, based on the nonlinear heat equation and experimental data, a method for solving the inverse nonlinear coefficient problem is proposed. The basis of the method is the minimization of the quadratic residual functional between numerical and experimental temperature values. Minimization of the functional is carried out by the method of gradient descent. When determining the damping factor (descent step), the fastest descent method is used.

The article is organized as follows: Section 2 presents a demonstration of a mathematical model for describing the physical phenomenon of heat conduction. The discretization of the computational domain and the model is also shown. Section 3 provides a description of the experiment,

characteristics and installation of the experimental equipment. The soil, consisting of two layers, soil 1 and soil 2, is in a controlled environment – a thermally insulated container. The end faces of the container from the inner side are in contact with the soil, and the outer sides are directed to the boundary condition, which depends on the environment. In Section 4, the reliability of numerical predictions is assessed by comparing them with experimental observations. The description of the obtained results is given, and the graphs of the obtained data are shown.

Mathematical model

Formulation of the problem. Figure 1 illustrates a two-layer container, the side faces of which are thermally insulated, and the end faces are in contact with the environment (air). Considering these limitations, instead of the three-dimensional heat equation, we can consider the one-dimensional non-stationary equation

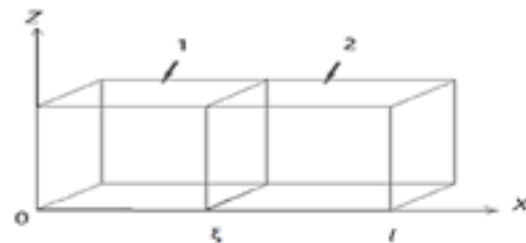


Figure 1 – Two-layer container

$$c(u)\rho(u)\frac{\partial u}{\partial t} = \frac{\partial}{\partial x}\left(k(u)\frac{\partial u}{\partial x}\right),$$

$$x \in (0, \xi) \times (\xi, l), t \in (0, 4t_{\max})$$

The ambient temperature at the left boundary of the region at $x = 0$ will be denoted by $u_{ins}(t)$, and at the right boundary at $x = l$ we will denote by $u_{out}(t)$. In engineering calculations, the parameters c , ρ and k are usually considered to be constants. However, many scientists conclude that the study of nonlinear processes is of great practical interest. Since most processes occurring in nature are nonlinear. Taking into account the nonlinearity of equation greatly complicates the mathematical formulation of the problem. Denote by $u(x, t)$ – distribution the temperature inside the complex containers, where x - is the coordinate of the complex along the Ox axis, t -is the current time. At the initial

time of observation, the temperature of both layers of the body is: $t = 0, u(x, 0) = u_0(x), x \in (0, l)$.

The boundary conditions that determine the features of the process on the wall surface are given as follows:

The left and right boundaries of the region $\Omega = (0, \xi) \times (\xi, l)$ are in contact with the gaseous medium (air), so it is advisable to formulate a boundary condition of the third kind on these boundaries – the relationship between the heat flux due to thermal conductivity from a solid wall and the heat flux from a gaseous medium. Thus, the boundary conditions on the left and right boundaries are written as follows:

$$x = 0: k_1(u) \frac{\partial u}{\partial x} = h_{ins}(u)(u - u_{ins}(t)),$$

$$x = l: k_2(u) \frac{\partial u}{\partial x} = -h_{out}(u)(u - u_{out}(t)),$$

where $u_{ins}(t), u_{out}(t)$ – are ambient temperatures; $h_{ins}(u), h_{out}(u)$ – heat transfer coefficients; $k_1(u), k_2(u)$ – thermal conductivity coefficients of the medium "1" and "2" (Figure 1).

Usually, on the contact surface of the layers $x = \xi$ a boundary condition is set that determines the equality of temperatures and heat fluxes at the junction of materials:

$$\begin{aligned} u_1(\xi, t) &= u_2(\xi, t), \\ k_1(u) \frac{\partial u_1}{\partial x}(\xi, t) &= k_2(u) \frac{\partial u_2}{\partial x}(\xi, t). \end{aligned} \quad (1)$$

Here $u_1(x, t)$ и $u_2(x, t)$ – are the temperatures of the material layers in contact. When solving problems with contact conditions of the form (1), the rate of convergence of a homogeneous difference scheme becomes very low [19]. Therefore, to avoid this problem, we placed a separate sensor at the point $x = \xi$ which measures the change in soil temperature at the point of contact of two media. Due to this, the original task is split into two tasks, i.e. using the measured data in each container, its own problem of nonlinear thermal conductivity is solved. In the future, we will state the problem only on the left container shown in Fig.1.

In addition to $u_{ins}(t), u_{out}(t)$, the initial temperature values $T_\xi(t), t \in [0, t_{max}]$. For

convenience of notation, we introduce the notation $h_{ins}(u) = h_1(u)$.

Problem. Using the measured values $u_{ins}(t), T_{ins}(t), T_\xi(t), t \in [0, t_{max}]$, it is required to develop a method for finding the temperature $u(x, t)$ and all the thermophysical parameters of the soil.

In the region of $Q_1 = (0, \xi) \times (0, t_{max})$ we studied the following system of equations.

$$c_1(u)\rho_1(u) \frac{\partial u}{\partial t} = \frac{\partial}{\partial x} \left(k_1(u) \frac{\partial u}{\partial x} \right),$$

$$u(x, 0) = u_0(x),$$

$$k_1(u) \frac{\partial u}{\partial x} = h_1(u)(u - u_{ins}(t)), x = 0,$$

$$u(\xi, t) = T_\xi(t).$$

Grid method. Section $(0, \xi)$ is divided into I equal parts with a step $\Delta x = \xi/I$. Then $\xi = I\Delta x$, where I - is the node number of the contact point $x = \xi$. And the segment $(0, t_{max})$ is divided into m equal parts with $\Delta t = t_{max}/m$.

As a result of this action, we get a grid:

$$\omega = \{x_i = i\Delta x, t_j = j\Delta t; i = 0, 1, \dots, I; j = 0, 1, \dots, m\},$$

In the present work, a method has been developed for finding the soil parameters $k_s(u), c_s(u), \rho_s(u), h_s(u), s = 1, 2$. In this case, the measured values of the ambient temperature are used as initial information $u_{ins}(t), u_{out}(t)$ и $u_0(t)$ – initial temperature distribution at time $t = 0$. And also $T_\xi(t)$ – soil temperature at the contact point of two media $x = \xi$. To compile the functional, $T_{ins}(t), T_{out}(t)$ – measured values of soil temperature at the boundary of the considered area are used.

Development of iteration methods

In the grid region ω the difference scheme is studied:

$$\rho_1(u_i^{j+1}) \cdot c_1(u_i^{j+1}) \frac{u_i^{j+1} - u_i^j}{\Delta t} = \frac{1}{\Delta x} \left(k_1 \left(u_{i+\frac{1}{2}}^{j+1} \right) \frac{u_{i+\frac{1}{2}}^{j+1} - u_i^{j+1}}{\Delta x} - k_1 \left(u_{i-\frac{1}{2}}^{j+1} \right) \frac{u_i^{j+1} - u_{i-\frac{1}{2}}^{j+1}}{\Delta x} \right),$$

$$i = 1, 2, \dots, I - 1; j = 0, 1, \dots, m - 1;$$

$$u_i^0 = u_0(x_i), i = 0, 1, \dots, I; \tag{2}$$

$$u_i^{j+1} = T_\xi(t_{j+1}), j = 0, 1, \dots, m - 1;$$

$$k_1 \left(u_{\frac{1}{2}}^{j+1} \right) \frac{u_1^{j+1} - u_0^{j+1}}{\Delta x} = h_1 \left(u_0^{j+1} \right) \left(u_0^{j+1} - u_{\text{ins}}^{j+1} \right);$$

where

$$u_{i+\frac{1}{2}}^{j+1} = \frac{u_{i+1}^{j+1} + u_i^{j+1}}{2}, i = 0, 1, \dots, I - 1.$$

Let's rewrite difference equation of the system (2) in the form:

$$\begin{aligned} F(u_{i+1}^{j+1}, u_i^{j+1}, u_{i-1}^{j+1}) &\equiv Z \cdot \left(k \left(u_{i+\frac{1}{2}}^{j+1} \right) (u_{i+1}^{j+1} - u_i^{j+1}) - k \left(u_{i-\frac{1}{2}}^{j+1} \right) (u_i^{j+1} - u_{i-1}^{j+1}) \right) - \\ &\quad - \rho(u_i^{j+1}) c(u_i^{j+1}) (u_i^{j+1} - u_i^j) = 0, \\ i &= 1, 2, \dots, I - 1; j = 0, 1, \dots, m - 1 \end{aligned}$$

where $Z = \frac{\Delta t}{(\Delta x)^2}$.

Let's $x^s = (u_{i+1}^{s,j+1}, u_i^{s,j+1}, u_{i-1}^{s,j+1})$.

When $s = 0, x^0$ will be the initial approximation of the system (3). Then, applying the Newton method for system (3), the following approximation of the unknown grid function is obtained:

$$\frac{\partial F(x^s)}{\partial u_{i+1}^{j+1}} (u_{i+1}^{s+1,j+1} - u_{i+1}^{s,j+1}) + \frac{\partial F(x^s)}{\partial u_i^{j+1}} (u_i^{s+1,j+1} - u_i^{s,j+1}) + \frac{\partial F(x^s)}{\partial u_{i-1}^{j+1}} (u_{i-1}^{s+1,j+1} - u_{i-1}^{s,j+1}) + F(x^s) = 0 \tag{4}$$

where s – iteration's number for the Newton's method.

Expanding the brackets, (4) is reduced to tridiagonal system:

$$A_i (u_{i+1}^{j+1})^{s+1} + B_i (u_i^{j+1})^{s+1} + C_i (u_{i-1}^{j+1})^{s+1} = D_i^s, \\ i = 1, \dots, N - 1; j = 0, \dots, m - 1,$$

where the coefficients are equal:

$$A_i = \frac{\partial F(x^s)}{\partial u_{i+1}^{j+1}}, B_i = \frac{\partial F(x^s)}{\partial u_i^{j+1}}, C_i = \frac{\partial F(x^s)}{\partial u_{i-1}^{j+1}},$$

$$D_i^s = -F(x^s) + A_i (u_{i+1}^{j+1})^s + B_i (u_i^{j+1})^s + C_i (u_{i-1}^{j+1})^s$$

Then, expanding equation (3), the corresponding derivatives were found:

$$\begin{aligned} F(u_{i+1}^{j+1}, u_i^{j+1}, u_{i-1}^{j+1}) &= \\ &= \left[k_0 + k_1 \left(u_{i+\frac{1}{2}}^{j+1} \right) + k_2 \left(u_{i+\frac{1}{2}}^{j+1} \right)^2 + k_3 \left(u_{i+\frac{1}{2}}^{j+1} \right)^3 \right] \cdot (u_{i+1}^{j+1} - u_i^{j+1}) Z - \end{aligned}$$

$$\begin{aligned}
& - \left[k_0 + k_1 \left(u_{i-\frac{1}{2}}^{j+1} \right) + k_2 \left(u_{i-\frac{1}{2}}^{j+1} \right)^2 + k_3 \left(u_{i-\frac{1}{2}}^{j+1} \right)^3 \right] \cdot \\
& \cdot (u_i^{j+1} - u_{i-1}^{j+1})Z - c(u_i^{j+1})\rho(u_i^{j+1})(u_i^{j+1} - u_i^j) = 0, \quad i = 1, \dots, I-1, \\
\frac{\partial F}{\partial u_{i+1}^{j+1}} &= Z \cdot \left[\frac{3k_3}{2} \left(u_{i+\frac{1}{2}}^{j+1} \right)^2 + k_2 \left(u_{i+\frac{1}{2}}^{j+1} \right) + \frac{k_1}{2} \right] \cdot (u_{i+1}^{j+1} - u_i^{j+1}) + Z \cdot k \left(u_{i+\frac{1}{2}}^{j+1} \right), \\
\frac{\partial F}{\partial u_i^{j+1}} &= Z \cdot \left[\frac{3k_3}{2} \left(u_{i+\frac{1}{2}}^{j+1} \right)^2 + k_2 \left(u_{i+\frac{1}{2}}^{j+1} \right) + \frac{k_1}{2} \right] (u_{i+1}^{j+1} - u_i^{j+1}) - \\
& - Z \cdot k \left(u_{i+\frac{1}{2}}^{j+1} \right) - Z \cdot \left[\frac{3k_3}{2} \left(u_{i-\frac{1}{2}}^{j+1} \right)^2 + k_2 \left(u_{i-\frac{1}{2}}^{j+1} \right) + \frac{k_1}{2} \right] \cdot \\
& \cdot (u_i^{j+1} - u_{i-1}^{j+1}) - Z \cdot k \left(u_{i-\frac{1}{2}}^{j+1} \right) - \frac{\partial c}{\partial u_i^{j+1}} \rho(u_i^{j+1})(u_i^{j+1} - u_i^j) - \\
& - \frac{\partial \rho}{\partial u_i^{j+1}} c(u_i^{j+1})(u_i^{j+1} - u_i^j) - \rho(u_i^{j+1})c(u_i^{j+1}), \\
\frac{\partial F}{\partial u_{i-1}^{j+1}} &= -S \cdot \left[\frac{3k_3}{2} \left(u_{i-\frac{1}{2}}^{j+1} \right)^2 + k_2 \left(u_{i-\frac{1}{2}}^{j+1} \right) + \frac{k_1}{2} \right] (u_i^{j+1} - u_{i-1}^{j+1}) + S \cdot k \left(u_{i-\frac{1}{2}}^{j+1} \right),
\end{aligned}$$

Similarly, the boundary conditions are revealed, considering the dependence of the thermal conductivity and heat transfer coefficient on temperature:

$$k \left(u_{\frac{1}{2}}^{j+1} \right) \frac{u_1^{j+1} - u_0^{j+1}}{\Delta x} = h(u_0^{j+1})(u_0^{j+1} - u_{ins}^{j+1}).$$

Let's rewrite it in the form:

$$\frac{\partial H(u_0^{j+1,s}, u_1^{j+1,s})}{\partial u_0^{j+1}} (u_0^{j+1,s+1} - u_0^{j+1,s}) + \frac{\partial H(u_0^{j+1,s}, u_1^{j+1,s})}{\partial u_1^{j+1}} (u_1^{j+1,s+1} - u_1^{j+1,s}) + H(u_0^{j+1,s}, u_1^{j+1,s}) = 0.$$

Let's expand the derivatives in the following form:

$$\frac{\partial H(u_0^{j+1,s}, u_1^{j+1,s})}{\partial u_0^{j+1}} = D_0 = \frac{\partial k}{\partial u_0^{j+1}} \cdot \frac{u_1^{j+1} - u_0^{j+1}}{\Delta x} - \frac{k \left(u_{\frac{1}{2}}^{j+1} \right)}{\Delta x} - \frac{\partial h}{\partial u_0^{j+1}} (u_0^{j+1} - u_{ins}^{j+1}) - h(u_0^{j+1}),$$

where

$$\frac{\partial k}{\partial u_0^{j+1}} = \frac{3k_3}{2} \left(u_{\frac{1}{2}}^{j+1}\right)^2 + k_2 \cdot u_{\frac{1}{2}}^{j+1} + \frac{k_1}{2}$$

$$\frac{\partial h}{\partial u_0^{j+1}} = h_1.$$

$$\frac{\partial H(u_0^{j+1,s}, u_1^{j+1,s})}{\partial u_1^{j+1}} = E_0 = \frac{\partial k}{\partial u_1^{j+1}} \cdot \frac{u_1^{j+1} - u_0^{j+1}}{\Delta x} + \frac{k \left(u_{\frac{1}{2}}^{j+1}\right)}{\Delta x},$$

where

$$\frac{\partial k}{\partial u_1^{j+1}} = \frac{3k_3}{2} \left(u_{\frac{1}{2}}^{j+1}\right)^2 + k_2 \cdot u_{\frac{1}{2}}^{j+1} + \frac{k_1}{2}.$$

We find the initial values for the recursive formula of the Thomas method:

$$D_0 u_0^{j+1,s+1} - D_0 u_0^{j+1,s} + E_0 u_1^{j+1,s+1} - E_0 u_1^{j+1,s} + H(u_0^{j+1,s}, u_1^{j+1,s}) = 0,$$

$$u_0^{j+1,s+1} = \frac{-E_0 u_1^{j+1,s+1}}{D_0} + u_0^{j+1,s} + \frac{E_0 u_1^{j+1,s}}{D_0} -$$

$$- \frac{H(u_0^{j+1,s}, u_1^{j+1,s})}{D_0}.$$

From here we get

$$\alpha_1 = \frac{-E_0}{D_0},$$

$$\beta_1 = u_0^{j+1,s} + \frac{E_0 u_1^{j+1,s}}{D_0} - \frac{H(u_0^{j+1,s}, u_1^{j+1,s})}{D_0}.$$

Differentiation with respect to a parameter

1) In the area $(0, \xi) \times (0, t_{max})$ the discrete problem is solved

$$\rho_1(u_i^{j+1}) \cdot c_1(u_i^{j+1}) u_{i,\bar{t}}^{j+1} = \left(k_1 \left(u_{i+\frac{1}{2}}^{j+1}\right) u_{i\bar{x}}^{j+1}\right)_{\bar{x}}$$

$$i = 1, 2, \dots, I - 1, j = 0, 1, \dots, m - 1, u_i^0 = u_0(x_i), i = 0, 1, \dots, I, \tag{5}$$

$$u_i^{j+1} = T_{\xi}(t_{j+1}), j = 0, 1, \dots, m - 1$$

$$k_1 \left(u_{\frac{1}{2}}^{j+1}\right) u_{1\bar{x}}^{j+1} = h_1(u_0^{j+1})(u_0^{j+1} - u_{ins}^{j+1}), j = 0, 1, \dots, m - 1.$$

We consider that the coefficient $k_1(u)$ is represented as

$$k_1(u) = k_{10} + k_{11}u + k_{12}u^2 + k_{13}u^3.$$

Assuming that the solution to problem (4) continuously depends on $k_1(u)$ and has a derivative with respect to $k_1(u)$, we differentiate system (4) with respect to the parameter

$$k_{1s}(u), s = 0, 1, 2, 3$$

Let's denote

$$\frac{\partial u_i^{j+1}}{\partial k_{1s}} = y_i^{j+1}(s), i = 0, 1, \dots, I,$$

$$j = 0, 1, \dots, m - 1, s = 0, 1, 2, 3$$

Then

$$\begin{aligned} \frac{\partial \rho_1(u_i^{j+1})}{\partial k_{1s}} &= \rho'_1(u_i^{j+1})y_i^{j+1}(s), \\ \frac{\partial c(u_i^{j+1})}{\partial k_{1s}} &= c'_1(u_i^{j+1})y_i^{j+1}(s), \\ \frac{\partial k_1(u_i^{j+1})}{\partial k_{1s}} &= (u_i^{j+1})^s + k'_1(u_i^{j+1})y_i^{j+1}(s), \end{aligned}$$

$$\frac{\partial h_1(u_0^{j+1})}{\partial k_{1s}} = h'_1(u_0^{j+1})u_0^{j+1}(s).$$

After differentiating system (4) with respect to $k_{1s}, s = 0,1,2,3$, various problems follow depending on s . These tasks can be written in a single form as follows

$$\begin{aligned} [c'_1(u_i^{j+1})\rho_1(u_i^{j+1}) + \rho'_1(u_i^{j+1})c_1(u_i^{j+1})] y_i^{j+1}(s) u_{i,\bar{t}}^{j+1} + c_1(u_i^{j+1})\rho_1(u_i^{j+1})y_{i,\bar{t}}^{j+1}(s) = \\ = \left[k_1 \left(u_{i+\frac{1}{2}}^{j+1} \right) y_{ix}^{j+1}(s) \right]_{\bar{x}} + \left[\left(\left(u_{\frac{1}{2}}^{j+1} \right)^s + k'_1 \left(u_{i+\frac{1}{2}}^{j+1} \right) \frac{y_{i+1}^{j+1}(s) + y_i^{j+1}(s)}{2} \right) u_{i,\bar{x}}^{j+1} \right]_{\bar{x}} \end{aligned}$$

$$i = 1,2 \dots, I - 1, = 0,1, \dots, m - 1,$$

$$y_i^0 = 0, i = 0,1, \dots, I, u_i^{j+1} = 0, j = 0,1, \dots, m - 1,$$

$$\begin{aligned} k_1 \left(u_{\frac{1}{2}}^{j+1} \right) y_{1,x}^{j+1}(s) + \left(\left(u_{\frac{1}{2}}^{j+1} \right)^s + k'_1 \left(u_{\frac{1}{2}}^{j+1} \right) \frac{y_1^{j+1}(s) + y_0^{j+1}(s)}{2} \right) u_{1,\bar{x}}^{j+1} = \\ = h'_1(u_0^{j+1})(u_0^{j+1} - u_{ins}^{j+1}) + h_1(u_0^{j+1})y_0^{j+1}(s), j = 0,1, \dots, m - 1. \end{aligned}$$

The values of the coefficients $k_{1s}, s = 0,1,2,3$ of the coefficient of thermal conductivity of soil $k_1(u)$ will be found from the condition of the minimum of the functional

$$J(k_1(u)) = \sum_{j=0}^{m-1} (u_0^{j+1}(k_1) - T_0^{j+1})^2 \Delta t$$

Direct differentiation of the last equality with respect to $k_{1s}, s = 0,1,2,3$ gives us the gradient of the composed functional written as

$$\begin{aligned} \nabla J(k_{1s}) = \\ = 2 \sum_{j=0}^{m-1} (u_0^{j+1}(k_1) - T_0^{j+1})y_0^{j+1}(s)\Delta t, \\ s = 0,1,2,3. \end{aligned} \tag{6}$$

Then

$$J(k_1(u)) = \sum_{s=0}^3 J(k_{1s})$$

Knowing the explicit expression for the gradient of the functional, the parameters of the functions $k_1(u)$ are defined as follows

$$\begin{aligned} k_{1s}(n+1) &= k_{1s}(n) + \mu_1(s)\nabla J(k_{1s}(n)), = \\ &= 0,1,2,3. \end{aligned}$$

To determine the damping factor $\mu_1(s)$ of the functional

$$\begin{aligned} J(k_{1s}(n+1)) &= \\ &= \sum_{j=0}^{m-1} (u_0^{j+1}(k_{1s}(n+1)) - T_0^{j+1})^2 \Delta t. \end{aligned}$$

Minimize by parameter $\mu_1(s)$. For this we use the expansion

$$\begin{aligned} u_0^{j+1}(k_{1s}(n+1)) &= \\ &= u_0^{j+1}(k_{1s}(n)) + \mu_1(s)\nabla J(k_{1s}(n)) = \\ &= u_0^{j+1}(k_{1s}(n)) + \end{aligned}$$

$$+ \frac{\partial u_0^{j+1}(k_{1s}(n))}{\partial k_{1s}} \mu_1(s) \nabla J(k_{1s}(n)) + o(\mu_1(s))^2.$$

Using this expansion from (6) after some transformations, we obtain the parameter of the fastest descent in the form:

$$\begin{aligned} \mu_1(s) &= \\ &= - \frac{\sum_{j=0}^{m-1} (u_0^{j+1}(k_{1s}(n)) - T_0^{j+1}) y_0^{j+1}(s) \Delta t}{\sum_{j=0}^{m-1} (y_0^{j+1})^2 \Delta t \nabla J(k_{1s}(n))}, \\ s &= 0, 1, 2, 3. \end{aligned} \tag{7}$$

Using (7), we write out the final calculation formula for each coefficient of the function $k_1(u)$ in the following form

$$\begin{aligned} k_{1s}(n+1) &= k_{1s}(n) - \\ &- \frac{\sum_{j=0}^{m-1} (u_0^{j+1}(k_{1s}(n)) - T_0^{j+1}) y_0^{j+1}(s) \Delta t}{\sum_{j=0}^{m-1} (y_0^{j+1})^2 \Delta t}, \\ s &= 0, 1, 2, 3. \end{aligned}$$

2) To determine the specific heat coefficient $c_1(u)$ we represent it as

$$c_1(u) = c_{10} + c_{11}u.$$

This is the most commonly used dependence in practice [1].

Now the discrete problem is composed in the region $(0, \xi) \times (t_{max}, 2t_{max})$ and has the form

$$\begin{aligned} \rho_1(u_i^{j+1}) \cdot c_1(u_i^{j+1}) u_{i,\bar{t}}^{j+1} &= \\ &= \left(k_1 \left(u_{i+\frac{1}{2}}^{j+1} \right) u_{ix}^{j+1} \right)_{\bar{x}}, \end{aligned}$$

$$i = 1, 2, \dots, I-1, j = m, m+1, \dots, 2m-1,$$

$u_i^m = u_0(x_i)$ – solution of problem (5) for $j = m-1, i = 0, 1, \dots, I,$

$$u_i^{j+1} = T_\xi(t_{j+1}), \quad j = m, m+1, \dots, 2m-1, \tag{8}$$

$$k_1 \left(u_{\frac{1}{2}}^{j+1} \right) u_{1\bar{x}}^{j+1} = h_1(u_0^{j+1})(u_0^{j+1} - u_{ins}^{j+1}),$$

$$j = m, m+1, \dots, 2m-1.$$

In this case, all the coefficients of the functions $\rho_1(u)$, $k_1(u)$ and $h_1(u)$ are taken from the current iteration level, and the coefficients of the function $c_1(u)$ are changed, calculating the minimum of the functional

$$\begin{aligned} J(c+1(u)) &= \sum_{j=m}^{2m-1} (u_0^{j+1}(c_1) - T_0^{j+1})^2 \Delta t = \\ &= J(c_{10}(u)) + J(c_{11}(u)) = \\ &= \sum_{j=m}^{2m-1} (u_0^{j+1}(c_{10}) - T_0^{j+1})^2 \Delta t + \\ &+ \sum_{j=m}^{2m-1} (u_0^{j+1}(c_{11}) - T_0^{j+1})^2 \Delta t. \end{aligned}$$

Assuming the continuous dependence of the solution of the problem u_i^{j+1} on the parameters c_{10} and c_{11} , and, assuming the existence of a derivative of the function u_i^{j+1} with respect to the named parameters, we differentiate (8) with respect to $c_{1s}, s = 0, 1.$

As early as we introduce the notation

$$\begin{aligned} \frac{\partial u_i^{j+1}}{\partial c_{1s}} &= y_i^{j+1}(s), \quad i = 0, 1, \dots, I, \\ j &= m, m+1, \dots, 2m-1, \quad s = 0, 1. \end{aligned}$$

And given that

$$\frac{\partial c_1(u_i^{j+1})}{\partial c_{1s}} = (u_i^{j+1})^s + c_1'(u_i^{j+1}) y_i^{j+1}(s), \quad s = 0, 1.$$

We compose a system with respect to the unknowns $y_i^{j+1}(s)$ in the following form

$$\begin{aligned}
& \left((u_i^{j+1})^s + c_1'(u_i^{j+1})y_i^{j+1}(s) \right) \rho_1(u_i^{j+1})u_{i,\bar{t}}^{j+1} + \rho_1'(u_i^{j+1})y_i^{j+1}(s)c_1(u_i^{j+1})u_{i,\bar{t}}^{j+1} + \\
& + c_1(u_i^{j+1})\rho_1(u_i^{j+1})y_{i,\bar{t}}^{j+1}(s) = \\
& = \left[k_1 \left(u_{i+\frac{1}{2}}^{j+1} \right) y_{ix}^{j+1}(s) \right]_{\bar{x}} + \left[\left(k_1' \left(u_{i+\frac{1}{2}}^{j+1} \right) \frac{y_{i+1}^{j+1}(s) + y_i^{j+1}(s)}{2} \right) u_{ix}^{j+1} \right]_{\bar{x}} \\
& i = 1, 2, \dots, I-1, j = m, m+1, \dots, 2m-1, \\
& y_i^m = 0, \quad i = 0, 1, \dots, I, y_i^{j+1} = 0, j = m, m+1, \dots, 2m-1, \\
& k_1 \left(u_{\frac{1}{2}}^{j+1} \right) y_{1,\bar{x}}^{j+1}(s) + \left(k_1' \left(u_{\frac{1}{2}}^{j+1} \right) \frac{y_1^{j+1}(s) + y_0^{j+1}(s)}{2} \right) u_{1\bar{x}}^{j+1} = \\
& = h_1'(u_0^{j+1})(u_0^{j+1} - u_{ins}^{j+1}) + h_1(u_0^{j+1})y_0^{j+1}(s), j = m, m+1, \dots, 2m-1.
\end{aligned}$$

Here $s = 0, 1$.

Repeating all the calculations done when deriving the calculation formula k_{1s} , we derive the calculation formula for c_{1s} in the following form

$$\begin{aligned}
c_{1s}(n+1) &= c_{1s}(n) - \\
& - \frac{\sum_{j=m}^{2m-1} (u_0^{j+1}(c_{1s}(n)) - T_0^{j+1}) y_0^{j+1}(s, n) \Delta t}{\sum_{j=m}^{2m-1} (y_0^{j+1}(s, n))^2 \Delta t}, \\
& s = 0, 1
\end{aligned}$$

The corresponding functional has the form

$$\begin{aligned}
& \left((u_i^{j+1})^s + \rho_1'(u_i^{j+1})y_i^{j+1}(s) \right) c_1(u_i^{j+1})u_{i,\bar{t}}^{j+1} + c_1'(u_i^{j+1})y_i^{j+1}(s)\rho_1(u_i^{j+1})u_{i,\bar{t}}^{j+1} + \\
& + c_1(u_i^{j+1})\rho_1(u_i^{j+1})y_{i,\bar{t}}^{j+1}(s) = \\
& = \left[k_1 \left(u_{i+\frac{1}{2}}^{j+1} \right) y_{ix}^{j+1}(s) \right]_{\bar{x}} + \left[k_1' \left(u_{i+\frac{1}{2}}^{j+1} \right) \frac{y_{i+1}^{j+1}(s) + y_i^{j+1}(s)}{2} u_{ix}^{j+1} \right]_{\bar{x}} \\
& i = 1, 2, \dots, I-1, j = 2m, m+1, \dots, 3m-1, s = 0, 1, \\
& y_i^{2m} = 0, i = 0, 1, \dots, I; y_i^{j+1} = 0, \quad j = 2m, m+1, \dots, 3m-1
\end{aligned}$$

$$\begin{aligned}
J(c_{1s}(n)) &= \sum_{j=m}^{2m-1} (u_0^{j+1}(c_{1s}(n)) - T_0^{j+1})^2 \Delta t, \\
& s = 0, 1.
\end{aligned}$$

3) Assuming the dependence of the specific density $\rho_1(u)$ in the form

$$\rho_1(u) = \rho_{10} + \rho_{11}u$$

and given that $\frac{\partial u_i^{j+1}}{\partial \rho_{1s}} = y_i^{j+1}(s)$, we compose the corresponding discrete problem. This time in the area $(0, \xi) \times (2t_{max}, 3t_{max})$ in the form

$$k_1 \left(u_{\frac{1}{2}}^{j+1} \right) y_{1,\bar{x}}^{j+1}(s) + \left(k_1' \left(u_{\frac{1}{2}}^{j+1} \right) \frac{y_1^{j+1}(s) + y_0^{j+1}(s)}{2} \right) u_{1\bar{x}}^{j+1} =$$

$$= h_1'(u_0^{j+1})(u_0^{j+1} - u_{ins}^{j+1}) + h_1(u_0^{j+1})y_0^{j+1}(s), \quad j = 2m, m + 1, \dots, 3m - 1.$$

Here $s = 0, 1$.

In this case, to calculate the coefficients $\rho_1(u)$, the formula is derived

$$\rho_{1s}(n + 1) = \rho_{1s}(n) - \frac{\sum_{j=2m}^{3m-1} (u_0^{j+1}(\rho_{1s}(n)) - T_0^{j+1}) y_0^{j+1}(s, n) \Delta t}{\sum_{j=2m}^{3m-1} (y_0^{j+1}(s, n))^2 \Delta t},$$

$s = 0, 1$.

Functional is minimized

$$J(\rho_{1s}(n)) = \sum_{j=2m}^{3m-1} (u_0^{j+1}(\rho_{1s}(n)) - T_0^{j+1})^2 \Delta t,$$

$s = 0, 1$.

4) Calculation of the heat transfer coefficient $h_1(u)$.

In practical calculations, power-law dependences of the heat transfer coefficient on the soil temperature on the contact surface of two media are usually used. We'll look at the dependency:

$$h_1(u) = h_{10} + h_{11}u$$

$$\rho_1'(u_i^{j+1})c_1(u_i^{j+1})y_i^{j+1}(s)u_{i,\bar{t}}^{j+1} + c_1'(u_i^{j+1})\rho_1(u_i^{j+1})y_i^{j+1}(s)u_{i,\bar{t}}^{j+1} + c_1(u_i^{j+1})\rho_1(u_i^{j+1})y_{i,\bar{t}}^{j+1}(s) =$$

$$\left[k_1 \left(u_{i+\frac{1}{2}}^{j+1} \right) y_{ix}^{j+1}(s) \right]_{\bar{x}} + \left(k_1' \left(u_{i+\frac{1}{2}}^{j+1} \right) \frac{y_{i+1}^{j+1}(s) + y_i^{j+1}(s)}{2} \right) u_{ix}^{j+1} \right]_{\bar{x}}$$

$$i = 1, 2, \dots, I - 1; \quad j = 3m, m + 1, \dots, 4m - 1; \quad s = 0, 1,$$

$$y_i^{3m} = 0, i = 0, 1, \dots, I; y_i^{j+1} = 0, j = 3m, m + 1, \dots, 4m - 1,$$

$$k_1 \left(u_{\frac{1}{2}}^{j+1} \right) y_{1,\bar{x}}^{j+1}(s) + \left(k_1' \left(u_{\frac{1}{2}}^{j+1} \right) \frac{y_1^{j+1}(s) + y_0^{j+1}(s)}{2} \right) u_{1\bar{x}}^{j+1} =$$

$$= \left((u_0^{j+1})^s + h_1'(u_0^{j+1})y_0^{j+1}(s) \right) (u_0^{j+1} - u_{ins}^{j+1}) + h_1(u_0^{j+1})y_0^{j+1}(s),$$

$$j = 3m, m + 1, \dots, 4m - 1.$$

Then

$$\frac{\partial h_1(u_i^{j+1})}{\partial h_{1s}} = (u_i^{j+1})^s + h_1'(u_i^{j+1})y_i^{j+1}(s),$$

$s = 0, 1$,

here $\frac{\partial u_i^{j+1}}{\partial h_{1s}} = y_i^{j+1}(s), i = 1, 2, \dots, I - 1, j = 3m, m + 1, \dots, 4m - 1, s = 0, 1.$

In this case, the problem is considered in the area $(0, \xi) \times (3t_{max}, 4t_{max})$ and the next function coefficients are taken from the current iteration level:

$$\rho_1(u), c_1(u) \text{ и } k_1(u).$$

After skipping the difference scheme in the next grid domain

$$\omega_{14} = \{x_l = i\Delta x, t_j = j\Delta t; i = 0, 1, \dots, I; j = 3m, \dots, 4m - 1\},$$

Let us immediately write out the difference problem for the function y_i^{j+1} . The difference scheme has the form

Here $s = 0,1$.

In this case, by controlling the parameters $h_{1s}, s = 0,1$, the functional is minimized

$$J(h_{1s}(n)) = \sum_{j=3m}^{4m-1} (u_0^{j+1}(h_{1s}(n)) - T_0^{j+1})^2 \Delta t,$$

$$s = 0,1.$$

And the control parameters of optimization processes are determined by the formula

$$h_{1s}(n+1) = h_{1s}(n) -$$



Figure 2 – Containers with soil

Containers with sensors were built for the experiment. Photos of containers are shown in Fig. 2. The side faces of the containers are made of 2 cm thermally insulated material, and the end faces are in contact with the environment (air). In each compartment of the container, 15 cm long, there are various soils. One end side is heated with lamps. The second outer side is affected by the ambient temperature.

3 sensors (C2, C3, C4) are evenly distributed inside the material as shown in Figure 1. They measure temperature with an error of 0.3 degrees Celsius according to the technical data sheet of the sensor. In addition to these sensors, there are 2 more sensors (C1, C5) close to the ends to measure the ambient temperature. The errors of these sensors are the same as those of the previous sensors. The temperature data measurement is taken at intervals of 10 minutes.

For calculations, a two-chamber container was considered and, accordingly, with two materials:

$$- \frac{\sum_{j=3m}^{4m-1} (u_0^{j+1}(h_{1s}(n)) - T_0^{j+1}) y_0^{j+1}(s, n) \Delta t}{\sum_{j=3m}^{4m-1} (y_0^{j+1}(s, n))^2 \Delta t},$$

$$s = 0,1.$$

Comment. Everywhere we have assumed that the parameters $\rho_1(u), c_1(u), k_1(u)$ and $h_1(u)$ depend on u in the form of a polynomial. However, the considered method is applicable in another form of dependence on u .

Experimental setup

sand and black soil. The data were measured over a period of three months, and the physical length of the entire container is determined through the interval $x \in (0, l)$, where $l = 30$ cm. The boundary of the two media is at a distance of $x = 15$ cm and the temperature measurement sensor is also located there. Since there is an exchange with the environment at the end boundaries, Robin boundary conditions were considered for the numerical solution. Measurements at points $x = 0$ cm. and $x = 30$ cm determine the temperature at the end boundaries. The temperature values of the measured data can be seen in Fig. 3.

It should be noted that enough time has passed to conduct numerical experiments (about 3 months) from the installation of measuring instruments and the data used in the proposed article. Also, for the initial condition, the interpolation of the measured data was taken.

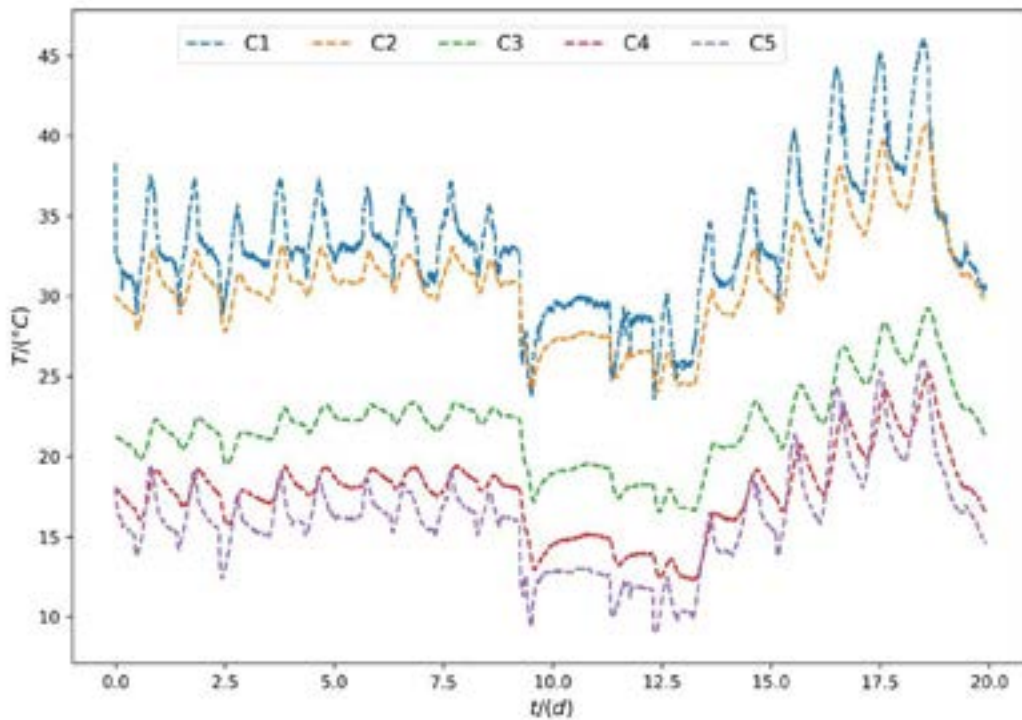


Figure 3 – Containers with soil

Results

The measured temperature data were used to solve a numerical problem to find all thermophysical coefficients (thermal conductivity coefficient, specific heat capacity, specific density and heat transfer coefficient). Thanks to the steepest descent method, the functionals converge fairly quickly and reach a minimum in 6 and 7 iterations. The minimization of the functional continued until the relative error between the nonlinear solution and the experimental data reached $\sim 4.3\%$ for chernozem and $\sim 3.12\%$ for sand, which in turn shows a fairly good accuracy of the solution. If we look at the absolute errors in two environments – $\sim 6.3\%$ and $\sim 5.3\%$, we see that they also meet our expectations.

In addition, the values of the coefficients at the contact boundary of two media were

considered. Figure 4 illustrates the values of thermal conductivity, density, specific heat capacity and volumetric heat capacity from the left approximation (sand) and the right approximation (soil) to the boundary. As can be seen from the graph, the values of the coefficients at the contact discontinuity differ significantly from each other, but in the case of the volumetric heat capacity coefficient, the values at many points coincide at the boundary of two media, which can prove a continuous volumetric heat capacity at the boundary of two different media. This statement needs further research on other materials. The large difference at the initial points in time is associated with a rough initial approximation of the iterative process for the parameters of thermophysical coefficients.

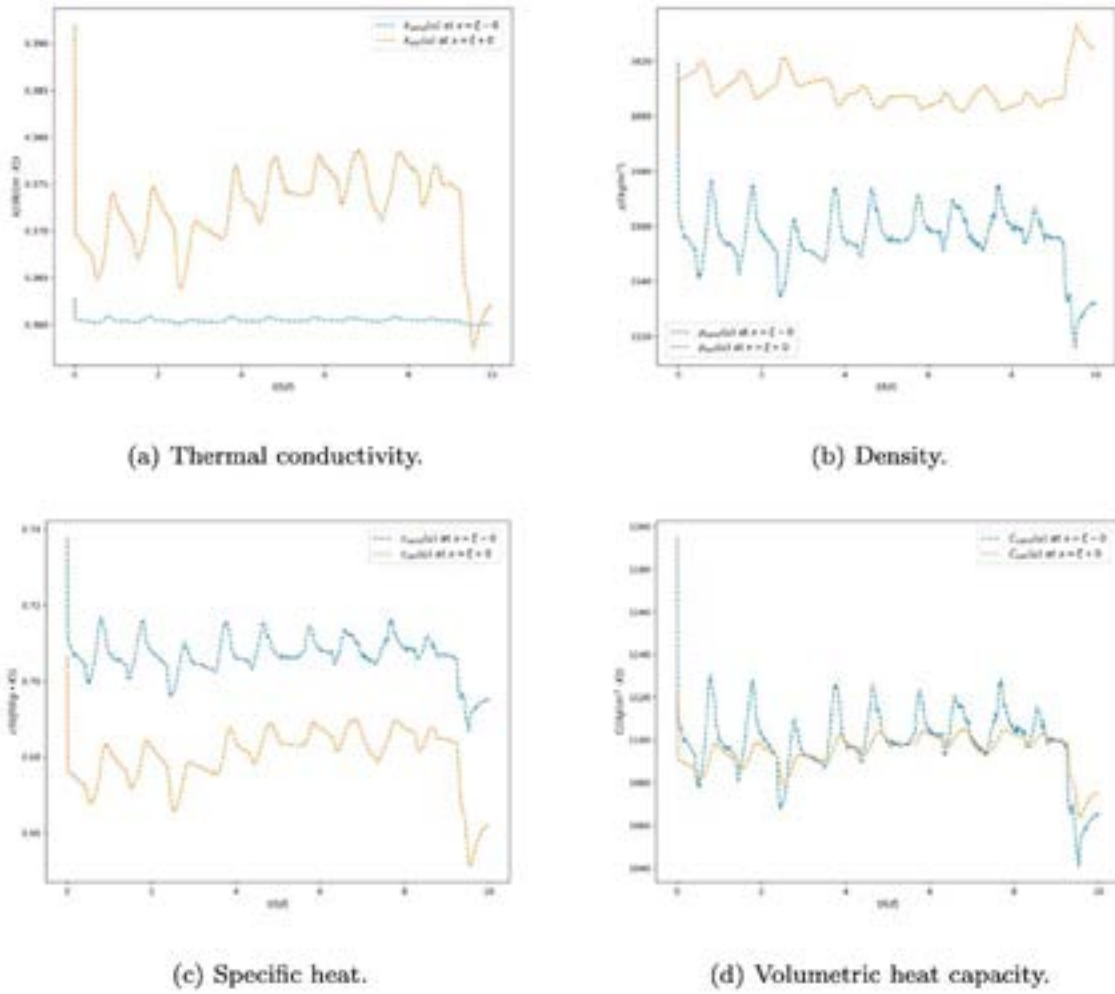


Figure 4 – The distribution of a) thermal conductivity b) density c) specific and d) volumetric heat capacity at the boundary of two materials.

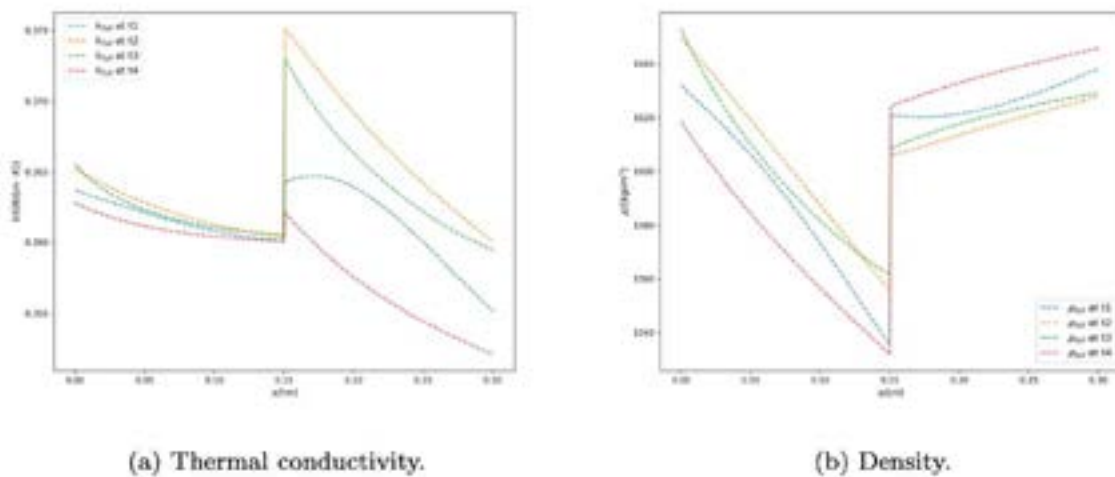


Figure 5 – Distribution of thermal conductivity and density along the container during $t_1 = 2.5/d, t_2 = 5/d, t_3 = 7.5/d, t_4 = 10/d$.

Fig.4 and Fig.5 illustrate the values of thermophysical coefficients along the container. The graphs clearly show jumps-discontinuities in the values of thermophysical coefficients at the contact boundary of contact between two media, except for the coefficient of volumetric heat capacity. From here it can also be said that the volumetric heat capacity shows a continuous nature of the values.

Conclusion

In the context of predicting and finding all thermophysical coefficients (thermal conductivity, heat capacity, density and heat transfer), this article proposes an efficient numerical method. In contrast to the methods previously proposed in the literature, this approach allows one-time determination of all thermophysical coefficients in two media with a contact boundary. This approach takes into account the impossibility of finding several coefficients in one time interval. To solve this problem, the entire measured data time is divided into segments equal to the number of coefficients, and the corresponding coefficient is calculated in each segment. In addition, one should not forget that a solution of the nonlinear heat equation is proposed with the heat conductivity coefficient, which is a cubic function, and with the heat capacity, density, and heat transfer coefficients, which are linear functions. The system of nonlinear equations is solved by Newton's method, which ensures high convergence of the solution. The initial approximation for Newton's method is taken from the solution of a linearized difference problem. Also the next approximation for Newton's method, i.e. for a nonlinear difference problem, is found using the Thomas method (sweep), which in turn is unconditionally stable. Finding the thermophysical coefficients is calculated by minimizing the corresponding functional using the steepest descent method. Using the differentiation of a nonlinear difference problem with respect to the desired parameter, the gradient of the functional and the damping coefficient are found in explicit form. With the help of this, the elimination of the solution of the adjoint problem for the solution of inverse problems is achieved. A proof of the quadratic convergence of the iterative scheme for Newton's method is also proposed.

In conclusion, it can be said that research in the field of coefficient inverse problems for non-linear equations should be advanced with detailed

experimental measurements, including, for example, moisture, freezing, porosity, etc.

Acknowledgments

This document is the result of the research project No. AP08855955 funded by MES RK.

References

1. Luikov, A.V. *Heat and Mass Transfer in Capillary-Porous Bodies*. 1964.
2. Rysbaiuly B., Adamov A.A. *Matematicheskoje modelirovanie tepla I massoobmennogo processa v mnogosloynnom grunte*. [Mathematical modeling of heat and mass transfer process in multilayer soil]. Publishing House «Kazakh University», 2020, 211 p.
3. Desta, T. Z., and Langmans, J., and Roels, S. *Experimental data set for validation of heat, air and moisture transport models of building envelopes*. Building and Environment, 2011.
4. Lipus, M.P., Reinsch, T., Weisenberger, T.B., Kragset, S., Stefansson, A., Bogason, S.G. "Monitoring of a reverse cement job in a high-temperature geothermal environment." *Geothermal Energy*.
5. Lesnic, D. "Inverse Problems with Applications in Science and Engineering", *CRC Press*, Abingdon, UK, (2021): 349 p.
6. Jumabekova, A., Berger, J., Foucquier, A., Dulikravich, G.S. "Searching an optimal experiment observation sequence to estimate the thermal properties of a multilayer wall under real climate conditions." *International Journal of Heat and Mass Transfer*. (2020).
7. Tien-Mo Shih, Chao-Ho Sung and Bao Yang. "A Numerical Method for Solving Nonlinear Heat Transfer Equations." *Numerical Heat Transfer, Part B: Fundamentals: An International Journal of Computation and Methodology*. (2008).
8. Berger J., Dutykh D., and Mendes N., and Rysbaiuly B. "A new model for simulating heat, air and moisture transport in porous building material." *International Journal of Heat and Mass Transfer*. 134, (2019): 1041–1060.
9. Travis, M., Matthew, J. "Solving nonlinear heat transfer problems using variation of parameters." *International Journal of Thermal Sciences*. (2015).
10. Battaglia, Jean-Luc, Maachou, Asma, Malti, Rachid, and Melchior, Pierre. "Nonlinear heat

diffusion simulation using Volterra series expansion.” *International Journal of Thermal Sciences*. (2013).

11. Nguyen, Huy Tuana and Pham, Hoang Quanc. “Some extended results on a nonlinear ill-posed heat equation and remarks on a general case of nonlinear terms.” *Nonlinear Analysis: Real World Applications*. (2011).

12. Huntul, Mousa, and Lesnic, Daniel. “Determination of the time-dependent convection coefficient in two-dimensional free boundary problems.” *Engineering Computations*. (2020).

13. Jumabekova, A., Berger, J., Dutykh, D., and Le Meur, H. “An efficient numerical model for liquid water uptake in porous material and its parameter estimation.” *Numerical Heat Transfer, Part A: Applications*. (2019).

14. Hasanov, A. “Simultaneously identifying the thermal conductivity and radiative coefficient in heat equation from Dirichlet and Neumann boundary measured outputs.” *Journal of Inverse and Ill-Posed Problems*. (2020).

15. Lesnic, D., Hussein, M.S., Kamynin, V., Kostina, B. “Direct and inverse source problems for degenerate parabolic equations.” *Journal of Inverse and Ill-Posed Problems*. (2020).

16. Kabanikhin, S.I., and Shishlenin, M.A. “Theory and numerical methods for solving inverse

and ill-posed problems.” *Journal of Inverse and Ill-Posed Problems*. (2019).

17. Rysbaiuly, B., Alpar, S., and Mukhametkaliyeva, N., “Nelineynaya obratnaya zadacha teploprovodnosti. Kvasilineynaya dvukhsloynaya obratnaya zadacha teploperedachi.” [Nonlinear inverse problem of heat conduction. Quasi-linear two-layer inverse heat transfer problem]. Avtorskoe proizvedenie. №EC-02-21121KZ Certificate of COPYRIGHT 10, 2021.

18. Rysbaiuly, B., “Obratnye zadachi nelineynoy teploprovodnosti”. [Inverse Problems of Nonlinear Heat Conduction]. *Издательский дом «Қазақ Университеті»*, (2022): 369.

19. Rysbaev, B., “Ustoychivost raznostnoy schemy dlya teploprovodnogo gaza s kontaktnym razryvom.” [Stability of a difference scheme for a heat-conducting gas with a contact discontinuity. Note. methods of fun. analysis in non-classical equations mat. physics]. Novosibirsk: Siberian Branch of the USSR Academy of Sciences, (1988): 17 – 24.

20. Rysbaiuly, B. “Metod. konechnykh raznostey dlya odnomernogo teploprovodnogo vyazkogo szhimaemogo gaza s kontaktnym razryvom.” [Finite difference method for one-dimensional heat-conducting viscous compressible gas with a contact discontinuity.] *Siberian journal of computational mathematics*, RAS SB, № 3(4), (2001): 32-43.

© This is an open access article under the (CC)BY-NC license (<https://creativecommons.org/licenses/by-nc/4.0/>). Funded by Al-Farabi KazNU

G.T. Balakayeva¹ , Paul Ezhichelvan² , M.K. Tursynkozha³ 

¹Al-Farabi Kazakh National University, Almaty, Kazakhstan

²School of Computer Science Newcastle University, Newcastle, Great Britain

*e-mail: mfrwedom@gmail.com

(Received 09 March 2022; received in revised form 18 April 2022; accepted 07 June 2022)

Analysis, Research and Development of an Innovative Enterprise Digitalization System for Remote Work

Abstract: This article presents innovative development of the system for the remote activity implementation. It is all about from remote customer service to the company and private conferences for employees, online conferences, meetings, training, etc. This system refers to devices for implementing the employees' remote production activities of the enterprise, to devices for organizing and managing the business processes. The developed system may be used without restrictions. The most important particularity of this useful system is the opportunity to add various features depending on the demand for a separate enterprise, upon that having saved a range of using the already existing opportunities. By applying this system, it is possible to increase by several times the level of the information and communication technologies usage for enterprises. The developed data device essentially allows economizing various resources on data transmission and storage. Besides, the requirements to the infrastructure of the enterprise may be used either by browsers or mobile devices, upon that by increasing the efficiency of analysis and the agility of making production decisions. Research and analysis of fault tolerance, applicability of modern IT technologies to increase the efficiency of enterprise digitalization have been carried out

Key words: Digitalization; remote work; webtrc; development; system

1 Introduction

At present, one of the priority areas for the development of society is a high level of digitalization of all types of activities and, as reality has shown, this is especially important for working in conditions such as a pandemic and post-pandemic. Despite a sufficient number of information systems, now there is a need to develop scalable fault-tolerant information systems, which are now in demand due to the constantly growing volume of information, big data, and the need to ensure fault tolerance.

The modern need for the development of information systems for the digitalization of enterprise activities is due to the following shortcomings of many existing systems: the impossibility of processing big data, including unstructured data, poor data security, susceptibility to unauthorized access to data files, the impossibility of making decisions in optimizing document flow routes, high cost available known systems.

There are known the various devices used when conducting remote transactions of the production activities, for instance, Zoom, MS Teams, Google meet and others. However, the devices mentioned

above have some different drawbacks and restrictions, a usage-time restriction, a restriction to quantity of participants, restriction to usage of various device capabilities, no transparency, etc. The usage of such systems may cause to several disadvantages, among them, if necessary to hold any confidential corporate meetings. There are various devices of the Enterprise Content Management and the Electronic Document Management System which are used at organizational activity of an enterprise. The widely used Directum system assigned for document flow of the enterprise (State Registration Certificate of the program for "Directum RX" computing machine dated on 22 April 2015 No.2015614659) has some restrictions such as unavailability to conduct online meeting in real-time mode, no opportunities to interact with external applications and some other restrictions [1].

The purpose of the developing system like this is the development of fault-tolerant, zoomed data device which will enable to conduct organization and management of the employees' remote production activities of the enterprise.

The prospects for the development of this scalable fault-tolerant information system are also

due to the fact that the openness of the architecture, scalability, a high level of independence of the functional subsystems of the complex, maintenance, practical development and application open up a fundamentally new possibility of distributed use by enterprises, united by a common communication intranet and Internet environment, responding general requirements for information systems and information security, intended for implementation in a single information educational space of the Republic of Kazakhstan.

2 Research of ensuring fault tolerance

The development of scalable fault-tolerant application for digitalization of enterprise activities is due to the following shortcomings of many existing systems: the impossibility of processing big data, including unstructured data, weak data security, susceptibility to unauthorized access to data files, insufficient optimization of document flow routes, high cost of known systems. The main idea for creation of such application is multitasking: for study, work, teaching, online conference, etc.

Reliability. The system architecture supports a transactional model that guarantees the integrity of system data throughout all stages of their life cycle. Managed MongoDB storage allow one to organize reliable storage of documents.

Safety. For each object of the system, it can be specified which users or groups have the right to perform certain actions with it. Confidential electronic documents and tasks can be encrypted directly in the system by any Microsoft CryptoAPI-compatible encryption provider, which guarantees protection even from users with unrestricted access to data. Logging of all user actions will allow restoring the history of work with system objects in the event of a security violation. Provides high protection against unauthorized access to document storages of all types.

Scalability. The invention enables to add some other features at customer's option as well. This is the key factor for own data device of the enterprise.

Fault tolerance and speed. Thousand or even millions of concurrent connections in the world may become the cause of failure in operation even in the largest analogue projects. This invention may operate independently for a certain enterprise, and they may be supported separately from the basic flow. That way it is possible to obtain essential increases in as well operating speed of the application.

Big data processing. The invention enables to process large volume of data of different type, which is very topical at present time.

All control services can be installed both on one server and on multiple ones – in order to distribute the load and safety. Users randomly select a server and perform their actions.

Management manipulate has been defined as the system with the aid of which managers have an effect on other participants of their agencies to put into effect their strategies, and additionally assures that the sources are obtained and used correctly and correctly in achieving its objectives.

The work of the personnel Department of a fairly large enterprise is associated with the accumulation of a large amount of data about the individual data of employees. Traditionally, data is put away on paper. Also, it is difficult to quickly select the necessary data when hiring, firing, or compiling reports. The basis of the development was a number of reasons that arise due to the influence of the human factor, which negatively affect the quality and intensity of the human resources Department:

- a) the possibility of an accidental error in manually filling out forms;
- b) inability to quickly cope with a large amount of information;
- c) the complexity of finding the necessary information;

The purpose of the development is to eliminate as much as possible random errors, the listed shortcomings of the existing system of work of the personnel Department, and to introduce into it factors that positively affect the quality and timing of the functions implemented in it:

- a) reducing the execution time of each function;
- b) automatic creation of documentation and reports;
- c) simple and fast search;
- d) automatic affixing of dates and service numbers;

All of the above indicates the relevance of the problem, a solution to which is presented in this diploma work.

Verbal description of the subject area. Main functions of the company's human resources Department:

- hiring
- calculation from work

For a detailed description, you can divide the main functions into a number of additional ones. For example, hiring involves performing the following actions:

2.1 Data Analysis

Data analysis is performed when a person is hired. To perform this function, the following documents are required: passport, work record and education document. Provided that the person has passed the interview, an order for employment is drawn up. The acceptance order must include the full name, position (workplace), date, and, accordingly, the order number.

2.2 The Preparation of an employment contract

Drawing up an employment contract is made according to the prescribed form of the contract. An employment contract (contract) is filled out when an employee is hired. Contains data: last name, first name, patronymic, service number, position (workplace), reason (number and date of the order for employment). After drawing up the employment contract, the corresponding mark is entered in the employment record and the employee's personal file is formed [2].

2.3 Formation of a personal file

Passport data and General information about the employee are stored in the personal file. In addition to the data required for drawing up an employment contract (full name, workplace (position), no. of the order of acceptance), it contains the employee's service number, personal and other data:

- Personal data:
 - date of birth, place of birth;
 - address;
 - passport: series, number;
 - pension certificate;
- Education;
- Employment history (employment history before working at the company) with the following data:
 - enterprise;
 - position;
 - experience;
 - article of dismissal;
- Documents (inventory of documents attached to the employee's personal file), indicating the fields:
 - document type;
 - identification number;
 - date of acceptance;
 - date of issue;

2.4 Changing the staffing table

The staff list of employees in the company (in the position format-the number of people working for this position), when hiring a new employee, must be changed accordingly.

2.5 Making marks in the personal file and work record

If there is a dismissal order, a corresponding note is entered in the personal file indicating the article of dismissal and the date of settlement, as well as the number of the dismissal order. In this case, a mark on the calculation is also put in the work record.

2.7 Making a service provisioning system

The technological support of the business processes continuity is, in our opinion, almost the priority task of IT system. Nobody needs in any separate feature-packed hardware and expensive software in case all this is not a reliable support, a basement for users' daily successful operations.

The capability of any system to keep its operability after failure or abruption of one or several composite components is named as the system fault tolerance. The fault-tolerance system shall keep its operability in case of abruption of one node at least, and respectively, the main way to increase the fault tolerance is to create the hardware redundancy by way of reservation (redundancy).

Users may simultaneously create their requests. For their servicing some servers are required. The quantity of servers can be several or the great one. Advantages of this approach are as follows: a request is a stream of jobs, has quality of service contract, n is kept optimal to minimise energy consumption ($n \leq N$). QoS contract:

- Charge: For each accepted and completed stream a user shall pay a fee.
- Obligation: The average waiting time, w , of the jobs in an accepted stream shall not exceed a certain bound.
- For each stream where the average waiting time exceeds the bound, a user shall receive compensation.

Thus, a contract for a given type of service is characterised by the triple: $(r_i, q_i, p_i) = (\text{charge, obligation, penalty})$. Objective. Maximize the average revenue per unit time, R [3]:

$$R = \sum_{i=0}^n a_i [r_i - p_i P(w_i > q_i)] - cS$$

where:

- a_i is the average number of type i streams accepted per unit time
- w_i is the average waiting time for the jobs in a type i stream
- S is the average number of operative servers
- C is the cost of a single server per unit time

3 Analysis and technologies

One of the first technologies that were used in application is .NET Core. Many developers think that the nature of .NET platform is unfinished. And because of that, it is practically almost always under rework and upgrades. If earlier versions of the technology are tool for the applications with large functionality, in modern times the technology allows supporting the development of API and support of Visual Basic. The technology gives the developers a great deal of freedom and, at the same time, allows fully controlling all the processes, especially when uploading the product to industrial environment. And what about the SignalR library, which is the main gateway for data exchange. SignalR is remarkably similar to SocketIO. Their main similarity is that they both support negotiation/fallback. Of course, it is important that SignalR is a library, not a server. Therefore, it should be placed on individual server together with .NET Core. There were also hosts for ASP.NET, Owin and self-host, that is why it would be possible to easily launch it in its own process, for example, right now it is a Windows service. Investigations showed that SignalR is supported by clients for JS, .NET, Silverlight, and Windows Phone 7 browsers. There are also clients for the same items as IOS, Mono Touch, etc. SignalR provided the project with much higher level of API than raw sockets, which is a great advantage compared to other similar technologies. It means that SignalR allows us to do such things as “RPC” from server to clients in a broadcast form.

The next investigation is related to Angular. Using the latest versions of Angular CLI allowed us to make the project structure in Model-View-Controller format. There was an opportunity to use Model-View or View-Model as well. When selecting this technology, the function of two-way data binding was of interest. In Angular, this function is designed so simply that there is no need to spare a lot of time to solve certain tasks. It allows aligning models and presentations without any problems. The following factors were the main reasons for technologies selection: Angular allows using HTML to create a user interface, Angular has a small number of observable functions, it facilitates modification and changes of

properties, huge support from community and framework designers themselves. Not every similar technology may afford some of the possibilities of Angular.

WebRTC is a browser technology designed to implement the transmission of streaming data among several browsers or applications using the special technology of point-to-point transmission. One of particularities of this technology is that the technology enables to establish communication among users by using browser applications only. Previously this was becoming a kind of discovery for some developers of the community when they had been inquiring after the WebRTC: in fact, it is possible to create a video chat or even an audio chat independently of an outside server— you need a certain browser only where the WebRTC is supported. The WebRTC does not require for downloading any additional extensions or plugins. You need only to do some HTML or JavaScript coding and video streams, audio streams in a browser will be working with no trouble. Perhaps, there is the next question: for which projects the WebRTC is suited? Initially, the purpose of the WebRTC is to create video conferences using technologies independently of any additional servers. The technology is ideal for developing new applications for video conferences with the help of a browser. It means that for this project the WebRTC is ideally suited. The WebRTC does not use any outside servers which may be located in various servers where it is possible to implement the data security. But the technology operates via the secure network protocols which may provide with the safety of data or streams transmission. When the WebRTC-agent is run, it does not aware of who it needs to be connected with and what kind of information it will be shared. And in this situation the Signaling comes to the rescue. Signaling solves this problem. Signaling is required for two or several browsers could find and call each other before within the network before the data transmission was started [4]. The Signaling may use the current or a secure protocol. SDP is a simple text protocol. Every SDP message consists of key-value pairs that are placed in the strict order (rfc4566), which, in return, comprise a set of streams [5]. As signaling the SignalR library had been used, and with the help of it, the WebRTC could find

each other. After setting the signaling, all sides of WebRTC browsers have enough data to connect each other. And after this, another created technology named ICE is used.

ICE (Interactive Connectivity Establishment) is a protocol of the WebRTC. The ICE enables to establish communication among several browsers. These browsers may be located both within the same network or maybe

in various parts of the world. The ICE allows solving the problem of establishing the direct communication independently of various intermediate servers. After establishing the communication between two browsers, the WebRTC moves on to setting an encrypted transmission channel. Further, this channel will be used for audio/video and data transmission [6].

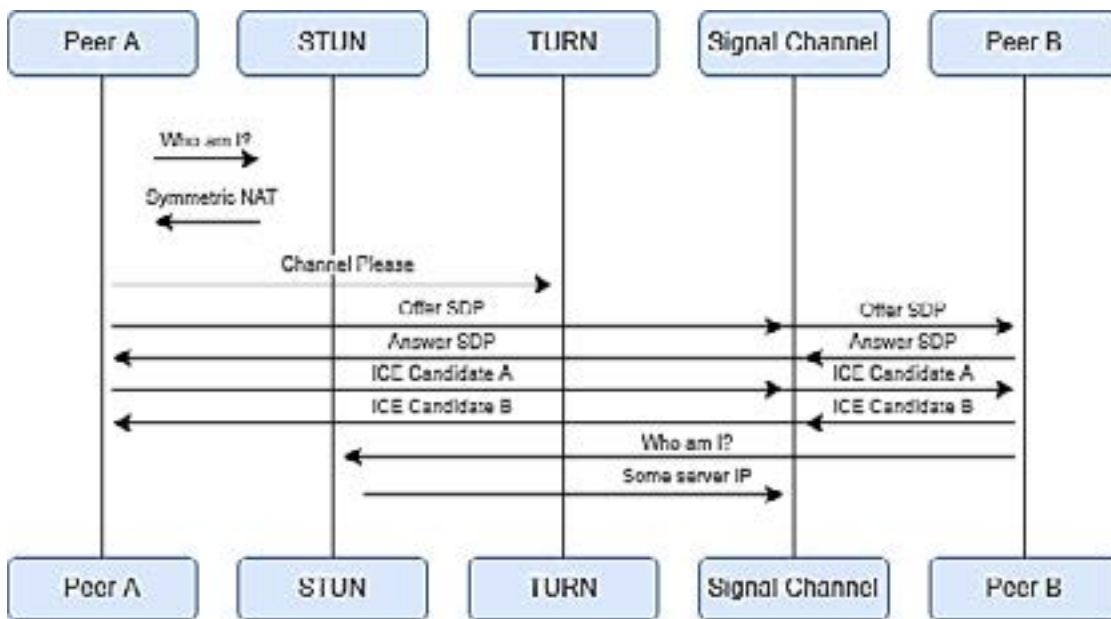


Figure 1 – WebRTC. How it works

Other standards or technologies could be used to create streaming connections between the users, but the choice fell on WebRTC [7]. The main advantages include the following:

- No need to install additional SO.
- High quality of connection and in audio stream and video stream.
- Custom modifications may be incorporated into this project with open-source code.
- There is a built-in possibility of screen, desktop capture, etc.
- Cross-platform scripting.
- Possibility to create any interface based on HTML5 and JS technologies.

Firstly, creation of a project on Angular platform for customer part, development of initial UI/UX design, which will be further supplemented, as specific tasks are completed. Secondly, NodeJS was

created with support of PeerJS. Thirdly, ASP .NET Core with SignalR library was created. This library allows exchanging messages with the server-side and the client in real-time. Operation with server part required HTTPS on the client-side for the stable operation of sockets; Fourth, creation of a database [8]. MongoDB was chosen as the database. The necessary collections for the application to work were created in advance [9].

An interface was required to start the work. The interface could be created from scratch, without using various libraries. However, that would not be rational. So, Angular CLI was chosen. Angular is an open and free platform for creating a web application. It makes the work faster, and small tasks, usually consuming a lot of time, take a few seconds on Angular. Material UI for Angular and the usual Bootstrap were used as an initial design [10].

Depending on the project, the following items are included:

1. [Bootstrap@5.0.1](#)
2. [Uuid@8.3.2](#)
3. [Microsoft/signalr@5.0.7](#)
4. PeerJS
5. MomentJS
6. Ngx-ui-loader

7. There are also built-in Angular dependencies, such as rxjs, router, angular forms, typescript, etc.

Bootstrap was used for a quick layout of required components, and Material UI was already used for a good version of project. On the one hand, it might seem that one Material UI would be enough. However, Material UI lacks some Bootstrap qualities, without which it is difficult to create a flexible interface. For example, 12 column grid, margins, etc. Many conferences require creation of a unique ID for each of them. UUID dependency is used for these purposes.

One of the main technologies of this project is WebRTC (Web Real-Time Communications). It is some kind of standard for transfer of streaming audio data, video data and various content between browsers [11]. This method gives opportunity to turn a browser into a real-time terminal [12]. To start the conference, simply click on the conference link. Examples of using WebRTC:

- Google Meet is a ready-made service for instant messaging, as well as video and audio calls [13]. Chromium browsers have many hidden WebRTC functions used by this application. Official documentation does not indicate these functions. Maybe it indicates some of them. For example, screen capture, background blur, etc [14].

- Jitsi Meet is an open-source application developed by 8x8. Technologies of this application are based on Simulcast, which means that there is unstable work on weaker communication channels and rather high requirements for a web server.

- Zoom is the only application where WebRTC is not used. It was made for improvement of communication quality and for saving server resources.

It was decided to use PeerJS library for easier work with WebRTC. The task of this library is simple. This is convenience and simplicity. Also needed a webserver to synchronize two clients for work with two clients [14]. The launch requires peer

dependency, which keeps a lot of methods and properties. After connection of the library, the application can get PeerServer property and start it with port 9000 and path /peerjs. That is, after starting NodeJS server, the application can access PeerJS via path localhost:9000/peerjs. Of course, after the global publication, this path may change. On the client-side, peerjs library is used for communication between the client and the server. After that, this stream can be controlled at your discretion [15].

In addition, as mentioned above, .NET Core is used for server part of the application. The correct work of the server part of the project requires connection with database and client part [16]. Standard REST API was used for these purposes. The server may receive various requests with different HTTP methods. Method GET is used for obtaining any data, and method POST is used for addition of new element. Methods PATCH, PUT are used for changing the element. Method DELETE is used for deleting. The request accepts a JWT token, which users receive when logging in [17]. This token controls the user roles. That is, you can control who will be allowed to delete, add or receive records. The next library for .NET Core is SignalR. SignalR is a library from Microsoft that specializes specifically for applications that work in real-time. That is, there is no need to update the page every time you receive any data from other users. The data will be sent immediately via the socket to all users in the group. The principle of the library is simple. One or more users are added to the same group [18]. Once added, they can send various data to all users of the group in the form of a text or even a file. Thus, they can communicate in real-time via chat or take a test together, etc.

The common pattern of the proposed “Digital Enterprise” data device with the streams of information is represented in Fig. 2, where the following is designated: 1 – data exchange web-server, 2 – stored data module, 3 – authentication module, 4 – general software package, 5 – controlling videoconference units, 6 – participant’s module, 7 – organizer’s module, 8 – features for the latest sessions viewing, 9 – features for voting, 10 – training process module, 11 – features for personification, 12 – features for viewing the participants’ list, 13 – training process module, 14 – training materials module, 15 – timesheet module, 16 – statement module.

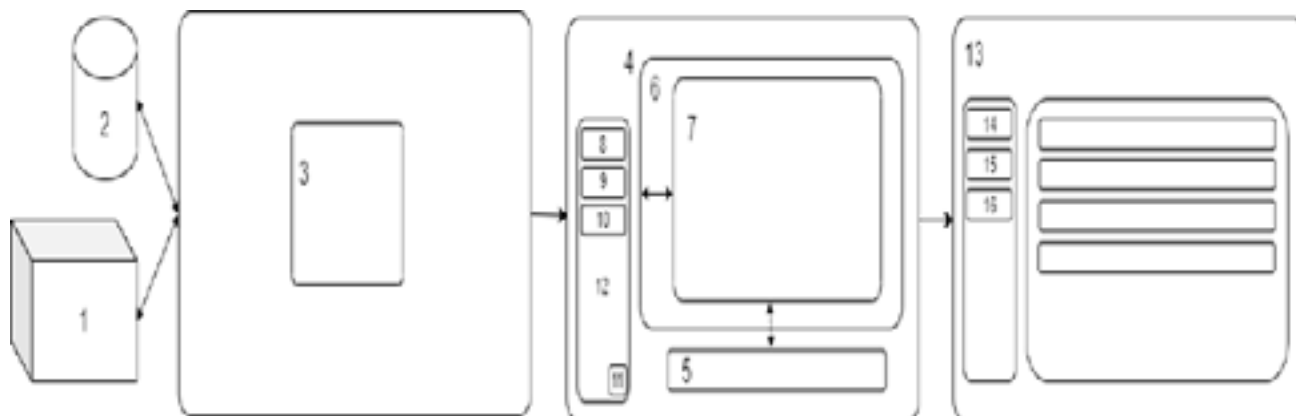


Figure 2 – Pattern of “Digital Enterprise” data device with the streams of information

4 Description of results of the conducted research

Using the proposed development, it is possible to increase the level of use of information and communication technologies in enterprises several times. The developed information device allows you to significantly save various resources for data transmission and storage. In addition, the requirements for corporate infrastructure are reduced, since Digital Enterprise can be used through browsers and mobile devices, while increasing the efficiency of analysis and the efficiency of production decision-making.

The following is a description of the results of the development of the main modules that ensure the functioning of a web application:

The authentication module is the first stage of the device usage. Users may personally pass registration or ask an administrator to add their data in the database for further authorization. If the user who has such a mail address and a password is found in the database then the user will be enabled to operate further. To ensure security of the user’s data there is the open standard used for creating access tokens to JWT. Authorization and registration were implemented in order to store user data. This functionality allows registration of new users and storing their data for subsequent authorization [19]. When registering, the E-mail, password and name fields are filled in. During authorization, these data are pulled up and filled in on the client-side. Authorization should be required for the correct operation of the project and for data logging purposes. This functionality allows identifying people entering the conference.

The data of authorized users can be stored in the database [20].

The problem of links also appeared in implementation of the functionality. When a new user joins a conference, the /conference link is used and a unique conference number is transmitted at the end. If an unauthorized user clicks the link, he/she will automatically go to the authorization page. At the same time, there is a risk of losing the unique conference number [21].

This problem was solved using the returnUrl principle. This principle is simple. When you go to the /conference page, the program records a unique conference number and transmits it to the authorization page. In turn, the authorization page stores the unique number. Upon successful authorization, the unique number will be automatically transmitted to the conference page.

The training module is one of the main modules, which is important for increasing the employees’ qualification. This module allows conducting the learning process, trainings for employees, including probationers and interns of the enterprise. The algorithm of roles division among users is developed in order to divide into students and teachers. At registration for the application, a user may automatically to get a role of a student. And in order to get a role of a teacher it is required to address to the administrator. Access to educational materials may be obtained on a page of educational materials. Every teacher is enabled to add materials for his future lessons. The lessons can be seen in the timesheet module which, in its turn, has a timetable for the next academic year. There is the knowledge evaluation is scheduled in the module – a teacher posts grades into a grade report sheet.

Interactive screen sharing by all meeting participants. Screen sharing or interactive screen sharing is a handy feature that in turn allows you to share a user's screen with other users in real-time. This feature allows to share screen with anyone in the conference and provided by the shareScreen option.

The chat was created for this purpose. When the session starts, it becomes possible to send messages to the rest of the conference participants. The chat appears on the lower right side when you click on the "Chat" button. In order to save space, it was decided to use a pop-up window that stands on top of all other parts of the application. At the top of the window, there is an inscription "Messages" with a green indicator, which in turn means the possibility of sending a message. The window can be closed by clicking on the cross or on any other place except the chat itself. On the bottom side, there is a field for filling in the message. The send button is next to it. When the send button is clicked, a request `SendMessageToConference` is sent to the server [22]. The component implements methods such as: `initTextAreaResizer`, `keepMessagesScrollInBottom`, `changeChatView`.

- `initTextAreaResizer` is an algorithm that allows expanding the chat field (If the message is too long)

- `keepMessagesScrollInBottom` – Does automatic scrolling when a new message is added

"Recent Sessions" functionality is one of the first functionality that was developed. This functionality has the standard role of storing the latest sessions and the ability to restore the connection with the latest sessions. It was initially planned to use a database for storing the latest sessions, and it likely will be done so. But at the moment, the last sessions are stored in the local store. The local store holds an array with the objects of the last session. The session ID and the date of the last connection are recorded there. The data is stored in JSON format for further processing [23].

The next module is poll. The project required a new functionality for some diversification. In addition, the possibility of implementation of various functionalities should be demonstrated. The poll was created for these purposes. This functionality helps conference participants to create polls and vote anonymously. That is, no user will be able to see who voted for what. This is one of the main advantages [24].

A new block called "Polls" was also created after "Recent Sessions" block. The poll can only be created

during an active session. Every time someone tries to create a poll, they will be able to see a text with a description that only the conference organizer can create a poll. It helps to avoid creation of many polls in one session. As soon as the session starts, the organizer has the opportunity to click on the "Add question" button. As soon as he/she clicks, a modal window opens with the contents of the Angular component.

This component contains a form, which should be filled by the organizer in order to create a new question. After filling in the "Enter a question" field, the user can click on the "Add" button. After confirmation, a SignalR request under the name questions is sent to all conference participants. As soon as such request comes from the server, the client part begins to draw a window with polls. A list of polls appears in the window, clicking on which you can vote. Every time a participant clicks on a poll, a request is sent to the socket that the participant clicked, and the data in the database should be saved and updated.

The Angular component, which adds new polls, keeps the save method. This method sends a request to SignalR method `CreateQuestion`, which in turn creates a question in the DB with the use of received data. The poll data is processes in cycle. When the value of the questions comes from the socket, the client part accepts the received data and puts it in the questions variable. After that, the total number of votes is calculated for each question in the cycle. This procedure is required for further calculations of the percentage of votes. The component part uses the built-in Angular cycle. If the number of polls is zero, then the list of polls is not shown. In the cycle, the percentage is calculated for each poll. The formula is simple: $number\ of\ poll\ votes / total\ number\ of\ votes\ of\ all\ polls * 1$

The function of module Conference input queue of accepting new participants was developed in order to make the conference confidential. The organizer or other participants can accept new users who want to join the current conference. At the same time, the new user will wait until he/she is accepted, or until he/she cancels the call.

The mobile version of the app is very important for good UI/UX. Since more than half of users access websites and other applications through a smartphone. In some cases, the mobile version is more important than the desktop version. And that's

why it was decided to slightly refine the mobile version. Unnecessary details have been removed and hid large parts of the UI. However, they can still be opened by clicking on the corresponding buttons in the mobile version of the application [25].

Also, the administrative part is developed which allows seeing the analytics of all sessions. This is the total number of sessions, quantity of participants, quantity of organizers, quantity of users, interval between creation of sessions, etc. The data are prohibited to be removed as they are fixed which allows keeping the accurate analytics. This has the large potential when introducing new capabilities in the device as these data are also can be collected and analyzed.

5 Discussion and conclusion

The system with new functionalities is developed for enterprises, which can handle various tasks: remote customer service to the company, local private conferences for employees, meetings, etc. Moreover, the using this application is regardless of the type of enterprise, small, medium, or large enterprise.

Currently, the number of online users is growing (because of Covid 19), and this process will continue for many reasons, such as post-pandemic. And not every project will be able to withstand the flow of thousands or even millions of users [26].

Main result is the data device for business communication in real time with the help of video and audio streams exchange, by using some developed updated features: a chat, anonymous surveys, training module, interactive screen sharing, etc.

The system refers to devices for implementing the employees' remote production activities of the enterprise, to devices for organizing and managing the activities of the enterprise without any time restrictions, by number of participants. The system represents the zoomed data device for digitalization of the enterprise activities by implementing the videoconference system with extended updated additional capabilities. The organizer may create its own sessions and hold online conferences. Participants may join the organizer's conference and take active, among them interactive participation, these processes result in the video and audio streams intensive exchange. Except the video and audio streams the live exchange of messages or data which

are translated to the stored data module. With the help of authentication device participants may login the applications via the link at any time of a session. The conference organizer is sharing the link and the participants who have clicked this link, may connect to the single stream of data exchange. The interrelated modules have different roles within one session. Majority of actions is controlled by the conference organizer who, at any time, may log out the current session or to disconnect from various accesses for the conference participants. The data stream is automatically translated to the database and the administrative part of the application. The administrative part has all data on users, on number of online sessions, information on all actions during the session, etc. The organizer and participants may give access to the application to use camera and microphone for further operation of the program. Current system is assigned for increasing the efficiency of enterprises activities by enabling to implement the wide range of managerial and organizational production solutions in the real-time mode, including in case of distant locations from the main workplace. Besides, the features of the tasks to solve may be expanded at customer's option – the enterprise itself.

Our developed application has several advantages. Primary advantages are: firstly, our application is not limited in operating time and does not require payment for the time of use; secondly, scalability, which was developed with using of the REST API (it is the ability to process requests from any operating system iOS, Android, Microsoft) or other systems will be able to use network requests to communicate with the API. This means that other systems can integrate thanks to the REST API and protected methods; the third advantage is "Interactive Screen Demonstration", Interactive screen sharing between all meeting participants; Another significant advantage is voting. This feature helps conference participants create polls vote anonymously.

It was possible to achieve the maximum data processing speed. This means that any requests will be processed quickly and efficiently. In addition, when developing, first of all, in addition to the server's properties, you should optimize the code. All the possibilities of object-oriented programming on the server-side of the developed application were used. Moreover, thanks to this, it was possible to avoid the procedural programming style. Furthermore, the main advantage of the "Digital

Enterprise" project is that it was possible to develop a digital application that will be different for each enterprise since other new functions can be added to our application at the request of a customer – an enterprise following the specifics of the operation of this enterprise.

The top priority of its usage is multitasking. It can be used for various purposes: holding online meetings, voting, demonstration and discussion, increase in performance of the personnel (rated surveys, trainings, education) and others. The application developed is assigned for enterprise digitalization. It allows adding features at customer's option and completely integrating into the information environment of an enterprise.

The developed application for real-time business communication through the exchange of video and audio streams, using the developed modern functionality: chat, anonymous surveys, used without restrictions, training module, interactive use of the screen, etc. The most important feature of this is the ability to add various functions depending on the requirements of an individual enterprise, while maintaining the range of use of existing capabilities.

Currently, the developed application "Digital Enterprise" is used for online meetings, training and plan to expand its use in the activities of other companies.

Acknowledgment

This research was funded by the Science Committee of the Ministry of Education and Science of the Republic of Kazakhstan (Grant #AP09259208).

References

1. J. Andersson, "Enterprise Information Systems Management," Thesis, 114p, 2002.
2. G. Gross, "WebRTC technologies prove to be essential during pandemic," IETF interview with Adam Roach, 2020. [Online]. Available: <https://www.ietf.org/blog/webrtc-pandemic/>
3. Aidarov K.A., Mitrani I., Ezhilchelvan P. Energy-aware Management of Customer Streams // Electronic Notes in Theoretical Computer Science, London, UK – Volume 296. – 2012 – pp. 199-210
4. Developer Mozilla, "RTCPeerConnection," Properties, methods, events, 2021. [Online]. Available: <https://developer.mozilla.org/en-US/docs/Web/API/RTCPeerConnection>
5. Developer Mozilla, "Signaling and video calling," The signaling server, 2021. [Online]. Available: https://developer.mozilla.org/en-US/docs/Web/API/WebRTC_API/Signaling_and_video_calling
6. Alan B. Johnston, "WebRTC: APIs and RTCWEB Protocols of the HTML5 Real-Time Web," WebRTC adds standard APIs, pp.127-135, 2012.
7. "WebRTC for the Curious," What is WebRTC, 2020. [Online]. Available: <https://webrtcforthe curious.com/docs/01-what-why-and-how/>.
8. "Big Data: New Opportunities for Growing Business," 2021. [Online]. Available: <http://www.pcweek.ru>
9. Metanit.com, "MongoDB Online Manual," Working with MongoDB Database, 2021. [Online]. Available: <https://metanit.com/nosql/mongodb/>
10. Matthew F Callahan, "How to implement SignalR in a .NET 5 + Angular 12 web application," SignalR and Angular, 2021. [Online]. Available: <https://mfcallahan.blog/2020/11/05/how-to-implement-signalr-in-a-net-core-angular-web-application/>
11. R. Stewart, "Stream Control Transmission Protocol," 2007. [Online]. Available: <https://tools.ietf.org/html/rfc4960>.
12. M. Baugher, D. McGrew, M. Naslund, E. Carrara and K. Norrman, "The Secure Real-time Transport Protocol (SRTP)," 2004. [Online]. Available: <https://tools.ietf.org/html/rfc3711>. (5 authors)
13. "WebRTC.org implementation," Google Git. [Online]. Available: <https://webrtc.googleusercontent.com/src/>
14. P. Barrera and F. Stimberg, "Improving audio quality in Duo with WaveNetEQ," Google AI Blog, 2020. [Online]. Available: <https://ai.googleblog.com/2020/04/improving-audio-quality-in-duo-with.html>
15. Alex Sosnovskiy, "PeerJS Server," 2021. [Online]. Available: <https://github.com/peers/peerjs-server>
16. Metanit.com, "Work with MongoDB," Creating a project and connecting MongoDB, 2021. [Online]. Available: <https://metanit.com/sharp/aspnet5/27.1.php>
17. Filip Tonic, ".NET JWT Authentication with MongoDB," Implement JWT Authentication, 2021. [Online]. Available: <https://medium.com/nerd-for-tech/net-jwt-authentication-with-mongodb-9bca4a33d3f0>

18. IETF, “Real-time communication in Web-browsers (RTCWeb) working group,” 2021. [Online]. Available: <https://datatracker.ietf.org/wg/rtcweb/documents/>
19. J.W. van Houwelingen, “Relevance and Usability of Enterprise Architectures during Post Merger IT Integrations: Master Thesis,” 83p., 2008.
20. H. Panetto, M. Zdravković, R. Jardim-Goncalves, D. Romero, J. Cecil et al., “New Perspectives for the Future Interoperable Enterprise Systems,” *Computers in Industry*, № 79, pp. 47-63, 2016. (2 authors)
21. M. Petit-Huguenin, G. Salgueiro, J. Rosenberg, D. Wing, R. Mahy et al., “Session Traversal Utilities for NAT (STUN),” 2020. [Online]. Available: <https://tools.ietf.org/html/rfc8489>
22. Microsoft.com, “Create a web API with ASP.NET Core and MongoDB,” Create the ASP.NET Core web API project, Configure MongoDB, 2021. [Online]. Available: <https://docs.microsoft.com/en-us/aspnet/core/tutorials/first-mongo-app?view=aspnetcore-5.0&tabs=visual-studio>
23. T. Reddy, A. Johnston, P. Matthews and J. Rosenberg, “Traversal using relays around NAT (TURN): Relay extensions to session traversal utilities for NAT (STUN),” 2020. [Online]. Available: <https://tools.ietf.org/html/rfc8656>. (4 authors)
24. “Digitization with Document Management System.” [Online]. Available: <https://www.kreyonsystems.com/Blog/digitization-with-document-management/>
25. E. Protalinski, “Google Meet noise cancellation is rolling out now—here's how it works,” *VentureBeat*, 2020. [Online]. Available: <https://venturebeat.com/2020/06/08/google-meet-noise-cancellation-ai-cloud-denoiser-g-suite/>
26. L. Doug, “3D Data Management: Controlling Data Volume,” *Velocity and Variety*, Meta Delta, 949-951 p., 2001.
27. “Guide to Digital Document Management,” [Online]. Available: <https://www.imageapi.com/blog/digital-document-management/>
28. IETF, “WebTransport,” 2021. [Online]. Available: <https://datatracker.ietf.org/wg/webtrans/about/>
29. E. Ivov, “This is what end-to-end encryption should look like,” 2020. [Online]. Available: <https://jitsi.org/blog/e2ee/>

© This is an open access article under the (CC)BY-NC license (<https://creativecommons.org/licenses/by-nc/4.0/>). Funded by Al-Farabi KazNU

G.A. Ashirova¹ *, A.K. Manapova² , A.O. Beketaeva¹ ¹Institute of Mathematics and Mathematical Modeling, Almaty, Kazakhstan²Kazakh British Technical University, Almaty, Kazakhstan*e-mail: gulzana.ashyrova@yandex.ru

(Received 23 February 2022; received in revised form 18 March 2022; accepted 30 March 2022)

Numerical Simulation of Particle Dynamics in the Hydrogen-Air Mixing Layer

Abstract. In this paper, supersonic plane turbulent mixing layer of gases with injection of solid particles is studied numerically. The gas phase are determined by DNS solving the multi-species Navier-Stokes equations in the Eulerian approach, and the dynamic of solid particles are traced in the Lagrangian approach. The dynamics of hydrogen – air mixing and the formation of the vortex system in the mixing layer and its effect on the distribution of solid particles in the two free-flow speeds are investigated. The study focuses on detailed analysis an influence of the vortex system in the supersonic turbulent mixing layer on the dispersion solid particles with different size. The results show that heavy particles almost do not react to vortex structures. It is revealed that medium particles tend to accumulate along the circumference of the vortex and along the braid between the two vortices. A quasi-equilibrium state with a gas flow of light particles is established.

Key words: two-phase flow, solid particles, multicomponent gas, mixing layer, Navier - Stokes equations.

Introduction

The understanding of the physics of mixing properties, ignition, and combustion, which are related to the turbulent supersonic mixing layer flow in the presence of particles, is strongly needed for the optimal design and operation of scramjet combustors.

The two-phase flows involving solid, droplet, or suspensions are investigated intensively both experimentally [1-3] and numerically [4-13]. Quite a lot of research have been devoted to the study of particle dynamics in subsonic flows [7–10]. In [7] with a two-way coupling way. It was revealed in the process of vortex rolling up and vortices pairing, the particles with different Strouhal numbers have a very different pattern of dispersion. In [9] using DNS was found that the asymmetry of the developing mixing layer leads to an increase in the number of particles moving from the upper faster flow to the lower flow. Authors [10] used two-way coupled Eulerian–Lagrangian approach have been studied the particle dynamics in a turbulent boundary layer via DNS. They found the influence of the wall on the particle

velocity and distribution is significant in the near wall region but is little in the outer region.

Limited number studies of particle dispersion in a supersonic flow have been performed [11-13]. For example, authors [11] showed the particle dispersion in a spatially developing compressible mixing layer. The direct numerical simulations were performed with different Stokes numbers. It has been shown the particles tend to accumulate in the peripheries of the vortical structures with high density, low vorticity inside the mixing layer, as well as the high-density regions behind the shocklets outside the mixing layer.

The Eulerian-Lagrangian approach is used for high-speed shear layers with monodisperse, adiabatic, inertial particles in the [12] to study the interactions of particles and flow turbulence and their effect on pressure fluctuations. It was found the particle–turbulence interactions change the local pressure intensity due to the displacement of the flow (due to the particles) and significant turbulence changes.

In accordance with the above, the numerically detailed analysis and discuss the influence the vortex system in the turbulent supersonic multispecies

mixing layers on the dispersion solid particles with different size will be performed via DNS numerical

simulation applying a high-order essentially nonoscillatory (ENO) scheme (Figure 1).

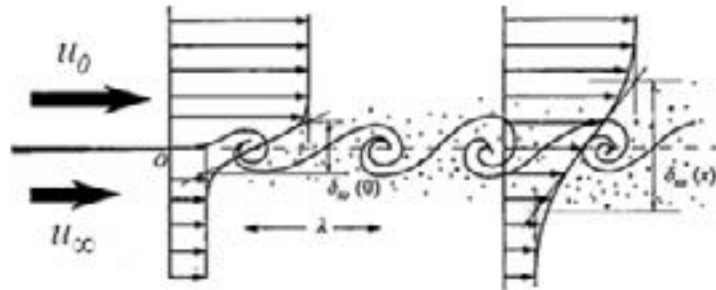


Figure 1 – Scheme of the development of the mixing layer

Model of gaseous phase

The basic equations are the system of two-dimensional Navier–Stokes equations for a multispecies gaseous mixture, which is written in the Cartesian coordinate system in the conservative form:

$$\frac{\partial \bar{U}}{\partial t} + \frac{\partial (\bar{E} - \bar{E}_v)}{\partial x} + \frac{\partial (\bar{F} - \bar{F}_v)}{\partial z} = 0, \quad (1)$$

here the vectors $\bar{U}, \bar{E}, \bar{F}$ have the form

$$\bar{U} = \begin{pmatrix} \rho \\ \rho u \\ \rho w \\ E_t \\ \rho Y_k \end{pmatrix}, \quad \bar{E} = \begin{pmatrix} \rho u \\ \rho u^2 + p \\ \rho u w \\ (E_t + p)u \\ \rho u Y_k \end{pmatrix},$$

$$\bar{F} = \begin{pmatrix} \rho w \\ \rho u w \\ \rho w^2 + p \\ (E_t + p)w \\ \rho w Y_k \end{pmatrix},$$

and \bar{E}_v, \bar{F}_v - the dissipative terms of the form

$$\bar{E}_v = (0, \tau_{xx}, \tau_{xz}, u\tau_{xx} + w\tau_{xz} - q_x, J_{kx})^T,$$

$$\bar{F}_v = (0, \tau_{xz}, \tau_{zz}, u\tau_{xz} + w\tau_{zz} - q_z, J_{kz})^T.$$

The tensors of viscous stresses and heat fluxes are:

$$\tau_{xx} = \frac{\mu_1}{Re} \left(2u_x - \frac{2}{3}(u_x + w_z) \right),$$

$$\tau_{zz} = \frac{\mu_1}{Re} \left(2w_z - \frac{2}{3}(u_x + w_z) \right),$$

$$\tau_{xz} = \tau_{zx} = \frac{\mu_1}{Re} (u_x + w_x),$$

$$q_z = \frac{\mu_1}{Pr Re} \cdot \frac{\partial T}{\partial z} + \frac{1}{\gamma_\infty M_\infty^2} \sum_{k=1}^N h_k J_{zk},$$

$$q_x = \frac{\mu_1}{Pr Re} \cdot \frac{\partial T}{\partial x} + \frac{1}{\gamma_\infty M_\infty^2} \sum_{k=1}^N h_k J_{xk},$$

$$J_{kx} = -\frac{\mu_1}{Sc Re} \cdot \frac{\partial Y_k}{\partial x}, \quad J_{kz} = -\frac{\mu_1}{Sc Re} \cdot \frac{\partial Y_k}{\partial z},$$

where ρ is the density, u and w are the velocity components, p is the pressure, E_t is the total energy, Y_k is the mass fraction of the k^{th} species, Wk is the molecular weight of the k^{th} species ($k = 1, \dots, N$, N is the number of species in the gas mixture), Re is the Reynolds number, Pr is the Prandtl number, Sc is the Schmidt number.

The equation of state for the mixture of perfect gases may be written as

$$p = \frac{\rho T}{\gamma_\infty M_\infty^2 W},$$

where $W = \left(\sum_{k=1}^N \frac{Y_k}{W_k} \right)^{-1}$ is the molar weight of the

mixture of all gases, and $\sum_{k=1}^N Y_k = 1$.

The equations for the total energy have the following form:

$$E_t = \frac{\rho h}{\gamma_\infty M_\infty^2} - p + \frac{1}{2} \rho (u^2 + w^2), \quad (2)$$

where $h = \sum_{k=1}^N Y_k h_k$ is the mixture specific enthalpy,

$h_k = h_k^0 + \int_{T_0}^T c_{pk} dT$ is the specific enthalpy of the k^{th} component.

The specific heats at constant pressure are computed for each component c_{pk} via the molar specific heats C_{pk} by the formula $c_{pk} = C_{pk} / W$, where C_{pk} are determined from experimental data with the aid of the fourth-order polynomial interpolation in temperature:

$$C_{pk} = \sum_{i=1}^5 \bar{a}_{ki} T^{(i-1)},$$

where $\bar{a}_{jk} = a_{jk} T_\infty^{j-1}$.

The numerical values of empirical constants a_{jk} have been taken from the table JANAF [28] at normal pressure ($p = 1 \text{ atm}$) and standard temperature $T = 293 \text{ K}$.

The mixture molecular viscosity is determined by Wilke's formula [14]

$$\mu_l = \sum_{i=1}^N \frac{X_i \mu_i}{\Phi_i},$$

where the function Φ_i is specified in the form

$$\Phi_i = \sum_{r=1}^N X_r \left[1 + \sqrt{\frac{\mu_i}{\mu_r}} \left(\frac{W_r}{W_i} \right)^{1/4} \right]^2 \left[\sqrt{8} \sqrt{1 + \frac{W_i}{W_r}} \right]^{-1},$$

μ_i is the molecular viscosity of the i^{th} component, it is calculated by the formula

$$\mu_i = \frac{\mu_{i\infty}}{\mu_{\Lambda\infty}} \sqrt{W_i T_\infty},$$

where $\mu_{i\infty} = 2.6693 \cdot 10^{-7} \frac{\sqrt{W_{i\infty} T_\infty}}{\sigma_i^2 \Omega_i^{(2.2)*} (T_i^*)}$,

$\mu_{i\infty} = \sum_{i=1}^N \frac{X_i \mu_{i\infty}}{\Phi_i}$, σ_i is the collision diameter of the i^{th} component, the values of components are presented in the work [14]: $\sigma_1 = 2.63$, $\sigma_2 = 3.30$, $\sigma_3 = 3.5$, $\sigma_4 = 3.050$, $\sigma_5 = 0.50$, $\sigma_6 = 0.560$, $\sigma_7 = 3.50$, $\Omega_i^{(2.2)*}$ is the integral of collisions for the momentum transfer, $T_i^* = kT / \varepsilon_i$ is the reference temperature, ε_i / k is the parameter of the potential function of the intermolecular interaction. According to the work [15], $\Omega_i^{(2.2)*} (T_i^*) = 1$.

The turbulent flow is assumed quasi-two-dimensional, and the system of the Navier–Stokes equations is solved with the aid of the two-dimensional DNS approach without using the additional closing turbulence models.

Disperse phase model

The following assumptions are adopted for the dynamic particles: the particles are the spheres of the same size; the interaction of particles with one another is not taken into account; the particles motion does not affect the gas flow; the forces of Saffman and Magnus do not consider hence the small aluminum particles are considered. In accordance with these assumptions, the equations for the motion trajectory (\vec{x}_p) and the velocity (\vec{u}_p) of particles are written as follows:

$$\frac{d}{dt} \vec{x}_p = \vec{u}_p, \quad (3)$$

$$m \frac{d}{dt} \vec{u}_p = \vec{F}_p + mg,$$

where $m = \frac{4}{3} \pi r_p^3 \rho_p$ is the mass of a spherical

solid particle, ρ_p is the density of the solid particle of the p^{th} component, F_p is the drag force acting from the gas side on the particle of radius r_p which is determined as

$$\vec{F}_p = C_D \frac{1}{2} \pi r_p^2 \rho |\vec{u} - \vec{u}_p| (\vec{u} - \vec{u}_p),$$

here C_D is the drag coefficient, μ is the coefficient of the gas dynamic viscosity.

For the case of a turbulent flow around a particle at $Re > 1$, different formulas are used for the drag coefficient C_D (based on the Stokes formula $C_D = 24/Re$) with regard for gas properties and motion regime. The most known formula is the one proposed in the [16], which is also used in the present work in the form:

$$C_D = \begin{cases} \frac{24}{Re_p} \left(1 + \frac{1}{6} Re_p^{2/3} \right), & Re_p \leq 1000, \\ 0.424, & Re_p > 1000, \end{cases}$$

where $Re_p = \frac{2\rho|\vec{u} - \vec{u}_p|}{\mu}$ is the Reynolds number built in terms of the particle radius r_p .

The governing equations (1)–(3) are written in dimensionless form. As the non-dimensionalization parameters, the following reference values of the upper flow have been taken: $u_\infty, \rho_\infty, T_\infty, Y_{k\infty}$; the pressure and total energy are related to the value $\rho_\infty u_\infty^2$, the reference length is the vorticity inlet

thickness $\delta_\omega = \frac{(u_\infty - u_0)}{(\partial u / \partial z)_{\max}}$. The time scale is

defined as $t \approx \delta_\omega / u_\infty$. The same parameters as for the gaseous phase are taken for disperse phase at the non-dimensionalization.

Initial and boundary conditions

The parameters of gas flows are specified at the inlet as follows:
the upper flow

$$u = u_0 = M_0 \sqrt{\gamma_0 RT_0 / W_0}, w = 0, p = p_0, T = T_0,$$

$$Y_k = Y_{k0} \text{ at } x = 0, 0 \leq z < H_1,$$

the lower flow

$$u = u_\infty = M_\infty \sqrt{\gamma_\infty RT_\infty / W_\infty}, w = 0, p = p_\infty,$$

$$T = T_\infty, Y_k = Y_{k\infty}$$

$$\text{at } x = 0, H_1 + \delta \leq z < H_2, H_z = H_1 + \delta + H_2.$$

H_z is the height and H_x – the length of the region under consideration.

At the inlet, the particle velocities are set equal to the flow velocities at the injection point. In a thin mixing layer, the initial velocity u are determined by the hyperbolic tangent function

$$\varphi(z) = 0.5(\varphi_0 + \varphi_\infty) + 0.5(\varphi_0 - \varphi_\infty) \tanh(0.5z / \delta_\theta), \quad (4)$$

where

$$\varphi = (u, Y_k, T),$$

$$\delta_\theta(x) = \int_{H_1/2}^{H_2/2} (\rho(\tilde{u} - u_\infty)(u_0 - \tilde{u})) / (\rho_\infty \Delta u^2) dz$$

$\delta_\theta(x)$ is the thickness of the momentum loss,

$\tilde{u} = (u - u_\infty) / \Delta u$ is the gas mean velocity,

$\Delta u = (u_\infty - u_0)$ is the difference of inlet velocities.

The initial conditions are set in the same way as the inlet boundary conditions. The non-reflecting boundary conditions are specified at the outlet, bottom, and top boundaries, where the gas fluxes and perturbations pass through the boundary and do not reflect back [17]. The inflow perturbation at the inlet the boundary conditions, in which one adds for the velocity fields $\vec{u}(z)$ a random phase u_{dist} :

$$\vec{u} = \vec{u}(z) + \vec{u}_{distr},$$

where

$$\vec{u}_{distr} = \sum_{m=1}^3 A_m \cdot \Delta u \cdot \text{Gaussian}(z) \cdot \sin(\omega_m \cdot t + \alpha), \quad (5)$$

here $\bar{u}(z)$ is the hyperbolic tangent function defined by formula (4). The A_m is the perturbation amplitude, which is satisfying the condition that the given product $A_m \Delta u$ must be equal to 0.1–0.2% of the maximum velocity of gases at the inlet. The perturbation frequency ω_m are taken: $\frac{2\pi}{18} \leq \omega_m \leq \frac{2\pi}{10}$. The $Gaussian(z)$ is the Gauss function the maximum value of which is equal to unity at $z = 0$ and α is a random number.

Method of solution

Numerical solution of the system of equations (1), i.e., the gaseous phase, is carried out in two stages. At the first stage, one computes the vector of the thermodynamic parameters \bar{U} and at the second stage, the mass fraction of the k^{th} species $Y_k = 1, 7$. For a more detailed consideration of the flow at the inlet of the mixing layer, the grid clustering is introduced with the aid of the following transformations:

$$\xi = \xi(x), \eta = \eta(z). \quad (6)$$

In this case, the system of equations (1) in generalized coordinates is written as:

$$\begin{aligned} \frac{\partial \tilde{U}}{\partial t} + \frac{\partial \tilde{E}}{\partial \xi} + \frac{\partial \tilde{F}}{\partial \eta} &= \frac{\partial \tilde{E}_{v2}}{\partial \xi} + \frac{\partial \tilde{E}_{vm}}{\partial \xi} + \\ &+ \frac{\partial \tilde{F}_{v2}}{\partial \eta} + \frac{\partial \tilde{F}_{vm}}{\partial \eta} \end{aligned} \quad (7)$$

where

$$\begin{aligned} \tilde{U} &= \frac{1}{J} \bar{U}, \quad \tilde{E} = \begin{pmatrix} \xi_x \\ J \end{pmatrix} \bar{E}, \quad \tilde{F} = \begin{pmatrix} \eta_z \\ J \end{pmatrix} \bar{F}, \\ \tilde{E}_{v2} &= \begin{pmatrix} \xi_x \\ J \end{pmatrix} \bar{E}_{v2}, \quad \tilde{E}_{vm} = \begin{pmatrix} \xi_x \\ J \end{pmatrix} \bar{E}_{vm}, \\ \tilde{F}_{v2} &= \begin{pmatrix} \eta_z \\ J \end{pmatrix} \bar{F}_{v2}, \quad \tilde{F}_{vm} = \begin{pmatrix} \eta_z \\ J \end{pmatrix} \bar{F}_{vm}, \\ J &= \frac{\partial(\xi, \eta, \zeta)}{\partial(x, z, y)} - \text{Jacobian transformation.} \end{aligned}$$

The numerical solution algorithm is based on a finite-difference third-order ENO scheme, which have been described in detail in the work [18-21].

Using the known values of the original variables and equation (2), the temperature field is computed with the aid of the equation

$$\begin{aligned} f(T) &= E_t - \frac{\rho}{\gamma_\infty M_\infty^2 W} (H(T) - R T) - \\ &- \frac{1}{2} \rho (u^2 + w^2) = 0, \end{aligned} \quad (8)$$

where H is the molar enthalpy of the gas mixture. The solution of the algebraic equation (8) for temperature is found by the Newton–Raphson iteration method [15].

The system of the ordinary differential equations (3) for the particles is solved with the explicit second order Euler method.

Results and Discussion

For the verification of the numerical method, the test problem of the shear flow of the multispecies gases without particles is solved. The numerical results are compared with computations of the [22]. For that the test problem is performed with follows conditions: the inflow lower air are a mixture of nitrogen (N_2) and oxygen (O_2) $Y_{O_2} = 0.232$, $Y_{N_2} = 0.768$; the inflow upper flow the mixture of nitrogen (N_2) and hydrogen (H_2) $Y_{H_2} = 0.1$, $Y_{N_2} = 0.9$. The flow parameters for air – $M_\infty = 2.1$, $T_\infty = 2000K$, $p_\infty = 101321Pa$, for nitrogen-hydrogen mixture – $M_\infty = 2$, $T_\infty = 2000K$, $p_\infty = 101321Pa$. The convective Mach number $M_c = (u_c - u_\infty) / a_\infty$, $u_c = (a_\infty u_0 + a_0 u_\infty) / (a_\infty + a_0)$, amounted here to $M_c = 0.38$. The dimensionless length and height of the domain are $H_x = 350$, $H_z = 120$. The geometric parameters of the problem under consideration are dimensioned to the initial thickness of the momentum loss which at the entrance is $9.35 \times 10^5 m$. For numerical simulation, the finest grid spacing is specified as non-dimensional 0.03 around the mixing layer center and the cell numbers in the x and z directions are 626x241.

Figure 2 shows turbulent shear stresses $\sigma_{uu} = \sqrt{u''^2} / \Delta u$ и $\sigma_{uw} = \sqrt{u''w''} / \Delta u$ in the sections $x = 320$. Turbulent characteristics, such as the intensity of turbulence and Reynolds stresses have quantitatively small discrepancies.

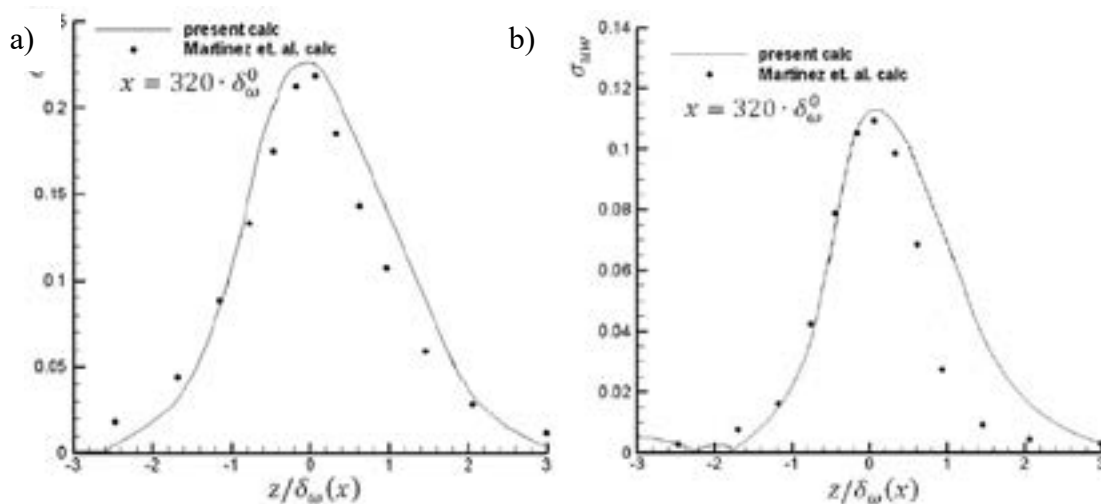


Figure 2 - Comparison of the calculated data obtained by the ENO scheme (solid line) and the numerical results of Martinez et al. [22] (circle points) for the profiles of turbulent shear stresses at section $x = 320\delta_w^0$, a) σ_{uu} , b) σ_{uw}

The numerical simulation of the posed problem was carried out for the dimensionless domain $H_x = 320, H_z = 80$. The inflow lower air with $Y_{O_2} = 0.232, Y_{N_2} = 0.768$ and upper flow (the mixture of nitrogen (N_2) and hydrogen (H_2)) with $Y_{H_2} = 1, Y_{N_2} = 0$ are taken. The Mach number of injected upper hydrogen-nitrogen mixture is $M_0 = 2$ and for lower air $M_\infty = 1.5$. The gas flow temperature is adopted equal $T_0 = 600, T_\infty = 1200$, the pressure $p_0 = p_\infty = 1 \text{ atm}$. The aluminum particles of the three sizes of diameters $d = 95\mu\text{m}, d = 9,5\mu\text{m}, d = 1,9\mu\text{m}$ are injected from five holes at the entrance simultaneously which is located near the center of the mixture layer ($x = 0, z = 20, 30, 40, 50, 60$).

The graphs below show non-stationary vortex system obtained by numerical simulation. The

dynamics of hydrogen – air mixing are illustrated in Figure 3 by instantaneous hydrogen concentration and streamlines at different time: a) $t = 100$, b) $t = 200$, c) $t = 400$, d) $t = 600$, e) $t = 1000$.

As follows from figures, a significant curvature of the streamlines begins at time $t = 100$, in the cross section $x = 50$ as a result of flow instability (Figure 3a). It is confirmed by the distribution of hydrogen contours, where formation of vortices begins in this section (Figure 3a) and the whirling vortex captures the airflow and simultaneously the hydrogen mixture takes out leading to the mixing layer expands. Over time, the number of arising vortices increases conducting to a considerable growth of the mixing layer in the hydrogen-air mixture. Therefore, the intensification of vortex twisting closed hydrogen zones are formed in the centers of their rotation (Figure 3d)

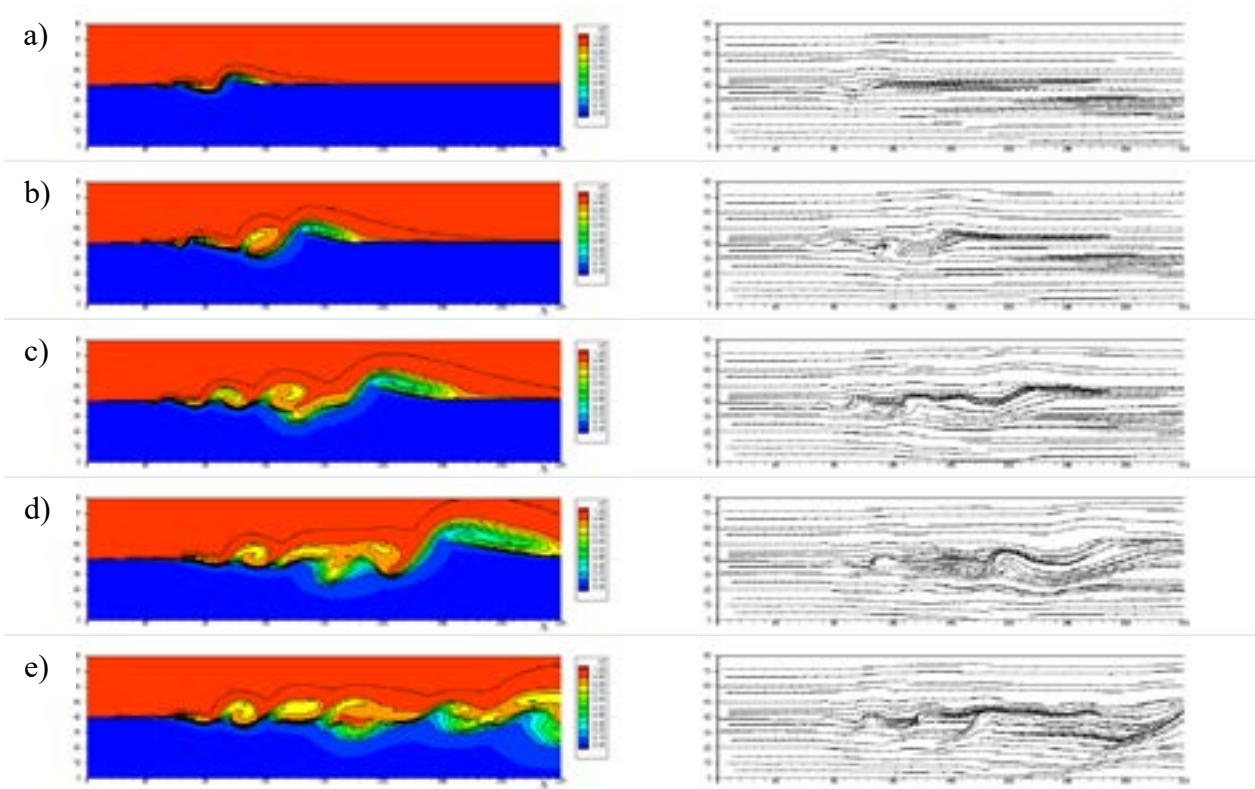


Figure 3–Distribution of the hydrogen mass concentration (left) and distribution of streamlines (right) at different time: a) $t = 100$, b) $t = 200$, c) $t = 400$, d) $t = 600$, e) $t = 1000$

The dynamics of vortex bubbles and entrained particles (particle dispersion over time) is shown in Figure 4, which illustrates instantaneous vorticity contours and particle trajectories at various moments

- a) $t = 100$, b) $t = 200$, c) $t = 400$,
d) $t = 600$, e) $t = 1000$.

Numerical experiments reveal that neighboring vortices merge (pair) and form larger ones at moments of time $t = 200, t = 400, t = 600$ (Figure 3 b – d). Apparently, each such merging lead to the entrainment of the non-whirling gas in the mixing layer thereby to the thickening of mixing layer. The generation of three vortex systems is observed at a distance from $x = 40$ to $x = 180$ by the moment of time $t = 200$ in Figure 4b and the number of vortices grow to 4 and 5 at times $t = 400$ and $t = 600$, respectively. A stable turbulent vortex structure forming with time ($t = 1000$) and consisting of seven vortices is shown in Figure 4 e.

The particle distribution provided in the same figure demonstrate that particles injected into the rapid upper flow move much faster compared to particles injected into the slower lower flow at the

initial time $t = 100$. Hence, for example, the particles that started moving from the inlet point $x = 0$ and injected at the height $z = 50, 60$ propagate by the moment of time until the cross section $x = 200$. Part of them gets into the vortex zone ($x = 80 \div 160$) and the trajectories of these particles become circular.

However, the slow moving particles (the particles injected from lower stream at height ($z = 20, z = 30$)) are still not captured by vortices and continue moving along their own trajectories and reach the position $x = 80$ by the moment of time $t = 100$. It follows from Figure 4 b – d, e that the particles are entrained completely into the vortex zone of the mixing layer over time, despite that dispersion of particles injected into the slower flow is much less compared to the particles which move in the faster flow.

As you can see from numerical experiments, that particles have tendency to accumulate in the periphery of vortex structures, which is visible from Figure 4, therefore, they are captured by vortices practically uniformly.

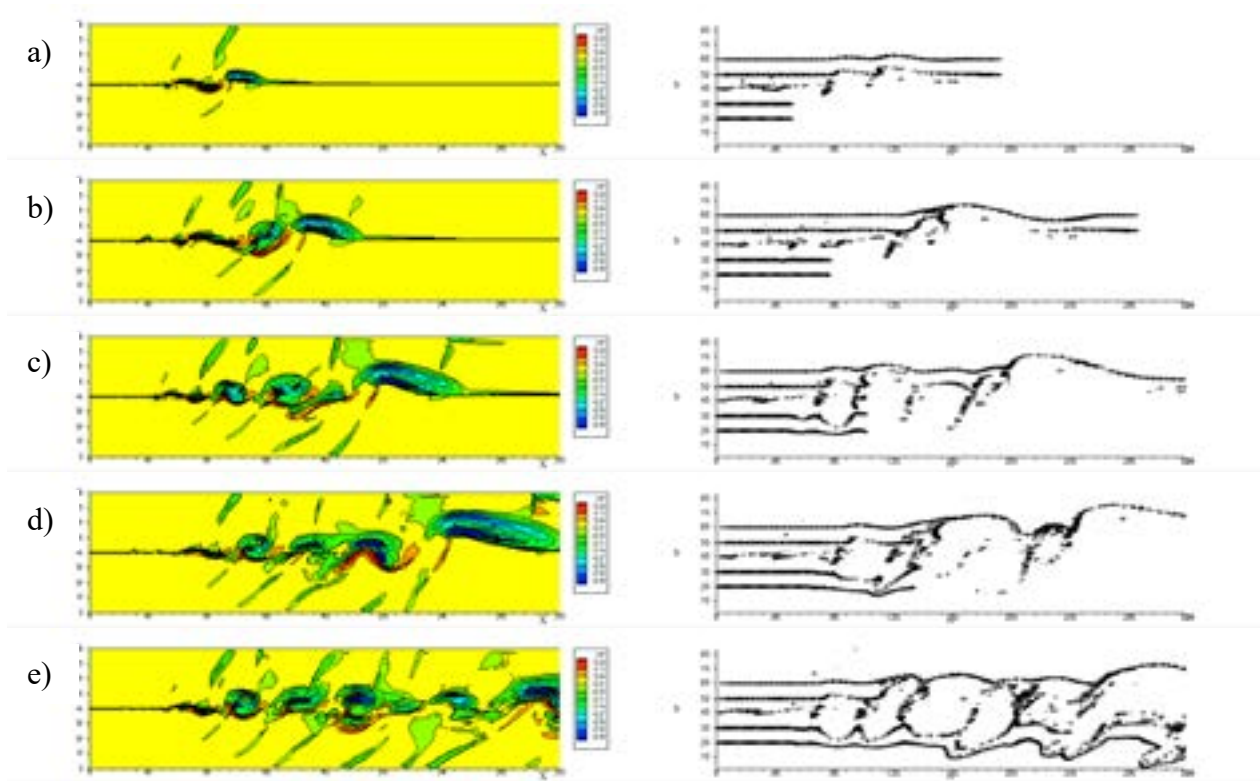


Figure 4—Distribution of vorticity contours (left) and distribution of particles (right) at different time
a) $t = 100$, b) $t = 200$, c) $t = 400$, d) $t = 600$, e) $t = 1000$

The above result shows that particles injected into the faster flow are more dispersed than particles injected into the slow flow, which are in qualitative agreement with the observed behavior of particles in the developing mixing layer. Despite that, the mixing of particles

between the two flows is shifted towards low velocity. It is confirmed in Figure 5, where presented the quantitative distribution of particles in the upper (Figure 5a) and in the low (Figure 5 b) mixing layers along the centerline of the x – axis at time $t = 1000$.

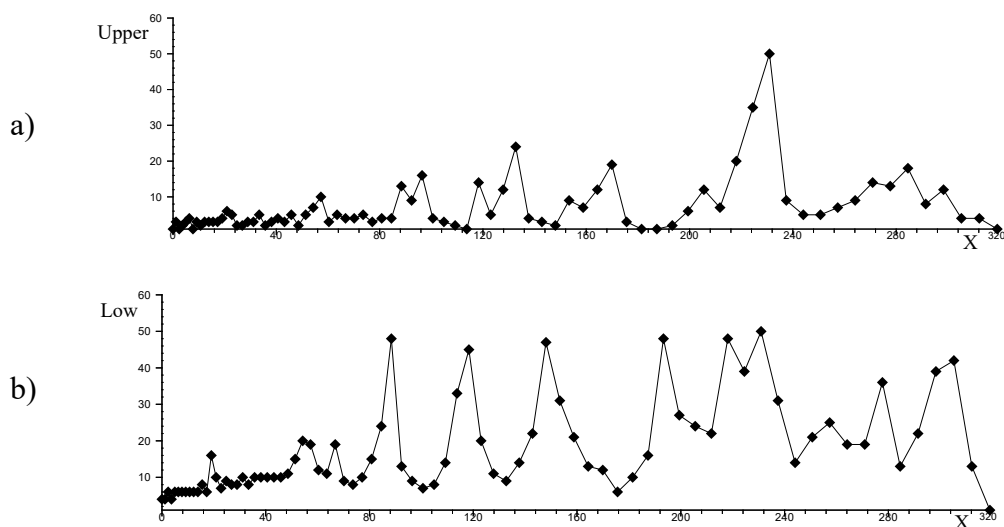


Figure 5 – Quantitative distribution of particles of the upper (a) and lower (b) flows over the cross section x at time $t = 1000$.

The number of particles is determined as follows:

$$N_{\text{rms}}(x) = \left(\sum_{i=1}^{N_{\text{cp}}} \frac{N_i(x)^2}{N_{\text{cp}}} \right)^{1/2},$$

here N_{cp} is the total number of grid cells, $N_i(x)$ is the number of particles in the i^{th} cell. As is seen in the Figure 5, the number of particles in the lower airflow is larger in comparison with their number in the upper flow of the hydrogen-nitrogen mixture.

Figures 6-7 provide numerical results with three different particle sizes of *a)* $d = 95 \text{ mkm}$ (heavy), *b)* $d = 9.5 \text{ mkm}$ (medium), *c)* $d = 1.85 \text{ mkm}$ (light). The following shows an analysis of the influence of particle sizes on the dispersion of particles and their location in the turbulent mixing layer.

Figure 6 shows the motion pattern of particles with different diameters *a)* $d = 95$, *b)* $d = 9.5$,

c) $d = 1.85$ at the time points $t = 100$ (left) and $t = 200$ (right). Fluid flow practically does not affect the distribution of heavy particles due to the absence of large stable structures at the time $t = 100$ (Figure 6a).

However, medium and light particles are already transported through the first vortices, which leads to a curvature of the particle's trajectories, which can be observed in Figure 6 b, c. It can be seen here that the particles are moving away from the vortex cores, accumulating in the areas surrounding the vortices and in the areas of the braid. The trajectories of heavy particles do not change at time $t = 200$ (Figure 6), even though larger vortices are created at this time (see Figure 3), this is since the intrinsic momentum of the particles is significantly greater than the momentum generated by the vortices. In this case, medium and light particles are attracted by large vortices from large distances to the mixing layer. The particle distribution becomes non-uniform and a large area of the vortex core still has not particles.

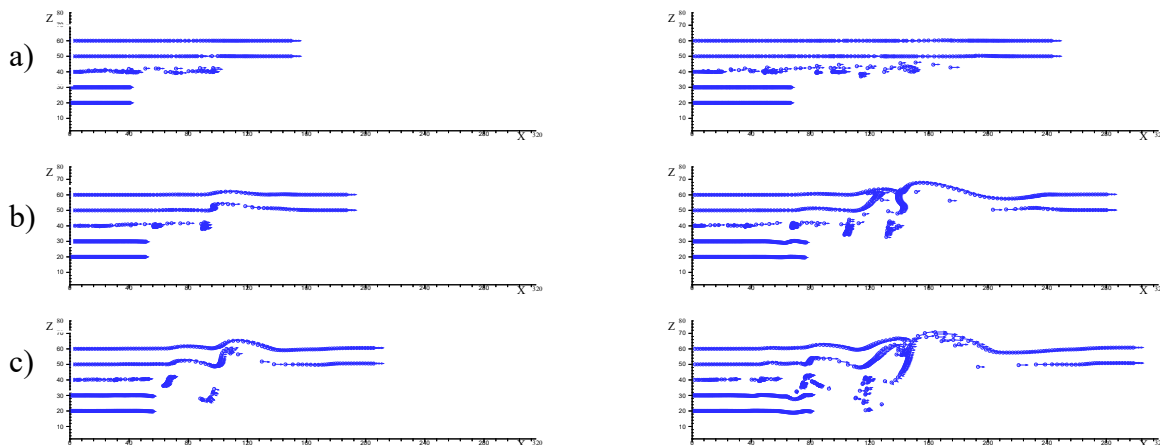


Figure 6 – Particle's trajectories at times $t = 100$ (left) and $t = 200$ (right) *a)* $d = 95$, *b)* $d = 9.5$, *c)* $d = 1.85$

Figure 7 demonstrated dispersion of particles with different diameters *a)* $d = 95$, *b)* $d = 9.5$, *c)* $d = 1.85$ at times $t = 600$ and $t = 1000$. One can see that the movement and distribution of particles in the mixing layer are strongly influenced by size. Heavy particles move along rectilinear trajectories. The particles almost do not react to the turning and rotation of large vortex structures, a small dispersion is observed only downstream.

However, medium-sized particles tend to accumulate along the circumference of the vortex and along the braid between the two vortices, which leads to appearing some "empty" areas where the solid particles are almost not observed (Figure 7b). This is due to the effects of deformation of the flow field in combination with centrifugal effects. This result means that the simulated flow can create almost linearly ordered particle dispersion structures at certain particle sizes.

On the contrary, light particles are carried throughout the flow field, including the vortex nuclei, which is clearly seen in the cross section $160 < x < 320$ (Figure 7c). Since these particles

react faster to flow changes, the structure of the particle dispersion resembles the flow vortex structure. In other words, light particles are in a quasi-equilibrium state with the gas.

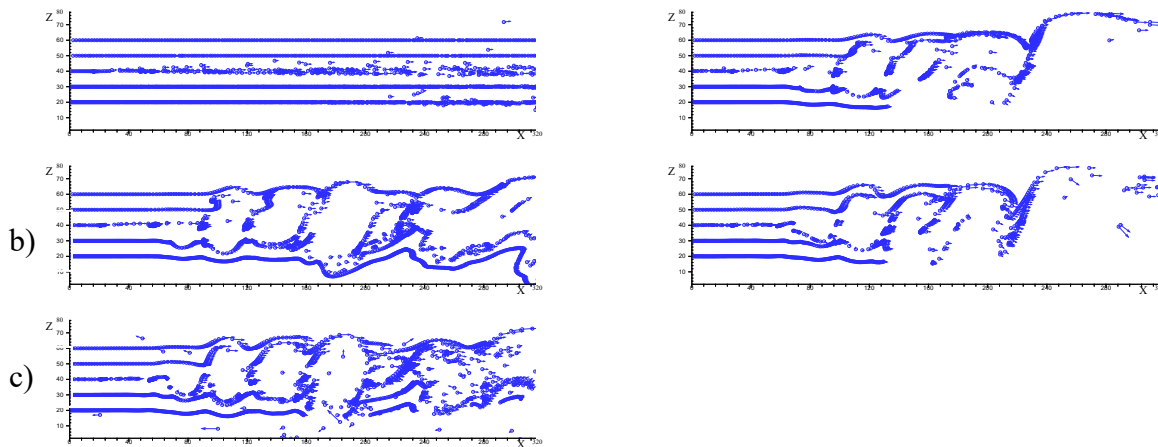


Figure 7 - Particles trajectories at times $t = 600, t = 1000$
 a) $d = 95$, b) $d = 9.5$, c) $d = 1.85$

Conclusion

A supersonic plane turbulent mixing layer of gas-particles for the flow of two parallel streams of hydrogen (upper high-speed) and air (lower low-speed) is numerically studied. It was found that the hydrogen – air mixing are generated non-stationary vortex system. It is revealed that neighboring vortices pair and form larger ones over time. Thereby, mixing layer is thickened. The particle distribution indicates that the particles injected into the fast upper stream move much faster than the particles injected into the slower lower stream. Particles are eventually completely entrained into the vortex zone of the mixing layer, even though the dispersion of particles injected into a slower flow is much smaller than particles that move in a faster flow. Numerical experiments show that particles tend to accumulate on the periphery of vortex structures. Numerical results with three different particle sizes at various time are also examined. It is confirmed that the movement of particles and their distribution in the mixing layer are strongly influenced by size. Heavy particles almost do not react to vortex structures. At the same time, medium particles tend to accumulate along the circumference of the vortex and along the braid between the two vortices. On the contrary, particles with a small diameter are carried by the gas

flow throughout the flow field, including the vortex cores.

References

1. Kulick J.D., Fessler J.R., Eaton J.K. “Particle response and turbulence modification in fully developed channel flow”. *J. Fluid Mech.* 277, 109–34. (1994)
2. Simakov N.N., “Experimental verification of the early crisis of drag using a single sphere”. *Tech. Phys.* 55, 7. (2010): 913–919.
3. Muste M., Parthasarathy R.N., Patel V.C. “Discriminator laser Doppler velocimetry for measurement of liquid and particle velocities in sediment-laden flows”. *Exp. Fluids.* 22. (1996): 45–56.
4. Lazaro B.J., Lasheras J.C. “Particle dispersion in the developing free shear layer”. *Part 1, Journal Fluid Mechanics.* 143. (1992): 235-247.
5. Lazaro B.J., Lasheras J.C. “Particle dispersion in the developing free layer”. *Part 2, Journal Fluid Mechanics.* 235. (1992): 179-185.
6. Pakhomov M.A., Terekhov V.I. “Solid particle spreading in gas-dispersed confined swirling flow. Eulerian and Lagrangian approaches”. *Thermophysics and Aeromechanics.* 24, 3. (2017): 325–338.
7. Lin J.Z., Lin J., Shao X.M., et al. “Research on particle dispersion in a plane-mixing layer with

- coherent structure”. *Acta Mech Sinica*. 19. (2003): 535–542.
8. Aggarwal S.K., Yapo J.B., Grinstein F.F., Kailasanath K. “Numerical simulation of particle transport in planar shear layers”. *Comp. Fluids*. 25, 1. (1996): 39–59.
 9. Hu Z., Luo X., Luo K.H. “Numerical simulation of particle dispersion in a spatially developing mixing layer”. *Theoret. Comput. Fluid Dyn.* 15, 6. (2002): 403–420.
 10. Luo K., Dai Q., Liu X., Fan J. “Effects of wall roughness on particle dynamics in a spatially developing turbulent boundary layer”. *Int. J. Multiphase Flow*. 111. (2018):414-421.
 11. Dai Q., Jin T., Luo K., Fan J. “Direct numerical simulation of particle dispersion in a three-dimensional spatially developing compressible mixing layer”. *Phys. Fluids*. 30. (2018): 56-78.
 12. Buchta D.A., Shallcross G., Capecelatro J. “Sound and turbulence modulation by particles in high-speed shear flows”. *J. Fluid Mech*. 875. (2019): 254-285.
 13. Ren Zh., Wang B., Zheng L. “Numerical analysis on interactions of vortex, shock wave, and exothermal reaction in a supersonic planar shear layer laden with droplets”. *Physics of Fluids*. 30. (2018).
 14. Lapin Yu.V., Strelets M.Kh. “Internal Flows of Gas Mixtures”. *Nauka*. (1989).
 15. Kee R., Rupley F.M., Miller J.A. “CHEMKIN-II: a Fortran chemical kinetic package for the analysis of gas-phase chemical kinetics”. *Sandia Report SAND89-8009B*. (1989).
 16. Chein R., Chung J.N. “Effects of vortex pairing on particle dispersion in turbulent shear flows”. *Multiphase Flow*. 13. (1987): 775-785.
 17. Poinso T.J., Lele S.K. “Boundary conditions for direct simulation of compressible viscous flows”. *J. Comp. Phys*. 101, 1. (1992): 104-129.
 18. Beketaeva A.O., Naimanova A.Zh. “Numerical study of spatial supersonic flow of a perfect gas with transverse injection of jets”. 19. *Journal of Applied Mechanics and Technical Physics*. 52. (2011): 896-904.
 20. Beketaeva A.O., Bruel P., Naimanova A. Zh. “Vortical structures behind a transverse jet in a supersonic flow at high jet to crossflow pressure ratios”. *Journal of Applied Mechanics and Technical Physics*. 56, 5. (2015): 777-788.
 21. Beketaeva A.O., Moissejeva Ye.S., Naimanova A. Zh. “Numerical simulations of shock-wave interaction with a boundary layer in the plane supersonic flows with jet injection”. *Thermophysics and Aeromechanics*. 23, 2. (2016):173-183.
 22. Beketaeva A.O, Bruel P., Naimanova A.Zh. “Detailed Comparative Analysis of Interaction of a Supersonic Flow with a Transverse Gas Jet at High Pressure Ratios.” *Technical Physics*. 64, 10. (2009): 1430–1440.
 23. Martinez Ferrer P.J., Lehnasch G., Mura A. “Direct numerical simulations of high speed reactive mixing layers”. *J. Physics: Conf. Ser.* 395. (2012).

This is an open access article under the (CC)BY-NC license (<https://creativecommons.org/licenses/by-nc/4.0/>). Funded by Al-Farabi KazNU

Kh. Khompysh*  A.A. Kabidoldanova 

Al-Farabi Kazakh National University, Almaty, Kazakhstan,

*e-mail: konat_k@mail.ru

(Received 24 March 2022; received in revised form 23 May 2022; accepted 30 May 2022)

An Initial-Boundary Value Problem for Kelvin-Voigt Equations with $(p(x), q(x), m(x))$ Structure

Abstract. A proof of a existence global in time of solutions of initial-boundary value problems for nonlinear equations mostly is not easy, even in some cases it is impossible. However, by establishing some qualitative properties of its solutions, one can find answers to such questions. For example, by establishing the blowing up in a finite time property of a solution, one can show that a solution does not exist globally in time. Thus, in last years, the investigating the qualitative properties of solutions such as localization and/or blow up in a finite time, has been developing rapidly.

In this work, we study the nonlinear initial-boundary value problem for the generalized Kelvin-Voigt equations describing the motion of incompressible viscoelastic non-Newtonian fluids. The equations generalized by replacing the diffusion and relaxation terms in equation with $p(x)$ -Laplacian and $q(x)$ -Laplacian, respectively, and adding a nonlinear absorption term with variable exponents and coefficients. A definition of a weak solution is given. Under suitable conditions for variable exponents and coefficients, and data of the problem, the blowing up of weak solution is established.

Key words: Kelvin-Voigt equation, blow up, p -Laplacian, damping term.

1. Introduction

In this work, we study the following initial-boundary value problem for the modified Kelvin-

Voigt equations (without convective term) perturbed by $p(x), q(x)$ -Laplacian diffusion, relaxation and damping term with variable exponents and coefficients

$$\bar{v}_t + \nabla \pi = \operatorname{div} \left(\chi(x) |D\bar{v}|^{q(x)-2} D\bar{v}_t + \mu(x) |D\bar{v}|^{p(x)-2} D\bar{v} \right) + \gamma(x) |\bar{v}|^{m(x)-2} \bar{v}, \quad (x, t) \in Q_T, \quad (1)$$

$$\operatorname{div} \bar{v} = 0, \quad (x, t) \in Q_T \quad (2)$$

that supplemented by the following initial and boundary conditions

$$\bar{v}(x, t) \Big|_{t=0} = \bar{v}_0(x), \quad x \in \Omega, \quad (3)$$

$$\bar{v}(x, t) \Big|_{\Gamma_T} = 0. \quad (4)$$

Here $\Omega \subset R^n$, $n \geq 2$, is a bounded domain with a smooth boundary $\partial\Omega$ and $Q_T = \Omega \times (0, T)$ is the

bounded cylinder with lateral $\Gamma_T = \partial\Omega \times (0, T)$,

$D(\bar{v}) = \frac{1}{2} (\nabla \bar{v} + \nabla \bar{v}^T)$ is the rate of the strain tensor,

the vector function $\bar{v}(x, t) = (v_1, v_2, \dots, v_n)$ is a velocity field, the scalar function $\pi(x, t)$ is a pressure, μ is a viscosity kinematic coefficient, and χ is a viscosity relaxation coefficient. The coefficients χ, μ, γ and the exponents q, p, m are given measurable functions on Ω , such that

$$\begin{aligned} 0 < \mu^- \leq \mu(x) \leq \mu^+ < \infty, \quad 0 < p^- \leq p(x) \leq p^+ < \infty, \\ 0 < \chi^- \leq \chi(x) \leq \chi^+ < \infty, \quad 0 < q^- \leq q(x) \leq q^+ < \infty, \\ 0 < \gamma^- \leq \gamma(x) \leq \gamma^+ < \infty, \quad 0 < m^- \leq m(x) \leq m^+ < \infty, \end{aligned} \quad (5)$$

where “+” and “-” on power denote the *ess sup* and *ess inf* values on Ω of corresponding functions, for example, for the function $\sigma(x)$:

$$\sigma^+ := \operatorname{ess\,sup}_{x \in \Omega} \sigma(x), \quad \sigma^- := \operatorname{ess\,inf}_{x \in \Omega} \sigma(x).$$

The system of equations (1)-(2) with $p=q=2$ and $\gamma=0$ and with constant coefficients is called the classical linear Kelvin-Voigt equations and it is used as the model of the motion of incompressible non-Newtonian fluids [1-3]. The name of the Kelvin-Voigt equations has been appeared in works of Oskolkov [4-8], though neither Kelvin nor Voigt have suggested any system of equations and these equations have been used in some cases even before the above Oskolkov's works. For instance, in 1966, Ladyzhenskaya [9] has suggested these classical Kelvin-Voigt equations as a regularization to the 3-dimensional Navier-Stokes equations to ensure the existence of unique global solutions, see also [2, 10-11] and references therein.

The various initial-boundary value problems for the classical linear and nonlinear Kelvin-Voigt equations have been studied by several authors, for instance, in [2], [4-11] for homogenous fluids, i.e. when the density is a known constant, and in [12], for nonhomogeneous fluids, i.e. when the density is unknown function.

On the other hand, the equation (1) is the pseudo-parabolic type equation, and the blow up properties of solutions of such equations with p-Laplacian with variable and constant exponents were studied in [13-15] (see the references therein).

In last years, as PDE generalized by p-Laplacian and nonlinear damping terms, an investigation of modified equations of hydrodynamics, in particular, the Navier-Stokes equations modified with p-Laplacian diffusion and with a damping term is rapidly developing, see [16-19].

The system (1)-(4) with a convective term, when all exponents and coefficients are constant, has been studied in [20]-[22], where the existence and uniqueness and the qualitative properties of weak solutions as large time behaviors and blow up in a finite time, are established.

Organization of this paper: in section 2, we introduce functional spaces, the inequalities and preliminary results used in the analysis. Later, in section 3 we state and prove our main result, in which we establish the conditions under which the weak

solutions to the investigating problems are blow up in a finite time.

2. Notation and Preliminaries

In this section, we introduce the necessary definitions and preliminary results to state the main results of this paper. For the definitions and notations of the function spaces used throughout the paper and for their properties, we address the reader to e.g. the monographs [19, 25] cited in this work. We just fix the following notations for the functions spaces of mathematical fluid mechanics:

$$\begin{aligned} \wp &:= \{v \in C_0^\infty(\Omega) : \operatorname{div} \bar{v} = 0\}, \\ H &:= \text{closure of } \wp \text{ in the norm of } L^2(\Omega); \\ V_p &:= \text{closure of } \wp \text{ in the norm of } W^{1,p}(\Omega). \end{aligned}$$

Let $1 \leq p < \infty$ and $\Omega \in R^n, n \geq 1$, be a domain. We will use the classical Lebesgue spaces $L^p(\Omega)$ whose norm is denoted by $\|\bullet\|_{p,\Omega}$. For any nonnegative k , $W^{k,p}(\Omega)$ denotes the Sobolev space of all functions $u \in L^p(\Omega)$ such that the weak derivatives $D^\alpha u$ exist, in the generalized sense, and are in $L^p(\Omega)$ for any multi-index α such that $0 \leq |\alpha| \leq k$.

Let $p : \Omega \rightarrow [1, \infty]$ be a measurable function and we define

$$p^- := \operatorname{ess\,inf}_{x \in \Omega} p(x), \quad p^+ := \operatorname{ess\,sup}_{x \in \Omega} p(x).$$

Given $p : \Omega \rightarrow [1, \infty]$ we denote by $L^{p(\cdot)}(\Omega)$ the space of all measurable functions u in Ω such that its semimodular is finite

$$A_{p(\cdot)} := \int_{\Omega} |u(x)|^{p(x)} dx < \infty.$$

The space $L^{p(\cdot)}(\Omega)$ is called Lebesgue space with variable exponent equipped with the norm

$$\|u\|_{p(\cdot), \Omega} := \operatorname{inf} \left\{ \lambda > 0 : A_{p(\cdot)} \left(\frac{u}{\lambda} \right) \leq 1 \right\},$$

and $L^p(\Omega)$ becomes a Banach space with this norm.

The weak solution to the problem (1)-(4) is understood as the following sense

Definition 1. The vector function $\vec{v}(x, t)$ is called a weak solution to the problem (1)-(4), if:

- (i) $\vec{v}(x, t) \in L^\infty(0, T; H(\Omega) \cap V_{q(x)}(\Omega)) \cap L^{p(x)}(0, T; V_{p(x)}(\Omega)) \cap L^{m(x)}(Q_T)$,
- (ii) $\vec{v}(x, 0) = \vec{v}_0(x)$ a.e. in Ω ;
- (iii) and for every $\bar{\varphi}(x) \in H(\Omega) \cap V_{q(x)}(\Omega) \cap V_{p(x)}(\Omega) \cap L^{m(x)}(\Omega)$ and for a.e. $t \geq 0$ holds

$$\frac{d}{dt} \int_{\Omega} (\vec{v} \cdot \varphi + \chi(x) |D\vec{v}|^{q(x)-2} D\vec{v} : D\varphi) dx + \int_{\Omega} \mu(x) |D\vec{v}|^{p(x)-2} D\vec{v} : D\varphi dx = \int_{\Omega} \gamma(x) |\vec{v}|^{m(x)-2} \vec{v} \varphi dx. \quad (6)$$

3. Main result

In this section, we establish the conditions for the coefficients, exponents and data of the problem,

that a weak solution to the problem (1)-(4) blows up in a finite time, i.e. the weak solution does not exist globally in time.

Theorem 1. Let the conditions (5) be fulfilled and for the exponents $p(x), q(x), m(x)$ hold the conditions:

$$p^+ \leq m^- \text{ and } m^- > \max\{2, q^+\}. \quad (7)$$

Let us assume, that also $\vec{v}_0 \in V^{p(x)}(\Omega) \cap L^{m(x)}(\Omega)$ and

$$\int_{\Omega} \left(\frac{\gamma(x)}{m(x)} |\vec{v}_0|^{m(x)} - \frac{\mu(x)}{p(x)} |D\vec{v}_0|^{p(x)} \right) dx \geq 0. \quad (8)$$

Then there exists a finite time $T_{\max} < \infty$ (defined by (18)) such that a weak solution to problem (1)-(4) blows up.

Proof. The proof of Theorem 1 is based on the methods, presented in [23-24].

Let us first introduce the following functional

$$\Phi(t) = \int_0^t \left(\frac{1}{2} \|\vec{v}\|_2^2 + \int_{\Omega} \frac{\chi(x)}{q(x)} |D\vec{v}|^{q(x)} dx \right) d\tau.$$

Under the conditions of Theorem 1, for every nontrivial solution of (1)-(4) and for all $t > 0$

$$\Phi'(t) = \frac{1}{2} \|\vec{v}\|_2^2 + \int_{\Omega} \frac{\chi(x)}{q(x)} |D\vec{v}|^{q(x)} dx \geq 0. \quad (9)$$

Testing now (6) by \vec{v} and using

$$\frac{d}{dt} \left(\int_{\Omega} \frac{\chi(x)}{q(x)} |D\vec{v}|^{q(x)} dx \right) = \int_{\Omega} \chi(x) |D\vec{v}|^{q(x)-2} D\vec{v} : D\vec{v}_t dx.$$

we have

$$\begin{aligned} & \frac{d}{dt} \left(\frac{1}{2} \|\vec{v}\|_{2,\Omega}^2 + \int_{\Omega} \frac{\chi(x)}{q(x)} |D\vec{v}|^{q(x)} dx \right) = \\ & = \int_{\Omega} (\gamma(x) |\vec{v}|^{m(x)} - \mu(x) |D\vec{v}|^{p(x)}) dx \end{aligned} \quad (10)$$

Combining (9) and (10), we obtain

$$\Phi''(t) = \int_{\Omega} (\gamma(x) |\vec{v}|^{m(x)} - \mu(x) |D(\vec{v})|^{p(x)}) dx. \quad (11)$$

Next, taking $\varphi = \vec{v}_t$ in (6) for all $t \geq 0$, we get

$$\begin{aligned} & \|\vec{v}_t\|_{2,\Omega}^2 + \int_{\Omega} \chi(x) |D\vec{v}|^{q(x)-2} |D\vec{v}_t|^2 dx = \\ & = \frac{d}{dt} \left(\int_{\Omega} \left(\frac{\gamma(x)}{m(x)} |\vec{v}|^{m(x)} - \frac{\mu(x)}{p(x)} |D\vec{v}|^{p(x)} \right) dx \right). \end{aligned} \quad (12)$$

Integrating (12) by τ from 0 to t and applying the assumption (8), we get

$$\begin{aligned} & \int_0^t \left(\|\bar{v}_t\|_2^2 + \int_{\Omega} \chi(x) |D\bar{v}|^{q(x)-2} |D\bar{v}_t|^2 dx \right) d\tau = \\ & \int_{\Omega} \left(\frac{\gamma(x)}{m(x)} |\bar{v}(t)|^{m(x)} - \frac{\mu(x)}{p(x)} |D\bar{v}(t)|^{p(x)} \right) dx - \int_{\Omega} \left(\frac{\gamma(x)}{m(x)} |\bar{v}_0|^{m(x)} - \frac{\mu(x)}{p(x)} |D\bar{v}_0|^{p(x)} \right) dx < \\ & \int_{\Omega} \left(\frac{\gamma(x)}{m(x)} |\bar{v}(t)|^{m(x)} - \frac{\mu(x)}{p(x)} |D\bar{v}(t)|^{p(x)} \right) dx, \quad \forall t > 0. \end{aligned} \quad (13)$$

Applying (7), we get the following inequality

$$\begin{aligned} & \int_{\Omega} \left(\frac{\gamma(x)}{m(x)} |\bar{v}(t)|^{m(x)} - \frac{\mu(x)}{p(x)} |D\bar{v}(t)|^{p(x)} \right) dx \leq \int_{\Omega} \left(\frac{\gamma(x)}{m^-} |\bar{v}(t)|^{m(x)} - \frac{\mu(x)}{p^+} |D\bar{v}(t)|^{p(x)} \right) dx \leq \\ & \leq \frac{1}{m^-} \int_{\Omega} \left(\gamma(x) |\bar{v}(t)|^{m(x)} - \mu(x) |D\bar{v}(t)|^{p(x)} \right) dx \leq \frac{1}{m^-} \Phi''(t), \quad \forall t > 0. \end{aligned}$$

Then, it follows from (13) that

$$0 < \int_0^t \left(\|\bar{v}_t\|_2^2 + \int_{\Omega} \chi(x) |D\bar{v}|^{q(x)-2} |D\bar{v}_t|^2 dx \right) d\tau \leq \frac{1}{m^-} \Phi''(t). \quad (14)$$

Next, applying the Hölder and Young inequalities together with (5), we derive the following chain of inequalities for $0 \leq t' < t$:

$$\begin{aligned} & \left[\Phi'(t) - \Phi'(t') \right]^2 = \left[\int_{t'}^t \Phi''(\tau) d\tau \right]^2 = \left[\int_{t'}^t \left(\int_{\Omega} \bar{v} \bar{v}_t dx + \int_{\Omega} \chi(x) |D\bar{v}|^{q(x)-2} D\bar{v} : D\bar{v}_t dx \right) d\tau \right]^2 \leq \\ & \left[\int_{t'}^t \left(\|\bar{v}\|_{2,\Omega} \|\bar{v}_t\|_{2,\Omega} + \left(\int_{\Omega} \chi |D\bar{v}|^{q(x)} dx \right)^{\frac{1}{2}} \left(\int_{\Omega} \chi |D\bar{v}|^{q(x)-2} |D\bar{v}_t|^2 dx \right)^{\frac{1}{2}} \right) d\tau \right]^2 \leq \\ & \left[\left(\int_{t'}^t \|\bar{v}\|_{2,\Omega}^2 d\tau \right)^{\frac{1}{2}} \left(\int_{t'}^t \|\bar{v}_t\|_{2,\Omega}^2 d\tau \right)^{\frac{1}{2}} + \left(\int_{t'}^t \int_{\Omega} \chi |D\bar{v}|^{q(x)} dx d\tau \right)^{\frac{1}{2}} \left(\int_{t'}^t \int_{\Omega} \chi |D\bar{v}|^{q(x)-2} |D\bar{v}_t|^2 dx d\tau \right)^{\frac{1}{2}} \right]^2 \leq \\ & \leq \int_{t'}^t \left(\|\bar{v}\|_2^2 + \int_{\Omega} \chi |D\bar{v}|^{q(x)} dx \right) d\tau \cdot \int_{t'}^t \left(\|\bar{v}_t\|_2^2 + \int_{\Omega} \chi |D\bar{v}|^{q(x)-2} |D\bar{v}_t|^2 dx \right) d\tau. \end{aligned} \quad (15)$$

It follows from (15) and (1), (2), that

$$\begin{aligned}
 & [\Phi'(t) - \Phi'(t')]^2 \leq \\
 & \leq \int_{t'}^t \left(2 \frac{1}{2} \|\bar{v}\|_2^2 + q^+ \int_{\Omega} \frac{\chi(x)}{q(x)} |D\bar{v}|^{q(x)} dx \right) d\tau \cdot \int_{t'}^t \left(\|\bar{v}_t\|_2^2 + \int_{\Omega} \chi(x) |D\bar{v}|^{q(x)-2} |D\bar{v}_t|^2 dx \right) d\tau \leq \\
 & \max\{2, q^+\} \Phi(t) \int_{t'}^t \left(\|\bar{v}_t\|_2^2 + \int_{\Omega} \chi(x) |D\bar{v}|^{q(x)-2} |D\bar{v}_t|^2 dx \right) d\tau \leq \\
 & \frac{\max\{2, q^+\}}{m^-} \Phi(t) \cdot \Phi''(t), \quad \forall t > t' > 0.
 \end{aligned} \tag{16}$$

We want to prove that the functional $\Phi(t)$ becomes unbounded (blows up) at a finite moment. Let us assume that for contradiction, the blow-up does not occur in a finite time, i.e. the nontrivial solution \bar{v} exists for all time $t > 0$. Since, $\Phi(t), \Phi'(t)$ and $\Phi''(t)$ are nonnegative, there exists a time $t' \geq 0$, such that they are strong positive for all $t \geq t'$, and it is necessary that $\Phi'(t) \rightarrow \infty$ as

$t \rightarrow \infty$. Notice that for every $\sigma \in \left(1, \frac{m^-}{2}\right)$

$$1 - \sqrt{\frac{2\sigma}{m^-}} \geq \frac{\Phi'(t')}{\Phi'(t)} \rightarrow 0 \text{ as } t \rightarrow \infty.$$

It follows that for every fixed $\sigma \in \left(1, \frac{m^-}{2}\right)$ there exists a moment $t_0 > t'$ such that

$$(\Phi'(t) - \Phi'(t'))^2 \geq \frac{2\sigma}{m^-} (\Phi'(t))^2$$

for all $t > t_0, \Phi(t_0) > 0$.

Using (15) and the last inequality, we get

$$\frac{2\sigma}{m^-} (\Phi'(t))^2 \leq (\Phi'(t) - \Phi'(t'))^2 \leq \frac{2}{m^-} \Phi''(t)\Phi(t)$$

for all $t > t_0$,

Hence

$$\sigma \frac{\Phi'(t)}{\Phi(t)} \leq \frac{\Phi''(t)}{\Phi'(t)} \Leftrightarrow (\ln \Phi^\sigma(t))' \leq (\ln \Phi'(t))' \Rightarrow$$

$$\left(\frac{\Phi'(t_0)}{\Phi^\sigma(t_0)} \right) \Phi^\sigma(t) \leq \Phi'(t) \text{ for all } t > t_0. \tag{17}$$

The direct integration of (17) leads to the inequality

$$\begin{aligned}
 \Phi^{\sigma-1}(t) & \geq \frac{\Phi^{\sigma-1}(t_0)}{1 - (t-t_0)(\sigma-1) \frac{\Phi'(t_0)}{\Phi(t_0)}} \rightarrow \infty \\
 \text{as } t \rightarrow T_{\max} & = t_0 + \frac{\Phi(t_0)}{(\sigma-1)\Phi(t_0)}.
 \end{aligned} \tag{18}$$

On the other hand, by using the above assumption on existence of a weak solution \bar{v} to the problem (1)-(4) for all time $t > 0$, we obtain that the functional $\Phi(t)$ is bounded at a finite moment T_{\max} :

$$\begin{aligned}
 \infty & > T_{\max} \sup_{t \in (0, T)} \left(\frac{1}{2} \|\bar{v}\|_2^2 + \frac{\chi}{2} \|\nabla \bar{v}\|_2^2 \right) \geq \\
 & \geq \int_0^t \left(\frac{1}{2} \|\bar{v}\|_2^2 + \frac{\chi}{2} \|\nabla \bar{v}\|_2^2 \right) d\tau \equiv \Phi(t)
 \end{aligned}$$

But this is impossible, because by (18) the functional $\Phi(t)$ is unbounded at a finite moment T_{\max} , i.e. $\Phi(t) \rightarrow \infty$, as $t \rightarrow T_{\max}$ and it contradicts the existence of a solution \bar{v} of the problem (1)-(4) for all time $t > 0$. Therefore, it follows from this contradiction that the weak solution to the problem (1)-(4) blows up in a finite time, and it completed the proof of the Theorem 1.

4. Conclusion

In this work, the nonlinear initial-boundary value problem for the generalized Kelvin-Voigt equations describing the motion of incompressible viscoelastic non-Newtonian fluids is considered. The equations has been generalized replacing the diffusion and relaxation terms in equation with $p(x)$ -Laplacian and $q(x)$ -Laplacian, respectively, and adding a nonlinear absorption term with variable exponents and coefficients.

The functional spaces with their norms and some necessary inequalities regarding to the variable exponents have been introduced. Under suitable conditions on exponents and coefficients, and on the data of the problem, the blowing up in a finite time property of weak solutions is established. As it is known from theory of PDE, this property means that the weak solutions of the problem do not exist global in time.

Acknowledgment

All authors were fully supported by the grant no. AP08052425 of Ministry of Education and Science of the Republic of Kazakhstan (MES RK), Kazakhstan.

References

1. Pavlovsky V.A. "On the theoretical description of weak water solutions of polymers." *Dokl Akad Nauk SSSR*. 200(4) (1971): 809-812.
2. Zvyagin V.G. and Turbin M.V. "The study of initial-boundary value problems for mathematical models of the motion of Kelvin-Voigt fluids." *J Math Sci*. 168 (2010): 157-308.
3. Astarita G., Marucciskolkov G. "Principles of Non-Newtonian Fluid Mechanics." *McGraw-Hill, London* (1974).
4. Oskolkov A.P. "The uniqueness and global solvability of boundary-value problems for the equations of motion for aqueous solutions of polymers." *J. Math. Sci.* 8 (1977): 427-455.
5. Oskolkov A.P. "Certain model nonstationary systems in the theory of non-Newtonian fluids." *Tr. Mat. Inst. Steklova* 127 (1975): 32-57 (in Russian).
6. Oskolkov A.P. "On the theory of unsteady flows of Kelvin-Voigt fluids." *J. Math. Sci.* 28(5) (1985): 751-758.
7. Oskolkov A.P. "Nonlocal problems for equations of Kelvin-Voigt fluids." *Zap. Nauch. Sem. LOMI*. 197 (1992): 120-158. Oskolkov A.P. "Nonlocal problems of motion for equations of the Kelvin-Voigt fluids." *J. Math. Sci.* 75(6) (1995): 2058-2078.
8. Oskolkov A.P. "Nonlocal problems for equations of Kelvin-Voigt fluids and their ϵ -approximations." *J Math Sci*. 87 (1997): 3393-3408.
9. Ladyzenskaya O.A. "On certain nonlinear problems of the theory of continuous media." *International Congress of Mathematicians Moscow, Abstracts of Reports* (1966): 149.
10. Karazeeva N.A. "Solvability of initial boundary value problems for equations describing the motions of linear viscoelastic fluids." *Journal of Applied Mathematics*. 1 (2005): 59--80.
11. Zvyagin V.G., Orlov V.P. "On weak solutions of the equations of motion of a viscoelastic medium with variable boundary." *Bound. Value Probl.* 3 (2005): 215--245.
12. Antontsev S.N., de Oliveira H.B., Khompysh Kh. Generalized Kelvin-Voigt equations for nonhomogeneous and incompressible fluids// COMMUN. MATH. SCI. c 2019 Vol. 17, No. 7, pp. 1915-1948.
13. Di H.F., Shang Y.D., Peng X.M. "Blow-up phenomena for a pseudo-parabolic equation with variable exponents." *Appl. Math. Lett.* 64 (2017): 67-73.
14. Al'shin A.B., Korpusov M.O., and Sveshnikov A.G., "Blow-up in nonlinear Sobolev type equations." *Gruyter, Series: De Gruyter Series in Nonlinear Analysis and Applications* 15 (2011): 62-77.
15. Cao Y., Nie Y. "Blow-up of solutions of the nonlinear Sobolev equation." *Applied Mathematical Letters* 28 (2014): 1-6.
16. Korpusov M.O., Sveshnikov A.G. "Blow-up of Oskolkov's system of equations." *Sb. Math.* 200(4) (2009): 549-572.
17. Antontsev S.N., de Oliveira H.B. "The Navier-Stokes problem modified by an absorption term." *Appl. Anal.* 12 (2010): 1805-1825.
18. Antontsev S.N., de Oliveira H.B. "Asymptotic behavior of trampling fluids." *Nonlinear Analysis: Real World Appl.* 19 (2014): 54-66.
19. Antontsev S.N., Diaz J.I., Shmarev S. "Energy methods for free boundary problems. Applications to nonlinear PDEs and fluid mechanics." *Birkhäuser Boston, Inc., Boston, MA*, (2002).
20. Antontsev S.N., Khompysh Kh. "Kelvin-Voigt equation with p-Laplacian and damping term: existence, uniqueness and blow-up." *J. Math. Anal. Appl.* 446 (2017): 1255-1273, <http://dx.doi.org/10.1016/j.jmaa.2016.09.023>

21. Antontsev S.N., Khompysh Kh. “Generalized Kelvin–Voigt equations with p-Laplacian and source/absorption terms.” *J. Math. Anal. Appl.* 456(1) (2017): 99-116.

22. Antontsev S.N., de Oliveira H.B. Khompysh Kh. “Kelvin-Voigt equations with anisotropic diffusion, relaxation, and damping: blow-up and large time behavior.” *Asymptotic Analysis.* 121(2) (2021): 125–157.

23. Levine H.A. “Some nonexistence and instability theorems for solutions of formally parabolic

equations of the form $Pu_t = -Au + F(u)$.” *Arch. Rational Mech. Anal.* 51 (1973): 371-386.

24. Antontsev S.N., Shmarev S. “Blow-up of solutions to parabolic equations with nonstandard growth conditions.” *J. Comput. Appl. Math.* 234 (2010): 2633–2645.

25. Lions J.-L. “Quelques m'ethodes de r'esolution des probl'emes aux limites non lin'earies.” *Dunod, Paris*, (1969).

© This is an open access article under the (CC)BY-NC license (<https://creativecommons.org/licenses/by-nc/4.0/>). Funded by Al-Farabi KazNU

D.B. Zhakebayev , A.S. Zhumali Al-Farabi Kazakh National University, Almaty, Kazakhstan
e-mail: Ainura.z89@gmail.com

(Received 26 April 2022; received in revised form 28 May 2022; accepted 07 June 2022)

Simulation of Ternary Fluid Mixtures Separation by Phase-Field Free Energy LBM

Abstract. This article reviews the mathematical and computer modeling of the process of ternary fluid mixture separation by free energy based phase field Lattice Boltzmann equations method. The process under study is considered in a limited area having the shape of a rectangle. Three different sets of fluid components with different structures are specified. The mathematical model constructed to describe this process is based on the Navier-Stokes equation for an incompressible fluid and the Cahn-Hilliard equation. The numerical model is built on the basis of LBM using the D2Q9 model. Numerical experiments were performed for two scenarios: (1) – investigate the model without gravity, in order to determine the patterns of the surface tension effect and (2) – investigate the model with gravity force. Numerical results showed a spinodal separation depending on the initial fractions of fluid concentrations. The results obtained determine the adequacy of the constructed model for a three-component fluid.

Key words. Three-component fluid, fluid mixtures separation, Cahn-Hilliard equation, free energy, lattice Boltzmann method.

Introduction

The study of multiphase and multicomponent flows dynamics is primarily necessary because they are often found in nature, and also take place in industrial and production processes, which requires a detailed study of a number of engineering problems. As an application example of numerical simulation of multiphase and multicomponent fluid flows, one can note the oil and gas production, the chemical processing of raw materials, as well as the steam-water mixture flows in boilers and condensers.

Various models can be used to model multiphase and multicomponent fluid flows [1-4]. Depending on the thickness of the transition layer between the phases, two main approaches can be distinguished: sharp interface models (transition layer between phases has zero thickness) and diffuse interface models (transition layer between the phases has a finite thickness). In our paper, we use the second approach. Van der Waals was the first to consider the transition layer between phases as a layer of finite thickness [5]. Currently, the Cahn-Hilliard approach

[6] is widely used to describe the diffuse interface models.

This paper presents a mathematical model of incompressible three-component fluid flow using the phase field method based on the solution of the complete Navier-Stokes equation and the Cahn-Hilliard convective equation. The numerical model is based on free energy LBM using the D2Q9 scheme. The accuracy and efficiency of the existing method have been tested on the basis of solving a number of problems. The results obtained determine the correctness of the constructed model for a three-component fluid.

Problem statement

The process under study is considered in a limited area having the shape of a rectangle with dimensions $[0, L] \times [0, L]$ (Figure1). In this area there are three fluid components with density ρ_1, ρ_2 and ρ_3 , the ratio of which is: $\rho_1 > \rho_2 > \rho_3$. A less dense fluid is indicated in blue, a medium density fluid in green, and a denser fluid in red.

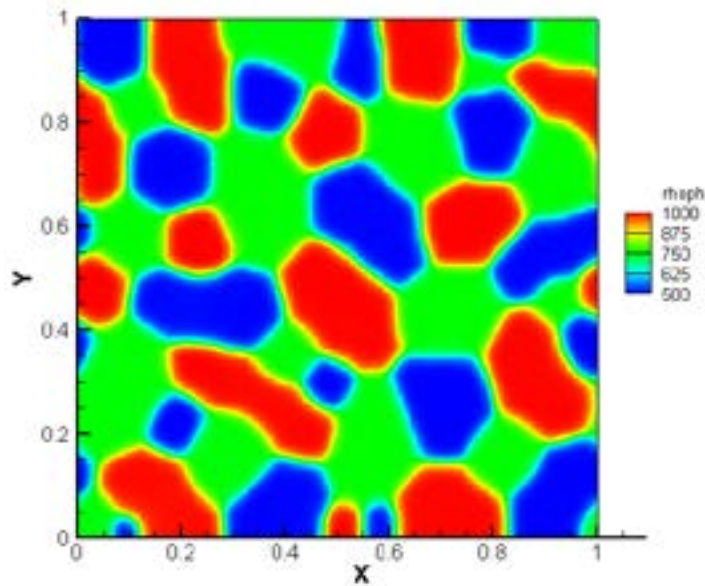


Figure 1 – Scheme of the computational domain

The mathematical model of the process includes the continuity equation, the momentum equation for the mixture and the Cahn-Hilliard convective equation:

$$\begin{aligned} \nabla \cdot \vec{u} &= 0, \\ \frac{\partial(\rho \vec{u})}{\partial t} + \nabla(\rho \vec{u} \vec{u}) &= \\ &= -\nabla p + \nabla[\eta(\nabla \vec{u} + \nabla \vec{u}^T)] + F_s + \vec{F}_b, \\ \frac{\partial(c_i)}{\partial t} + \nabla(c_i \vec{u}) &= \nabla(M_i \nabla \mu_i), i = 1, 2, 3 \end{aligned} \quad (1)$$

where \vec{u} are the velocity components, p is the pressure, ρ is the density, η is the dynamic viscosity, c_i is the phase field for the fluid components: $c_1 + c_2 + c_3 = 1$, \vec{g} is the gravitational acceleration, M_i is the mobility coefficient, μ_i is the chemical potential, $\vec{F} = F_s + \vec{F}_b = \sum_{i=1}^3 \mu_i \nabla c_i + \rho \vec{g}$ is the total force of surface tension and gravity.

For a system of a multicomponent medium, the

$$\mu_1 = 2\beta_{11}(-28c_1^3 + 18c_1^2 - 2c_1) + 2\beta_{12}(-4c_2^3 - 12c_1^2c_2 - 12c_1c_2^2 + 6c_2^2 + 12c_1c_2 - 2c_2) + 2\beta_{13}(-4c_3^3 - 12c_1^2c_3 - 12c_1c_3^2 + 6c_3^2 + 12c_1c_3 - 2c_3) - (\lambda_{11}\nabla^2c_1 + \lambda_{12}\nabla^2c_2 + \lambda_{13}\nabla^2c_3),$$

$$\mu_2 = 2\beta_{21}(-4c_1^3 - 12c_1^2c_2 - 12c_1c_2^2 + 6c_1^2 + 12c_1c_2 - 2c_1) + 2\beta_{22}(-28c_2^3 + 18c_2^2 - 2c_2) + 2\beta_{23}(-4c_3^3 - 12c_2^2c_3 - 12c_2c_3^2 + 6c_3^2 + 12c_1c_3 - 2c_3) - (\lambda_{21}\nabla^2c_1 + \lambda_{22}\nabla^2c_2 + \lambda_{23}\nabla^2c_3),$$

Landau free energy functional F can be determined based on the concentrations of fluids as follows [7]:

$$F(c, \nabla c) = \int \left[F_0(c) + \sum_{i,j=1}^3 \frac{\lambda_{ij}}{2} \nabla c_i c_j \right] d\Omega$$

where $F_0(c) = \sum_{i,j=1}^3 \beta_{ij}[g(c_i) - g(c_j) - g(c_i + c_j)]$ is the bulk free energy, $c = (c_1, c_2, c_3)$ is the phase variable of fluid components, $g(c) = c^2(1 - c)^2$, $\beta_{ij} = \frac{3}{D}\sigma_{ij}$ and $\lambda_{ij} = -\frac{3D}{4}\sigma_{ij}$ are the constants, where σ_{ij} is the surface tension between the fluids and D is the thickness of the transition layer between fluids.

The variation of the free energy function F with respect to the concentration fractions c of fluids yields the chemical potential μ_i for component i as

$$\mu_3 = 2\beta_{31}(-4c_1^3 - 12c_1^2c_3 - 12c_1c_3^2 + 6c_1^2 + 12c_1c_3 - 2c_1) + 2\beta_{22}(-4c_2^3 - 12c_2^2c_3 - 12c_1c_3^2 + 6c_2^2 + 12c_2c_3 - 2c_1) + 2\beta_{33}(-28c_3^3 + 18c_3^2 - 2c_3) - (\lambda_{31}\nabla^2c_1 + \lambda_{32}\nabla^2c_2 + \lambda_{33}\nabla^2c_3).$$

We substitute the above chemical potential μ_i for component i into the equation (1), as a result, the system will be complete. The system of equations (1) has the following initial conditions:

$$u = v = 0,$$

$$c_1(\vec{x}, 0) = \bar{c}_1 + \alpha \times rand(\vec{x})$$

$$c_2(\vec{x}, 0) = \bar{c}_2 + \alpha \times rand(\vec{x})$$

$$c_3(\vec{x}, 0) = 1 - c_1(\vec{x}, 0) - c_2(\vec{x}, 0)$$

Boundary conditions:

On the bottom wall at $y = 0$:

$$u = v = 0, \quad \frac{\partial c_1}{\partial y} = \frac{\partial c_2}{\partial y} = \frac{\partial c_3}{\partial y} = 0.$$

On the side walls at $x = 0, L$:

for u, v, c_1, c_2, c_3 – periodic boundary conditions.

On the bottom wall at $y = L$:

$$u = v = 0, \quad \frac{\partial c_1}{\partial y} = \frac{\partial c_2}{\partial y} = \frac{\partial c_3}{\partial y} = 0.$$

Numerical method

The numerical solution of this model is based on the D2Q9 scheme of the lattice Boltzmann equations method. The lattice Boltzmann equation in the Batnagar-Gross-Krook (BGK) approximation is written as follows:

$$f_i(\vec{x} + \vec{e}_i\Delta t, t + \Delta t) - f_i(\vec{x}, t) = \Delta t \left[-\frac{f_i(\vec{x}, t) - f_i^{eq}(\vec{x}, t)}{\tau_f} + F_i \right]$$

$$g_i^m(\vec{x} + \vec{e}_i\Delta t, t + \Delta t) - g_i^m(\vec{x}, t) = \frac{\Delta t}{\tau_m} [g_i^m(\vec{x}, t) - g_i^{m,eq}(\vec{x}, t)]$$

where $m = 1, 2, 3$ – fluid components, f_i, g_i^m – velocity and phase field distribution functions, e_i – discrete lattice velocity, $\tau_f = \frac{1}{2} + c_1\left(\tau_1 - \frac{1}{2}\right) + c_2\left(\tau_2 - \frac{1}{2}\right) + (1 - c_1 - c_2)\left(\tau_3 - \frac{1}{2}\right)$, $\tau_m = 0.8$ –

relaxation times, F_i – force component, Δt – lattice time step, $f_i^{eq}, g_i^{m,eq}$ – equilibrium distribution functions for velocity field and phase field, respectively.

The equilibrium distribution functions are determined by the following formulas [8]

$$f_i^{eq} = \begin{cases} \rho - \sum_{i \neq 0} f_i^{eq}, & i = 0 \\ \omega_i \rho \left(1 + \sum_{m=1}^3 \frac{c_m \mu_m}{\rho c_s^2} + \frac{e_{i\alpha} u_\alpha}{c_s^2} + \frac{u_\alpha u_\beta (e_{i\alpha} e_{i\beta} - c_s^2 \sigma_{\alpha\beta})}{2c_s^2} \right), & i \neq 0 \end{cases}$$

$$g_i^{m,eq} = \begin{cases} c_m - \sum_{i \neq 0} g_i^{m,eq}, & i = 0 \\ \omega_i \left(\frac{\Gamma_m \mu_m}{c_s^2} + \frac{c_m e_{i\alpha} u_\alpha}{c_s^2} + \frac{c_m u_\alpha u_\beta (e_{i\alpha} e_{i\beta} - c_s^2 \sigma_{\alpha\beta})}{2c_s^2} \right), & i \neq 0 \end{cases}$$

where $c_s = c/\sqrt{3}$ is the lattice speed of sound, $c = \Delta x / \Delta t$, Δx and Δt are the lattice space and time steps, which are equal to unity.

In the D2Q9 model the discrete velocities are

calculated using the formulas

$$e_{ix} = (0, 1, 1, 0, -1, -1, -1, 0, 1)c$$

$$e_{iy} = (0, 0, 1, 1, 1, 0, -1, -1, -1)c$$

The values of weight coefficients are as follows

$$\omega_i = \begin{cases} \frac{4}{9}, i = 0, \\ \frac{1}{9}, i = 1 - 4, \\ \frac{1}{36}, i = 5 - 8 \end{cases}$$

In this paper, to add the force term $\vec{F} = F_s + \vec{F}_b = \sum_{i=1}^3 \mu_i \nabla c_i + \rho \vec{g}$ to LBM we apply the scheme suggested by Guo et al. [9]

$$F_i = \omega_i \left(1 - \frac{\Delta t}{2\tau_f} \right) \left[\frac{\vec{e}_i - \vec{u}}{c_s^2} + \frac{\vec{e}_i (\vec{e}_i \cdot \vec{u})}{c_s^4} \right] \cdot \vec{F}$$

Equations for the distribution functions can be divided into two steps, collision and streaming:

$$f_i^*(\vec{x}, t) = f_i(\vec{x}, t) + \Delta t \left(-\frac{f_i(\vec{x}, t) - f_i^{eq}(\vec{x}, t)}{\tau_f} + F_i \right)$$

$$g_i^{m,*}(\vec{x}, t) = g_i^m(\vec{x}, t) + \Delta t \left(-\frac{g_i^m(\vec{x}, t) - g_i^{m,eq}(\vec{x}, t)}{\tau_c} \right)$$

$$f_i(\vec{x} + \vec{e}_i \Delta t, t + \Delta t) = f_i^*(\vec{x}, t)$$

$$g_i^m(\vec{x} + \vec{e}_i \Delta t, t + \Delta t) = g_i^{m,*}(\vec{x}, t)$$

After the second step, it is necessary to calculate the macroscopic variables for density, velocity and phase field:

$$\rho = \sum_{i=0}^8 f_i, \rho \vec{u} = \sum_{i=0}^8 f_i \vec{e}_i + \frac{\Delta t}{2} \vec{F}, c_m = \sum_{i=0}^8 g_i^m$$

Derivatives of macroscopic c_i are calculated using the following second-order isotropic differences [7]:

$$\nabla^2 c_m(\vec{x}, t) = \sum_{i=1}^8 \frac{2\omega_i [c_m(\vec{x} + \vec{e}_i \Delta t, t) - c_m(\vec{x}, t)]}{c_s^2 \Delta t^2}$$

For the velocity field, as the no-slip boundary condition in fixed walls (\vec{x}_w) the bounce back scheme is used [10]:

$$f_i(\vec{x}_w, t + \Delta t) = f_{-i}(\vec{x}_w, t + \Delta t), \quad \vec{e}_i \cdot \vec{n} > 0,$$

where the phase is constant and the boundary conditions for the concentration distribution functions are chosen as follows:

$$g_i^m(\vec{x}_w, t + \Delta t) = g_{-i}^m(\vec{x}_w, t + \Delta t) + 2\omega_i c_w, \quad \vec{e}_i \cdot \vec{n} > 0,$$

where c_w – near-wall phase.

The Neumann condition for the phase on all other walls:

$$g_i^m(\vec{x}_w, t + \Delta t) = g_{-i}^m(\vec{x}_w, t + \Delta t), \quad \vec{e}_i \cdot \vec{n} > 0.$$

Algorithm for applying the lattice Boltzmann equations method [11]:

- 1) Discretization of the physical domain and non-dimensionalization of the related parameters
- 2) Choice of simulation parameters
- 3) Domain initialization
- 4) Executing the collision step
- 5) Application of the boundary conditions
- 6) Executing the streaming step
- 7) Calculation of the macroscopic parameters.

Simulation results

We consider the evolution of the ternary fluid mixture in a rectangular computational domain with dimensions: $N_x \times N_y$, $N_x = 80, N_y = 80$. The physical size of the length is $L = 0.01$ m. The space and time steps are defined as $\Delta x = \frac{L}{N_x} = 0,000125, \Delta t = 0.000117188$.

Physical quantities: the density – $\rho_1 = 1000 \frac{kg}{m^3}$, $\rho_2 = 750 \frac{kg}{m^3}$, $\rho_3 = 500 \frac{kg}{m^3}$ and the viscosity – $\mu_1 = \mu_2 = \mu_3 = 0.01 Pa \cdot s$, the acceleration of gravity – $g = 9.8 \frac{m}{s^2}$. Dimensionless quantities: Reynolds number – $Re = 234.787$, the capillarity number – $Ca = 0.000417399$ and Atwood number $A = 0.142857$.

Computer simulation by the lattice Boltzmann equations method is performed in lattice units, i.e. the physical parameters of the model are replaced by their lattice analogs using transformation coefficients $Cu = 1.06667$, $Cg = 9102.22$. LBM parameters: the density – $\rho_1 = 1.33, \rho_2 = 1, \rho_3 = 0.67$, relaxation times – $\tau_1 = \tau_2 = \tau_3 = 0.8$, the surface tension – $\sigma_{12} = \sigma_{13} = \sigma_{23} = 0.01$, the surface thickness – $D = 2$, the acceleration of gravity – $g = 0.00107666$, and $U_{lbm} = 0.293484$.

The simulation results (Figure 2, 3) show the dynamic change of fluids – the mixture separation of immiscible fluids depending on the fractions of fluid concentrations. The average values of the concentration fractions are taken equal to $(\bar{c}_1, \bar{c}_2, \bar{c}_3) =$

$(0.4, 0.2, 0.4)$, $(\frac{1}{3}, \frac{1}{3}, \frac{1}{3})$, $(0.25, 0.25, 0.5)$. In the first scenario (Figure 2), which does not take into account the acceleration of gravity, one can see the spinodal decomposition of the mixture over time, resulting from the influence of surface tension between the fluids.

In the second scenario (Figure 3), which takes into account the acceleration of gravity, at an early stage ($T < 1$ s) a less dense fluid ($\rho_3 = 500$) begins to rise, while a denser fluid ($\rho_1 = 1000$) begins its downward movement. Eventually, stable three layers of fluid components are formed: the denser fluid at the bottom and the less dense fluid at the top.

The results obtained determine the adequacy of the constructed model for a three-component fluid.

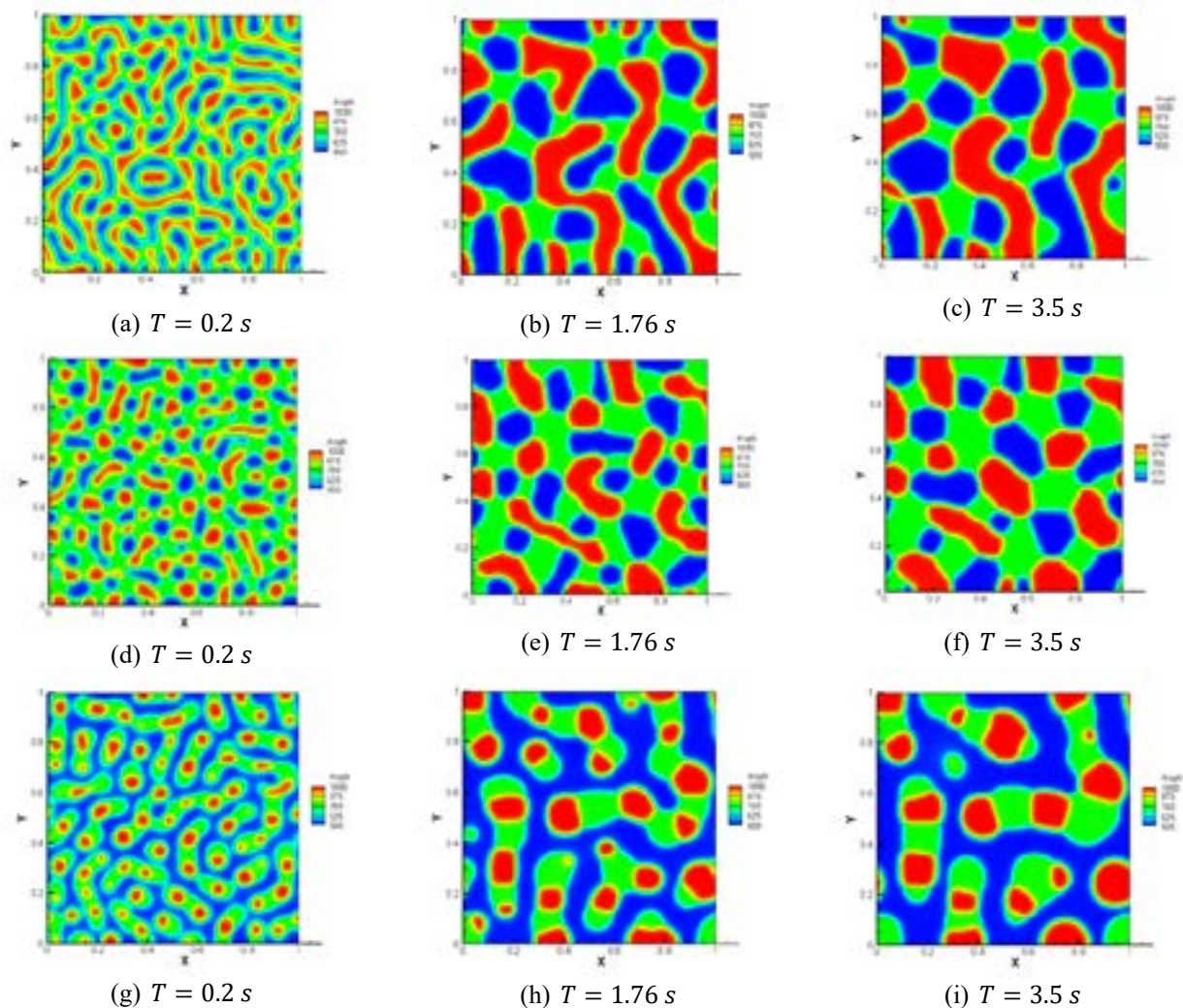


Figure 2 – Ternary fluid separation depending on time for different fractions of fluid concentrations: (a)-(c) $(\bar{c}_1, \bar{c}_2, \bar{c}_3) = (0.4, 0.2, 0.4)$, (d)-(f) $(\bar{c}_1, \bar{c}_2, \bar{c}_3) = (\frac{1}{3}, \frac{1}{3}, \frac{1}{3})$, (g)-(i) $(\bar{c}_1, \bar{c}_2, \bar{c}_3) = (0.25, 0.25, 0.5)$.

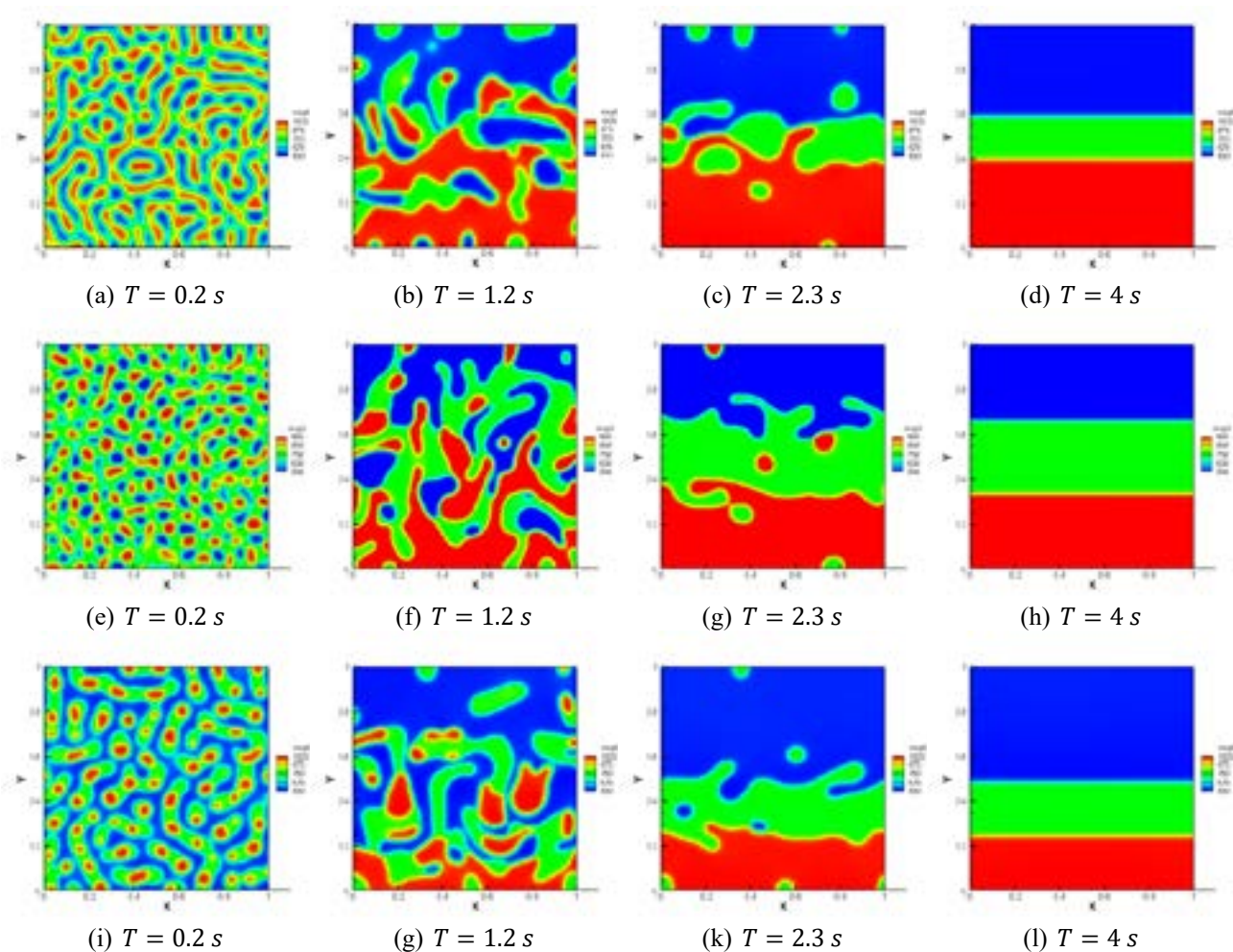


Figure 3 – Effect of body force on the time evolution of density contours of a ternary fluid mixture for different fluid concentration fractions: (a)-(d) $(\bar{c}_1, \bar{c}_2, \bar{c}_3) = (0.4, 0.2, 0.4)$, (e)-(h) $(\bar{c}_1, \bar{c}_2, \bar{c}_3) = (\frac{1}{3}, \frac{1}{3}, \frac{1}{3})$, (i)-(l) $(\bar{c}_1, \bar{c}_2, \bar{c}_3) = (0.25, 0.25, 0.5)$.

Conclusion

The paper proposes a mathematical and numerical model for studying the separation process of a three-component fluid. To implement this model, a 2D numerical algorithm has been developed based on the D2Q9 scheme of lattice Boltzmann equations method in a limited cavity in the shape of a rectangle. Numerical simulation was carried out with and without taking into account gravity. The results of numerical simulation showed that, depending on the initial fractions of fluid concentrations, spinodal separation occurs in different ways. From a physical point of view, this is explained by the effect of surface tension between fluids. Due to the influence of gravity, over time, denser, medium-density and less dense fluids begin to arrange themselves in

order, from bottom to top, respectively. The stability of the process sets in when the denser fluid component moves down completely. The results of this paper prove the applicability of the methods used in the paper for solving problems of this type.

Acknowledgement

The authors were supported by the Ministry of Education and Science of the Republic of Kazakhstan Grant No. AP08053154.

References

1. Shan X., Chen H. "Lattice Boltzmann model for simulating flows with multiple phases and components" *Phys. Rev. E* 47 (1993): 1815-1839.

2. He X., Chen S., Zhang R. "A Lattice Boltzmann scheme for incompressible multiphase flow and its application in simulation of Rayleigh-Taylor instability" *J. Comput. Phys.* 152 (1999): 642-663.
3. Rothman D.H., Keller J.M. "Immiscible cellular-automaton fluids" *J. Stat. Phys.* 52 (1988): 1119-1127.
4. Kim J. "Phase fluid models for multi-component fluid flows" *Commun. Comput. Phys.* 12, No 3 (2012): 613-661.
5. Waals J. van der. "The thermodynamic theory of capillarity under the hypothesis of a continuous variation of density" *Journal of Statistical Physics* 20 (1979): 200-244.
6. Cahn J. W., Hilliard J. E. "Free Energy of a Nonuniform System. I. Interfacial Free Energy" *J. Chem. Phys.* 28 (1958): 258-267.
7. Zheng L., Zheng S., and Zhai Q. "Multiphase flows of N immiscible incompressible fluids: Conservative Allen-Cahn equation and lattice Boltzmann equation method" *Physical review E* 101 (2020).
8. Kruger T., Kusumaatmaja H., Kuzmin A., Shardt O. and Silva G., Vigen E.M. *The Lattice Boltzmann-Method.*: Springer International Publishing 258, 2017.
9. Guo Z., Zheng C., Shi B. "Discrete lattice effects on the forcing term in the lattice Boltzmann method" *Phys. Rev. E.* 65 (2002): 1-6.
10. Wang P., Zhang Y., Guo Z. "Numerical study of three-dimensional natural convection in a cubical cavity at high Rayleigh numbers" *International Journal of Heat and Mass Transfer* 113 (2017): 217-228.
11. Zhumali A.S., Satenova B.A., Karuna O.L. "Lattice Boltzmann method simulation of thermal flow dynamics in a channel" *International Journal of Mathematics and Physics* 10, No 1 (2019): 75-81. DOI: <https://doi.org/10.26577/ijmph-2019-i1-10>

© This is an open access article under the (CC)BY-NC license (<https://creativecommons.org/licenses/by-nc/4.0/>). Funded by Al-Farabi KazNU

M. Odsuren^{1,2*} , G. Khuukhenkhoo² , Ch. Saikhanbayar² ,
S. Davaa² , O. Odgerel¹ , N. Baljinnyam³ 

¹School of Engineering and Applied Sciences, National University of Mongolia, Ulaanbaatar, Mongolia

²Nuclear Research Center, National University of Mongolia, Ulaanbaatar, Mongolia

³Central Geological Laboratory, Ulaanbaatar, Mongolia

*e-mail: odsuren@seas.num.edu.mn

(Received 29 April 2022; accepted 25 May 2022)

Scattering phase shifts of lithium isotopes

Abstract. Investigation of few body cluster systems is very important in nuclear physics. Problems appearing in few body systems can in principle be divided into two classes: bound state problems and scattering problems. The bound state problems are usually related to the spectroscopy of such systems while scattering problems describe their reactions. The main focus in the work is the scattering problem for systems consisting of two cluster systems. The single channel two body scattering problem is considered in the framework of different spin parity states for lithium isotopes.

Scattering phase shifts on negative and positive parity states of ${}^5\text{Li}$, ${}^6\text{Li}$ and ${}^7\text{Li}$ nuclei are calculated applying two-body $\alpha + p$, $\alpha + d$ and $\alpha + t$ systems and the complex scaling method. ${}^6\text{Li}$ and ${}^7\text{Li}$ are stable nuclei and their ground and low-lying excited states are considered in this work.

In this study, we calculated scattering phase shifts of the negative parity $J^\pi = 3/2^-$ and $J^\pi = 1/2^-$ states for p -wave of ${}^5\text{Li}$, $J^\pi = 7/2^-, 5/2^-, 3/2^-$ and $1/2^-$ states for p - and f -waves of ${}^7\text{Li}$ and the positive parity $J^\pi = 1^+, 2^+, 3^+$ states for s - and d -waves of ${}^6\text{Li}$.

Key words: phase shifts, structure of light nuclei, two-body system, low-lying excited states, ground state.

Introduction

During last several decades, scientists have tried and failed to provide a complete solution to scattering in complex nuclear system, one of the most fundamental phenomena in nuclear physics. Nuclear physics is one of the most rapidly developing fields of natural science in terms of theoretical and experimental research, many important and interesting issues remain still unclear in this area. The nuclei are complex objects consisting of several interacting nucleons where neutrons and protons have been arranged with different combinations. Light nuclei have exotic properties owing to peculiarities of the nuclear forces and quantum states of nucleon systems. To understand the characteristic properties of every nucleus, we use appropriate nuclear models and effective nuclear and Coulomb interactions [1-2].

The nuclear models can contain quasistationary or virtual states of nuclei, as well as their excited states located on the complex energy plane close to the real physical region of existence of the nuclei [3-7]. Nuclear models not only focused on the description of nuclear structures and reactions, but also considered nuclear fission and nuclear decay. At the beginning of development for nuclear models, it was known that the nucleons tend to group into clusters were extremely important in determining the structure of light nuclei. Consequently, the cluster structure of nucleus ground and excited (resonance or virtual) states became the focus of theoretical and experimental studies. Light nuclei are loosely bound and change their configurations when they interact with nucleons or other nuclei at relatively small distances. It was informed that a nucleus cluster structure is displayed in reactions with neutrons at low energies and with protons at energies higher than

Coulomb potential barrier. In the reactions of neutron scattering for various nucleus in the low-energy region is quite well measured by experimentally but the measured data for proton scattering on light nuclei at low energies is rare.

In this work, we apply the complex scaling method (CSM) [8-9] to the $\alpha + p$, $\alpha + d$ and $\alpha + t$ two-body models for obtaining ground and low-lying excited states of ${}^5\text{Li}$, ${}^6\text{Li}$ and ${}^7\text{Li}$ nuclei. Applying the CSM and $\alpha + p$ two-body model for the $J^\pi = 3/2^-$ and $1/2^-$ states of ${}^5\text{Li}$, $\alpha + d$ two-body model for the $J^\pi = 1^+$, 2^+ , 3^+ states of ${}^6\text{Li}$ and $\alpha + t$ two-body model $J^\pi = 7/2^-$, $5/2^-$, $3/2^-$ and $1/2^-$ states of ${}^7\text{Li}$.

For $\alpha + p$ and $\alpha + t$ systems the negative parity states of $p -$ and $f -$ waves are considered for the calculation of scattering phase shifts. The phase shifts for positive parity states in $s -$ and $d -$ waves of $\alpha + d$ system is calculated.

Complex Scaling Method and Two Body Model

The *Schrödinger* equation, $\hat{H}\Psi = E\Psi$, is transformed as

$$H^\theta \psi^\theta = E^\theta \psi^\theta, \quad (1)$$

where the complex scaled wave function is defined as

$$\psi^\theta = U(\theta)\Psi = e^{\frac{3}{2}i\theta}\Psi(re^{i\theta}). \quad (2)$$

The factor $e^{\frac{3}{2}i\theta}$ comes from the Jacobian of the coordinate transformation for r . The Hamiltonian in Eq. (1) is

$$H^\theta = U(\theta)HU^{-1}(\theta). \quad (3)$$

To solve Eq. (1), we expand the wave functions $\psi^\theta(k, r)$ to a finite number of L^2 basis functions, the Gaussian basis functions $u_i(r)$ for $i = 1, 2, \dots, N$,

$$\psi^\theta(k, r) = \sum_i^N c_i(k, \theta) u_i(r, b_i). \quad (4)$$

The coefficients $c_i(k, \theta)$ and the discrete spectra are obtained by solving the eigenvalue problem

$$\sum_i^N H_{ij}^\theta c_j(k, \theta) = E^\theta c_i(k, \theta), \quad (5)$$

$$H_{ij}^\theta = \langle \tilde{u}_i | H^\theta | u_j \rangle, \quad (6)$$

where H_{ij}^θ are the matrix elements of the complex scaled Hamiltonian given in Eq. (3).

Applying the CSM to two-body $\alpha + p$ model the Hamiltonian is expressed as

$$\hat{H} = \sum_{i=1}^2 \hat{T}_i - \hat{T}_{c.m.} + V_{ap}^{Nucl}(r) + V_{ap}^{Coul}(r), \quad (7)$$

where \hat{T}_i and $\hat{T}_{c.m.}$ are the kinetic energy operators of the i -th cluster and the center-of-mass of the total system, respectively. V_{ap}^{Nucl} is alpha-proton potential, $V_{ap}^{Coul}(r)$ is Coulomb potential. For the $\alpha + d$ and $\alpha + t$ two-body models the same Hamiltonian given in Eq. (7) is applied.

For each partial wave, we use Gaussian functions with different size parameters as basis functions

$$u_i^\ell(r, b_i) = N_\ell(b_i) r^\ell \exp\left(-\frac{1}{2b_i^2} r^2\right), \quad (8)$$

$$N_\ell(b_i) = \frac{1}{b_i^{\ell+3/2}} \left\{ \frac{2^{\ell+2}}{(2\ell+1)!! \sqrt{\pi}} \right\}^{1/2}, \quad (9)$$

where the parameters ($b_i: i = 1, 2, \dots, N$) are give by a geometrical progression of the form

$$b_i = b_0 \gamma^{i-1}, \quad (10)$$

where b_0 and γ are the first term and the common ratio, respectively.

Results and Discussion

$\alpha + p$ two body system

Phase shifts of the elastic scattering of proton from an alpha particle are shown in Figure 1. Calculated phase shifts for the $J^\pi = 3/2^-$ and $J^\pi = 1/2^-$ states generated by the total orbital momentum $L = 1$, which has a resonant state for each partial state. We obtained resonance state energy 0.74 MeV with decay width 0.59 MeV for $J^\pi = 3/2^-$ and resonance state energy 2.10 MeV and its decay width 5.82 MeV for $J^\pi = 1/2^-$ states. As can be seen from Figure 1 a), a narrow decay width state is calculated for the $J^\pi = 3/2^-$ state and the calculated scattering phase shifts of the $J^\pi = 3/2^-$ state increases rapidly from 1 MeV due to the small decay width. A resonance energy with large decay width for the $J^\pi = 1/2^-$ state is obtained and the calculated phase shifts approaches $\pi/2$ which shows a clear resonance behavior in Figure 1 b).

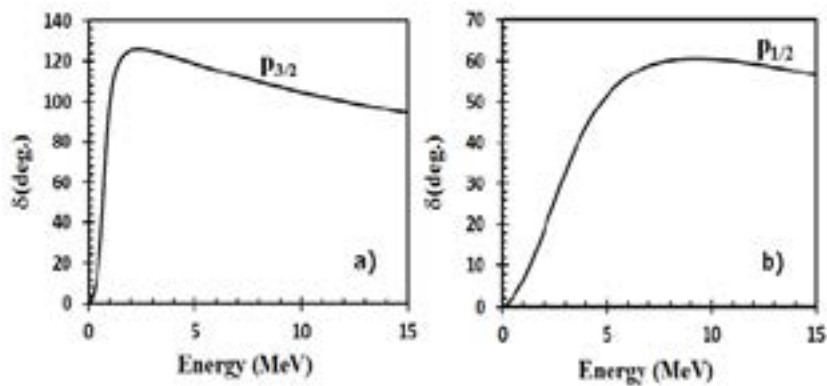


Figure 1 –The scattering phase shifts of $\alpha + p$ system / for $J^\pi = 3/2^-$ (a) and $J^\pi = 1/2^-$ (b).

$\alpha + d$ two body system

${}^6\text{Li}$ is a stable nucleus and excited energy levels are observed by experimentally. Calculated phase shifts for the elastic $\alpha + d$ scattering of the orbital momentum $L = 0$ and 2, the total angular momentum J are presented in Figure 2. In this calculation we consider only even parity states of ${}^6\text{Li}$

and ignored odd parity states because phase shifts for negative parity states are very small as comparing with even parity states. The $J^\pi = 1^+$ for the orbital momentum $L = 0$ is a ground state of ${}^6\text{Li}$. The calculated phase shifts of the $J^\pi = 1^+$ for $L = 0$ indicate an attractive interaction nature and it is displayed by dotted line in Figure 2.

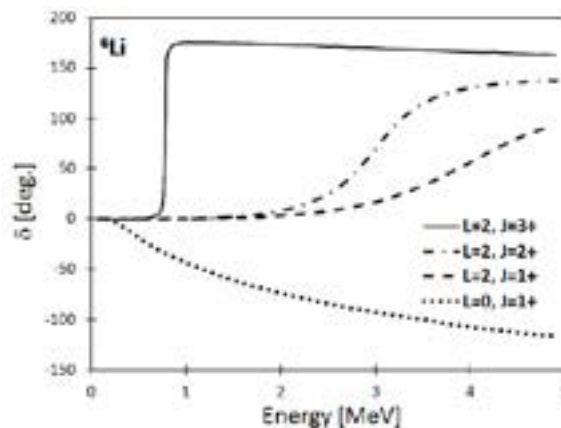


Figure 2 – The scattering phase shifts of $\alpha + d$ system of the $J^\pi = 1^+$ state for $L = 0$, and the $J^\pi = 3^+, 2^+, 1^+$ states for $L = 2$. The dotted, dashed, dotted-dashed and solid lines denote the calculated phase shifts of the $J^\pi = 1^+$ state for $L = 0$, and the $J^\pi = 1^+, 2^+, 3^+$ states for $L = 2$, respectively.

In the case of the $J^\pi = 3^+$ state for $L = 2$, the resonance energy is obtained and the calculated phase shifts for this state shows a sharp resonance behavior because of the very small resonance width. The calculated phase shifts of the $J^\pi = 3^+$ state increases sharply ~ 1 MeV and it approaches π which is displayed by solid line in Figure 2, and it implies a resonance state with small decay width. In Figure 2,

the dotted-dashed and dashed lines represent the calculated phase shifts of the $J^\pi = 2^+$ and $J^\pi = 1^+$ states for $L = 2$, respectively. It can be seen from Figure 2, the calculated phase shifts for the $J^\pi = 2^+$ and $J^\pi = 1^+$ states express resonance behavior. Phase shifts of the $J^\pi = 2^+$ state presents by the dotted-dashed line, and it increases gradually from 3 MeV and approaches $5\pi/6$. The dashed line

expresses the calculated phase shifts of the $J^\pi = 1^+$ state and it increases smoothly from 4.5 MeV and approaches $\pi/2$.

$\alpha + t$ two body system

We display phase shifts of the elastic $\alpha + t$ scattering in Figure 3. In this time, we study only negative parity states of ${}^7\text{Li}$ for $L = 1$, and 3 waves. The positive parity states are negligibly small as comparing with odd parity states.

Due to the Coulomb interaction, phase shifts are very small at the energy range $0 < E < 0.5$ MeV.

Phase shifts for the negative parity state and for the total angular momentum $J^\pi = 7/2^-$ and $J^\pi = 5/2^-$ for $L = 3$ exhibit a resonance behavior which approach π and $5\pi/6$. As can be seen from Figure 3, the solid line expresses the calculated phase shifts of the $J^\pi = 7/2^-$ state and it implies a sharp resonance state obtained. The dotted-dashed line displays the results of the $J^\pi = 5/2^-$ state and it shows resonance behavior too.

The phase shifts of the $J^\pi = 3/2^-$ and $J^\pi = 1/2^-$ state for $L = 1$ are drawn by dotted and dashed lines in Figure 3. The phase shifts behaviors for $L = 1$ state show attractive nature.

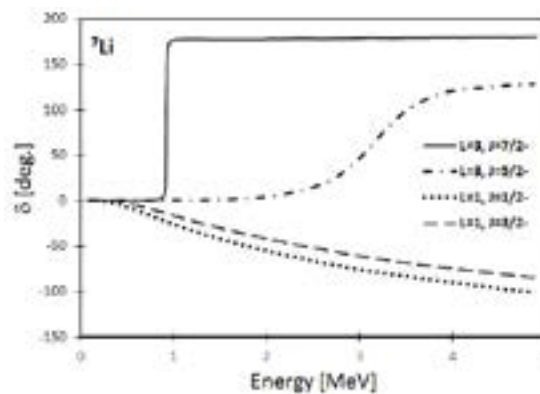


Figure 3 – The scattering phase shifts of $\alpha + t$ system of the $J^\pi = 3/2^-$ and $J^\pi = 1/2^-$ state for $L = 1$ and the $J^\pi = 7/2^-, 5/2^-$ states for $L = 3$.

The dotted, dashed, dotted-dashed and solid lines denote the calculated phase shifts of the $J^\pi = 3/2^-$ and $J^\pi = 1/2^-$ state for $L = 1$ and the $J^\pi = 7/2^-, 5/2^-$ states for $L = 3$.

Conclusions

In this work we discussed the calculated scattering phase shifts for the different spin parity states of ${}^5\text{Li}$, ${}^6\text{Li}$ and ${}^7\text{Li}$ nuclei applying two body model. The negative parity states of $L = 1$ and $L = 3$ waves are considered for $\alpha + p$ and $\alpha + t$ systems. The scattering phase shifts are calculated in positive parity states of $L = 0$ and $L = 2$ waves for $\alpha + d$ system.

The $J^\pi = 3/2^-$ and $J^\pi = 1/2^-$ states of $\alpha + p$ system have a resonant state for each partial state and the calculated phase shifts show resonance behavior.

We calculate scattering phase shifts of $\alpha + d$ system for $L = 0$ and 2 waves where only even parity states are considered. The phase shifts for negative parity states are very small as comparing with even parity states in $\alpha + d$ system. ${}^6\text{Li}$ has the ${}^3\text{He} + t$ cluster configuration and it reported in Ref.

[10], the $({}^3\text{He} + t)$ configuration of ${}^6\text{Li}$ is only slightly less probable than the $(\alpha + d)$ configuration.

${}^7\text{Li}$ nuclei is modelled as $\alpha + t$ two clusters and scattering phase shifts of $L = 1$, and 3 waves are calculated. The positive parity states are negligibly small as comparing with odd parity states in $\alpha + t$ system.

Acknowledgments

The numerical calculation was supported by the MINATO cluster computing system at the Nuclear Research Center, National University of Mongolia.

References

1. Freer M. "Clustering in Light Nuclei: from the Stable to the Exotic". *Lecture Notes in 47 Physics* Vol.879 (2014).

2. Beck C. *Clusters in Nuclei*. Berlin: Springer Verlag, 2014.
3. Odsuren M., Katō K., Khuukhenkhoo G., Davaa S., “Scattering cross section for various potential systems”. *Nuclear Engineering and Technology* Vol. 49, no.5 (2017): P.1006.
4. Odsuren M., Katō K., Khuukhenkhoo G. “Scattering phase shifts in the complex scaling method”. *Journal Experimental and Theoretical Physics letters* Vol.102, no. 7 (2015): P.409.
5. Kruppa A.T., Katō K. “Resonances in Complex-Scaled Orthogonality Condition Model of Nuclear Cluster System”. *Progress Theoretical Physics* Vol.84 (1990): P.1145.
6. Odsuren M., Khuukhenkhoo G., Kato K. “Structure of Continuum States of A= 5 Mirror Nuclei in the Complex Scaling Method”. *Acta Physica Polonica B* Vol.50, no.3 (2019): P.549.
7. Odsuren M., Khuukhenkhoo G., Sarsembayeva A.T., Amangeldi N., Katō K. “Analysis of continuum level density for virtual and resonance states”. *Indian Journal of Physics* Vol.96, no.2 (2022): P.543.
8. Ho Y.K. “The method of complex coordinate rotation and its applications to atomic collision processes”. *Phys. Rep.* Vol.99 (1983): P.1.
9. Aoyama S., Myo T., Katō K., Ikeda K. “The Complex Scaling Method for Many-Body Resonances and Its Applications to Three-Body Resonances”. *Prog. Theor. Phys.* Vol.116 (2006): P.1.
10. Young F. C, and Knudson A. R. “Reaction on ${}^9\text{Be}$ as a Direct Reaction”. *Nuclear Physics A*. Vol.184 (1972): P.563.

© This is an open access article under the (CC)BY-NC license (<https://creativecommons.org/licenses/by-nc/4.0/>). Funded by Al-Farabi KazNU.

Hayam F. Darweesh* , Essam M. Abulwafa , Atalla M. El-Hanbaly 

Mansoura University, Mansoura, Egypt

*e-mail: hayamfawzi1990@yahoo.com

(Received 17 January 2022; received in revised form 31 May 2022; accepted 6 June 2022)

Arbitrary amplitude nonlinear waves in a four-component quantum plasma

Abstract: Based on the approach of arbitrary amplitude Sagdeev pseudo-potential, the fully nonlinear structures, such as soliton and double-layer waves, of a four-component quantum plasma system have been extensively investigated. The plasma system under consideration consists of inertial positive and negative dust species and inertialess quantum ions and electrons. For simplicity, the dust grains are considered to have a constant surface charge. For typical plasma parameters, like Mach number, temperatures ratio, densities ratios and quantum parameter, the bifurcation analysis enables us to distinguish three types of nonlinear waves, namely compressive soliton, rarefactive soliton and double layer depending on the magnitude of the configurational plasma parameters. The formations and the existence ranges of both solitons and double layers are studied and found to be highly sensitive to the values of the chosen plasma parameters and the quantum indices as well. The implications of the obtained results have a wide relevance in the study of space and laboratory quantum dusty plasmas where the positive and negative dust particulates are presented, and quantum effects are taken into account.

Key words: Four-component quantum dusty plasma; Sagdeev pseudo-potential; Solitary waves and double-layers

Introduction

The topic of propagating linear and nonlinear waves in quantum dusty plasma had a great deal of interest due to its wide application in quantum plasma media such as in high-intensity laser-produced plasmas, dense astrophysical objects and ultra-small electronic devices [1-5]. It is well known that dusty plasma is the most general form of plasmas in most of space and astrophysical bodies which comprising with electrons, positive ions, neutral molecules and massive micrometer-sized charged dust grains. In addition to plasma laboratory, dusty plasmas are also observed in pulsar magnetospheres, active galactic nuclei, planetary rings, solar atmosphere, interstellar medium, comet tails and noctilucent clouds [6-14]. Dusty plasma may have dust grains with negative charge, dust grains with positive charge or may have both types of dust grains depending on the charging processes [15-17]. Due to the presence of large number of charged particles in dusty plasma media, many reports indicate that there are two sorts of low-frequency waves in dusty plasmas, called dust

acoustic (DA) waves and dust-ion acoustic (DIA) waves [18, 19]. Consequently, investigation of nonlinear wave characteristics in such media has been studied by many researchers [18, 20, 21]. Mannan and Mamun [18] studied the DA solitary waves associated with general and realistic self-gravitating dusty plasma medium composed of positive and negative charged warm dust grains as well as non-thermal ions. The population effect of non-thermal ions is examined and found that it modifies the basic properties of the obtained DA solitary waves. Khaled et al. [20] studied the presence of DA solitary waves in a dusty plasma medium with opposite polarity of dust grains and Maxwellian distributed electrons and ions taking into account the polarization force effect. They observed that the propagation characteristics of the obtained DA solitary waves are significantly modified due to the polarization force effect. In Farooq et al. [21] work, they investigated the polarization force effect on the nonlinear properties of DA solitary waves in a four component dusty plasma composed of positive and negative dust grains, non-Maxwellian electrons follows hybrid

Cairns–Tsallis distribution and Maxwellian ions. As a result of the presence of non-Maxwellian electrons, it is found that the polarization force acting on negatively charged dust is different from that acting on positively charged dust.

In quantum plasma media, the plasma behaves like degenerate plasma when its components are at higher densities and low temperature as well as the thermal de Broglie wavelength of charged species becomes same or larger than the inter-particle distance [22-24]. Quantum effects of plasma species are found to play an important role in many plasma physics applications such as in ultra-cold plasmas, ultra-small electronic devices, nanostructure devices, semiconductors, laser produced plasmas as well as in astrophysical plasmas such as interiors of white dwarfs and neutron stars [25-30]. In quantum plasma, the classical hydrodynamic equations are no longer suitably at all and should be modified [31], where the Bohm potential term may be added in the momentum equation. This of course makes the procedure of finding an explicit form for the pseudo-potential function very difficult. This leads some authors [32, 33] to restrict their studies only on small amplitude nonlinear wave's approximations, accordingly. The presence of different types of nonlinear waves such as solitary waves, shock structure and double layers in quantum dusty plasma had been investigated by many researchers in the framework of KdV-type equations. For instance, El-Hanbaly et al. [32] investigated the propagation characteristics of DA solitary waves interaction in four-component quantum dusty plasma and the quantum effects of plasma species are discussed. They found that the quantum parameters of electrons and ions played an important role on the features of the DA solitary waves such as phase shifts in trajectories due to collision. Nonlinear properties of DA solitary waves considering dust polarity effects as well as electrons and ions quantum effects in magnetized quantum dusty plasma were analyzed by Gao [33]. By performing numerical analysis, he found that the nature of solitary waves was modified depending on the effects of quantum electrons and ions. However, most of these studies have only focused on the use of reductive perturbation technique.

In order to investigate the fully nonlinear structures in quantum plasma, Sagdeev pseudo-potential technique and bifurcation analysis have been widely used [34, 35]. For example, Abulwafa et al. [34] have used the Sagdeev pseudo-potential

technique and bifurcation analysis to study the properties of DA double-layers in four-component dusty plasma with q-non-extensive distributed electrons and ions. They investigated that the behavior of the double-layers solution is extremely sensitive to the non-extensive parameters of electrons and ions as well as the Mach number strength. El-Monier and Atteya [35] used the bifurcation analysis to investigate the DA wave propagation in four-component dusty plasma. Abulwafa et al. [36] investigated the formation and propagation of small amplitude nonlinear waves in a four-component quantum dusty plasma. Therefore, we plan to extend the previous our study by investigating the fully nonlinear arbitrary amplitude waves in quantum dusty plasma by employing the Sagdeev pseudo-potential technique and bifurcation analysis. The effect of physical parameters such as Mach number M , dust charge-mass ratio R , temperature ratio σ , electron density ratio μ_e , ion density ratio μ_i and electron quantum parameter H_e are studied and found that they play vital role on the formation of both compressive and rarefactive solitary waves and on the creation of compressive double layers.

The quantum dusty plasma basic equations are presented in Sect. 2. Sagdeev Pseudo-potential and phase portrait analysis are derived in Sect. 3. Nonlinear analysis are explained and discussed in Sect. 4 while in Sect. 5, the conclusion is provided.

Basic Equations

Quantum dusty plasma system has four components comprising of inertial positive and negative dust species and inertialess quantum ions and electrons is considered. Such dusty plasma medium can be existed in many astrophysical situations such as Jupiter's magnetosphere, upper and lower mesosphere and comet tails [37-41]. For simplicity, the dust grains are considered to have a constant surface charge. The normalized basic equations of the considered system are described as follows:

The dynamic equations for quantum electrons and ions are described by

$$\frac{\partial \phi}{\partial x} - \sigma_j n_j \frac{\partial n_j}{\partial x} + \frac{\delta_j}{2} H_j^2 \frac{\partial}{\partial x} \left(\frac{1}{\sqrt{n_j}} \frac{\partial^2}{\partial x^2} \sqrt{n_j} \right) = 0, \quad (1)$$

where $j = e$ and i refer to electrons and ions, respectively. n_j represents the density number, $H_j = (\hbar\omega_{pd} / C_d^2) \sqrt{Z_- / (m_j m_-)}$ is the quantum factor that is defined as the ratio of the quantum energy to the thermal energy of the particle, $C_d = (k_B T_{Fi} Z_- / m_-)^{1/2}$ is the DA speed, $\omega_{pd} = [4\pi n_0 (Z_-)^2 e^2 / m_-]^{1/2}$ is the dust plasma frequency and the temperature ratios are $\sigma_e = \sigma = T_{Fe} / T_{Fi}$, $\sigma_i = -1$ and $\delta_e = 1$, $\delta_i = -1$.

Both continuity and momentum equations for the two dust species are given by

$$\frac{\partial n_k}{\partial t} + \frac{\partial (n_k u_k)}{\partial x} = 0, \quad (2a)$$

$$\frac{\partial u_k}{\partial t} + u_k \frac{\partial u_k}{\partial x} + R_k \frac{\partial \phi}{\partial x} = 0, \quad (2b)$$

where $k = +$ and $-$ refer to positive dust and negative dust, respectively, n_k is the particle density number, u_k is the particle fluid velocity and the dust charge-mass ratios are $R_+ = R = \alpha / \beta$ where $\alpha = Z_+ / Z_-$ and $\beta = m_+ / m_-$ while $R_- = -1$.

Finally, the Poisson's equation of the given quantum dusty plasma system can be written as

$$\partial^2 \phi / \partial x^2 - n_- + \mu_+ n_+ - \mu_e n_e + \mu_i n_i = 0. \quad (3)$$

The following normalizations $x \rightarrow x / \lambda_{Dd}$, $t \rightarrow t \omega_{pd}$, $n_{j(k)} \rightarrow n_{j(k)} / n_{0j(k)}$, $u_k \rightarrow u_k / C_d$,

$\phi \rightarrow e\phi / (2k_B T_{Fi})$ have been applied into (1)-(3). In the above equations, ϕ is the electrostatic potential, $n_{0j(k)}$ refers to the unperturbed plasma species density number. Here, $\lambda_{Dd} = [2k_B T_{Fi} / (4\pi n_0 Z_- e^2)]^{1/2}$ is the dust Debye length and the species density ratio is $\mu_j = Z_j n_{0j} / (Z_- n_{0-})$. In addition, k_B , T_{Fj} , Z_k , $m_{j(k)}$ and e refer to the Boltzmann constant, the species type Fermi temperature, the number of electronic charge residing on the surface of the dust particle, the particle mass and electronic charge, respectively.

The quantum effects due to dust grains are ignored in the considered model as they have large inertia in comparison with both electrons and ions. In addition, the two quantum factors H_e and H_i are governed by the relation $H_e / H_i = \sqrt{m_i / m_e}$.

Sagdeev Pseudo-potential Analysis

To investigate the existence and propagation of the arbitrary amplitude localized electrostatic waves in the plasma system under consideration, we consider moving coordinate ansatz

$$\zeta = x - Mt, \quad (4)$$

that moves parallel to the mentioned waves with Mach number M .

Inserting the travelling wave transformation (4) in the system of equations (1) and (2), one gets a system of nonlinear coupled ordinary differential equations, viz.

$$\frac{d\phi(\zeta)}{d\zeta} - \sigma_j n_j(\zeta) \frac{dn_j(\zeta)}{d\zeta} + \frac{\delta_j}{2} H_j^2 \frac{d}{d\zeta} \left[\frac{1}{\sqrt{n_j(\zeta)}} \frac{d^2}{d\zeta^2} \sqrt{n_j(\zeta)} \right] = 0, \quad (5)$$

$$-M \frac{dn_k(\zeta)}{d\zeta} + \frac{d[n_k(\zeta)u_k(\zeta)]}{d\zeta} = 0, \quad (6a)$$

$$-M \frac{du_k(\zeta)}{d\zeta} + u_k(\zeta) \frac{du_k(\zeta)}{d\zeta} + R_k \frac{d\phi(\zeta)}{d\zeta} = 0, \quad (6b)$$

while the Poisson's equation can be rewritten as

$$d^2\phi(\zeta)/d\zeta^2 = n_-(\zeta) - \mu_+n_+(\zeta) + \mu_en_e(\zeta) - \mu_in_i(\zeta). \tag{7}$$

where all physical quantities in (5) and (6) become only functions of a single variable ζ .

With appropriate boundary conditions, viz. $n \rightarrow 1$, $dn/d\zeta \rightarrow 0$, $u \rightarrow 1$ and $\phi \rightarrow 0$ as $\zeta \rightarrow \pm\infty$, the forms of density functions n_j of electrons and ions and n_k of dust particles in terms of electrostatic potential ϕ can be explicitly obtained after integrating (5) and (6) as

$$n_j(\zeta) = \sqrt{[1 + 2\phi(\zeta)/\sigma_j] + \delta_j(H_j^2/\sigma_j)[1 + 2\phi(\zeta)/\sigma_j]^{-1/4} d^2[1 + 2\phi(\zeta)/\sigma_j]^{1/4}/d\zeta^2}, \tag{8}$$

$$n_k(\zeta) = M/\sqrt{M^2 - 2R_k\phi}. \tag{9}$$

By looking upon (8), one may see that the density function of both electrons and ions $n_j(\zeta)$ depend obviously on the corresponding quantum factors H_j , whereas (9) shows that the dependence of dust densities $n_k(\zeta)$ on H_j is not exist. In addition, in order to guaranty the plasma state variables $n_k(\zeta)$ are analytical functions (i. e; real) we have to recall the well-known classical inequality, $\phi \leq \phi_{\max} = M^2/(2R_k)$ where ϕ_{\max} refers to the maximum value of ϕ (the amplitude of nonlinear

waves in the plasma). However, it provides us a useful check for high amplitude limits in terms of the dust charge-mass ratio R and Mach number M . Inserting the forms of $n_j(\zeta)$ and $n_k(\zeta)$, (8) and (9), into the reduced Poisson's equation (7), one obtains

$$d^2\phi/d\zeta^2 = -\rho(\phi), \tag{10}$$

where the charge density $\rho(\phi)$ is represented by

$$\begin{aligned} \rho(\phi) = & -M/\sqrt{M^2 + 2\phi} + \mu_+M/\sqrt{M^2 - 2R\phi} \\ & - \mu_e\sqrt{(1 + 2\phi/\sigma) + (H_e^2/\sigma)(1 + 2\phi/\sigma)^{-1/4} d^2(1 + 2\phi/\sigma)^{1/4}/d\zeta^2} \\ & + \mu_i\sqrt{(1 - 2\phi) + H_i^2(1 - 2\phi)^{-1/4} d^2(1 - 2\phi)^{1/4}/d\zeta^2}, \end{aligned} \tag{11}$$

Now, the advantage of using Sagdeev pseudo-potential technique is that the four-component quantum system equations are reduced to a single equation (10). This implies that studying the fully nonlinear structures of the plasma system is equivalent to study the solution of (10).

Multiplying (10) by $d\phi/d\zeta$ and integrating once, the order of (10) is reduced by one and can be written in the form of an energy balance integral equation

$$(d\phi/d\zeta)^2/2 + V(\phi) = E, \tag{12}$$

where

$$V(\phi) = -\int^\phi d\phi'\rho(\phi'), \tag{13}$$

and E is the integration constant. The first term of (12) refers to the kinetic energy whereas $V(\phi)$ is known as Sagdeev pseudo-potential energy function. This procedure is called Sagdeev pseudo-potential formalism. Using appropriate boundary conditions $\phi = d\phi/d\zeta = d^2\phi/d\zeta^2 \rightarrow 0$, at $\zeta \rightarrow \pm\infty$, the right side of (12) goes to zero.

Having integrated (13), $\phi = +\int^\phi d\phi'\sqrt{-V(\phi')}$,

the existence and propagation of the fully nonlinear structures in our plasma system can be identified exactly.

It is noted that knowing the explicit form of the Sagdeev potential $V(\phi)$ enables us to obtain the

maximum and minimum values of the Mach number (M_{max} , M_{min}) at which the permitted nonlinear waves exist. The maximum value of Mach number M_{max} can be defined, in terms of plasma parameters, by solving the algebraic equation $V(\phi_{max})=0$ for M where $\phi_{max} = M^2/(2R_k)$, the maximum values of the electrostatic potential ϕ for compressive and rarefactive waves. But on the other side, the minimum value of the Mach number M_{min} can be determined by solving the inequality $d^2V/d\phi^2 < 0$

at $\phi=0$. The interval of Mach number ($M_{min} - M_{max}$) leads us to identify the existence range at which the formula of nonlinear waves exists and propagates in the plasma model. It is anticipated from the above analysis that the existence and propagation of the nonlinear waves in the plasma system requires the values of Mach number M included in $M_{min} < M < M_{max}$, otherwise, the existence of nonlinear waves is not possible.

With the knowledge of the explicit form of Sagdeev potential function $V(\phi)$, the existence conditions for the localized nonlinear waves are readily examined. However, the conditions for solitary waves to exist are:

(i) $V(\phi) = dV/d\phi = 0$ at $\phi = 0$, which implies that the associated electric field ($E(\phi) = -d\phi/d\zeta$) and the charge density $\rho(\phi)$ equal zero at the origin ($\phi = 0$). Also, at the origin the potential condition $d^2V/d\phi^2 < 0$ should be satisfied, implying that the curve has maximum at (0,0) and hence the origin can be viewed as fixed unstable point.

(ii) The final condition $V(\phi) < 0$, is necessary for obtaining the configurational plasma parameters for which this condition holds. This means that the electrostatic potential ϕ follow the interval $0 < \phi < \phi_{max}$ for compressive waves or $\phi_{max} < \phi < 0$ for rarefactive solitary waves. Here, ϕ_{max} denotes the first non-zero root of $V(\phi) = 0$.

On the other side, the existence of the double-layer requires the following two conditions:

(i) $V(\phi) = dV/d\phi = 0$ at $\phi = 0$, and $\phi = \phi_{max}$.

(ii) $d^2V/d\phi^2 < 0$ at $\phi = 0$, and $\phi = \phi_{max}$.

Therefore, we are interested to specify the fully nonlinear structures propagating in the plasma system. The crucial point of this methodology is that the form of the Sagdeev potential function should be

known explicitly by integrating (13). Since the integration procedure is very difficult task, it is convenient to deal with such equation numerically. Then, we recall the bifurcation analysis to investigate the behavior and properties of the fully nonlinear structures graphically. In addition, the impact of some relevant plasma parameters on the nonlinear waves can be also examined.

Nonlinear Analysis

First, we shall investigate the influence of the physical plasma parameters such as (Mach number M , dust charge-mass ratio R , temperature ratio σ , electron density ratio μ_e , ion density ratio μ_i and electron quantum parameter H_e) on the profile of the nonlinear structures. The obtained results can be summarized in Figures (1) – (5), where the physical plasma parameters follow $n_{e0} \approx 2 \times 10^{30} m^{-3}$, $T_{Fe} \approx 1.0 \times 10^2 K$, $n_{i0} \approx 1 \times 10^{30} m^{-3}$, $T_{Fi} \approx 1/6 \times 10^2 K$, $n_{-0} \approx 5 \times 10^{26} m^{-3}$, $Z_- \approx 10^3$, $m_- \approx 10^{-17} kg$, $n_{+0} \approx 1.5 \times 10^{27} m^{-3}$, $Z_+ \approx 10^3$, $m_+ \approx 10^{-17} kg$ [2, 42, 43].

In Figs (1), the Sagdeev potential function $V(\phi)$, phase portrait $(\phi, d\phi/d\zeta)$, electrostatic potential $\phi(\zeta)$ and associated electric field $E(\zeta)$ are shown graphically for different values of the Mach number M . The chosen values of the Mach number M are taken in our calculations according to the allowed interval ($M_{min} - M_{max}$), where the other physical parameters are $R=1.0$, $\sigma=6.0$, $\mu_e=4.0$, $\mu_i=2.0$, $H_e=0.3$. Note that the width of the Sagdeev potential well means the amplitude of the solitary wave and its depth refers to the slop of the solitary pulse. In Fig (1a), it is seen that the dash-dotted potential curve ($M = 1.255$) and dashed curve ($M = 1.265$) refer to the coexistence of both compressive and rarefactive localized pulses. Obviously, increasing the Mach number, the potential well gets wider and deeper. This means that faster electrostatic pulse gets taller and narrower as the Mach number increases. Also, it can be seen that the amplitude and width of the rarefactive solitary waves are clearly greater than those of the compressive waves. The corresponding trajectories in the phase portrait diagram $(\phi, d\phi/d\zeta)$, Fig (1b), have obviously two stable centers at $(\phi_1, 0)$ and

$(\phi_2, 0)$ beside one unstable saddle point at $(0, 0)$, where ϕ_1 and ϕ_2 are the values of the electrostatic potential ϕ at which the Sagdeev potential $V(\phi)$ is minimum. The trajectories enclosing the two centers points and passing through the saddle point is called homoclinic orbits, which refer to stable solitary waves. The profiles and properties of the solitary waves $\phi(\zeta)$ and the associated electric field $E(\zeta)$ are shown graphically in Figs (1c) and (1d). Now, it is concluded that our plasma system supports the formation of both compressive and rarefactive to coexist in this plasma configuration. Moving to higher value of the Mach number, the dashed line curve in the potential diagram, Fig (1a), shows another feature of the nonlinear waves. The dotted curve at $M = 1.27278825$ denotes to the coexistence of both compressive double-layer and rarefactive nonlinear solitary wave. The existence of double-layer can be seen as a sudden change of the electrostatic potential pulse $\phi(\zeta)$ due to the presence of space charge. The corresponding trajectory in the phase-portrait, Fig (1b), has two unstable saddle points at $(0, 0)$ and $(\phi_{\max}, 0)$ beside a stable center point at $(\phi_1, 0)$. The trajectory passing through two unstable saddle points is called heteroclinic orbit and refers to double layer. On the other side of $\phi(\phi < 0)$, there exist one stable center point at $(\phi_2, 0)$ and one unstable saddle point at $(0, 0)$. The orbit going from saddle point confirms the existence of rarefactive nonlinear waves. The behavior of the electrostatic potential $\phi(\zeta)$ and the associated electric field $E(\zeta)$ (dotted line curve) can be graphically shown as in Figs (1c) and (1d). Further increasing the Mach number, the solid curve at $M = 1.28$ shows that the positive amplitude nonlinear wave is no longer exist and we are only left with the rarefactive solitary wave in this plasma configuration.

In addition to the Mach number M , the effect of dust charge-mass ratio R on the formation and existence range of nonlinear waves can be also shown by introducing the bifurcation diagrams, Figs (2). In Figs (2a) and (2b), the dashed-dot curve at $R = 1.03$ and the dashed curve at $R = 1.0$ reveal that the coexistence of both compressive and rarefactive

solitary waves can be observed. On the other side, when $R = 0.96159$ (dotted curve) another feature of special interest arises, where compressive double-layer and rarefactive solitary wave coexist. Decreasing further slightly the value of R ($R = 0.95$), only rarefactive solitary waves may be observed. The bifurcation curves also illustrate that the amplitude of the rarefactive solitary waves is greater than those of compressive solitary waves. From above, one may conclude that the dust charge-mass ratio R plays a significant role in formation of different types of nonlinear waves in this plasma system. The profiles of the different types of electrostatic solitary waves and the associated electric field are graphically shown in Figs (2c) and (2d), where the amplitude (width) decreases (increases) as R increases. This implies that the dust charge-mass ratio R would shrink the formation of nonlinear solitary waves.

Furthermore, in the same manner the effects of other configurational plasma parameters can be also achieved. However, the temperature ratio σ and the electron density ratio μ_e have the same behavior as that of the dust charge-mass ratio R , where the amplitude (width) of the nonlinear solitary waves decreases (increases) as σ and μ_e increases as shown in Figs (3) and (4), respectively. In the contrary, the effect of the ion density ratio μ_i has an opposite property, where the amplitude (width) of the nonlinear waves increases (decreases) with an increasing in μ_i . This means that the nonlinear electrostatic solitary waves and the strength of the associated bipolar electric field get stronger by increasing μ_i , as shown clearly in Fig (5).

Finally, in order to see the impact of quantum index H_e , the bifurcation analysis is graphically plotted, Figs (6), for different values of H_e ($H_e = 0.0, 1.0, 2.0, 3.0$) where the other chosen parameters are $M = 1.25$, $R = 1.0$, $\sigma = 6.0$, $\mu_e = 4.0$, $\mu_i = 2.0$. Obviously, this analysis supports the coexistence of both compressive and rarefactive solitary waves, where the amplitudes are nearly the same while the depth of the soliton decreases as H_e increases, as evidently in Figs (6). In addition, the strength of the associated electric field increases slightly as H_e increases.

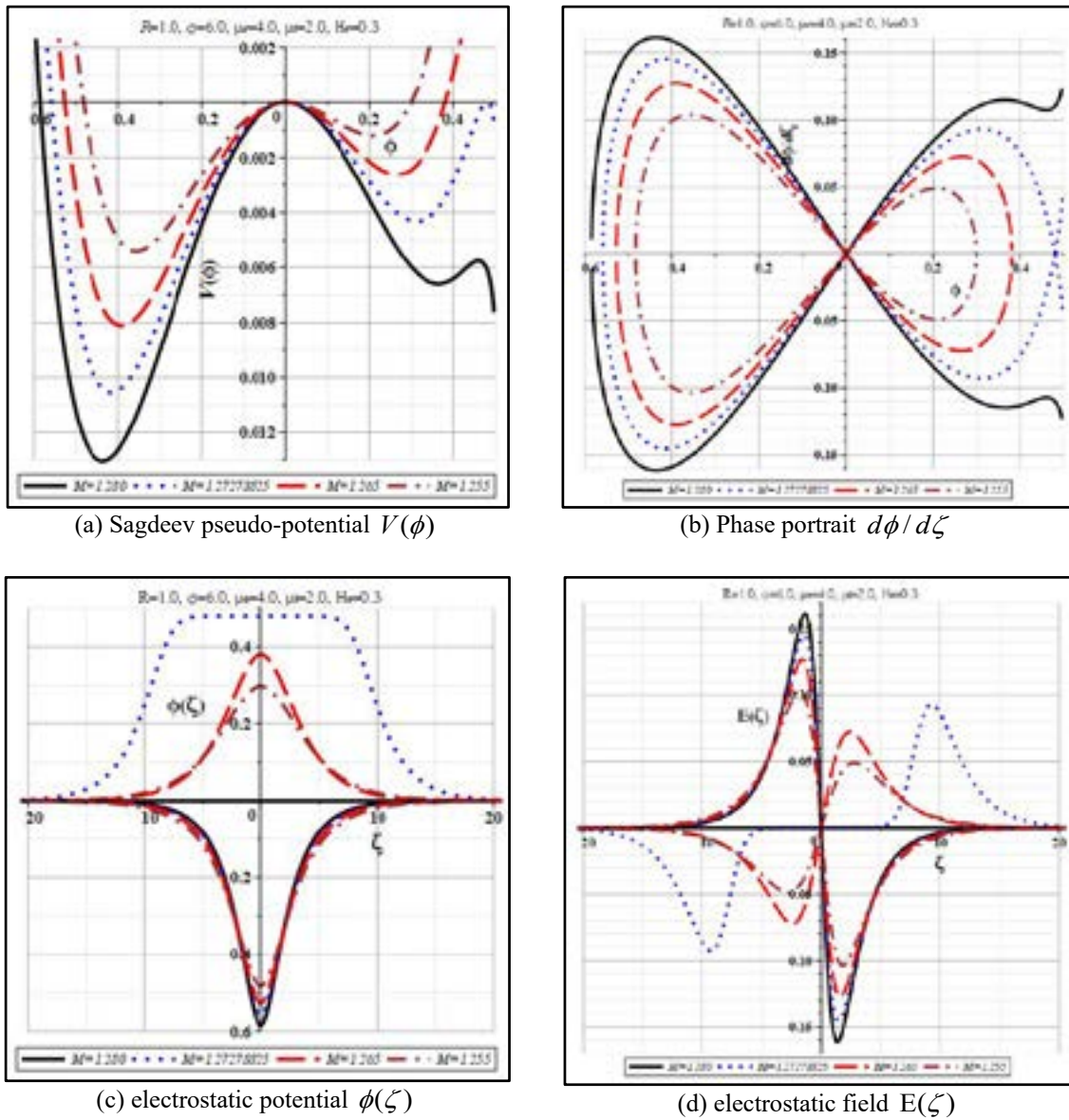
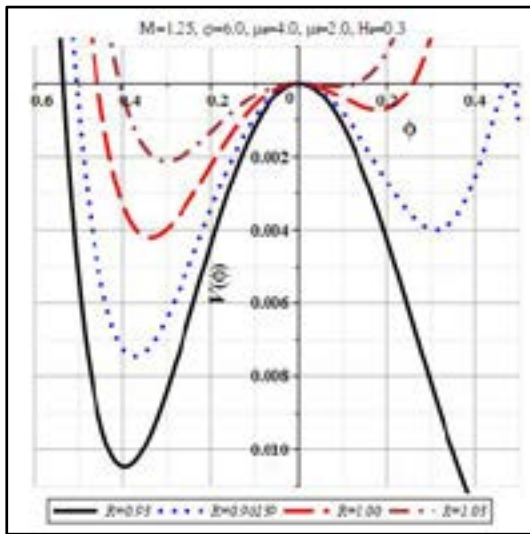
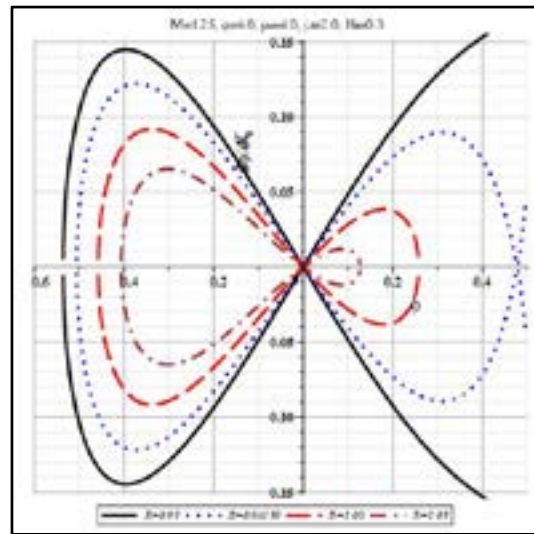


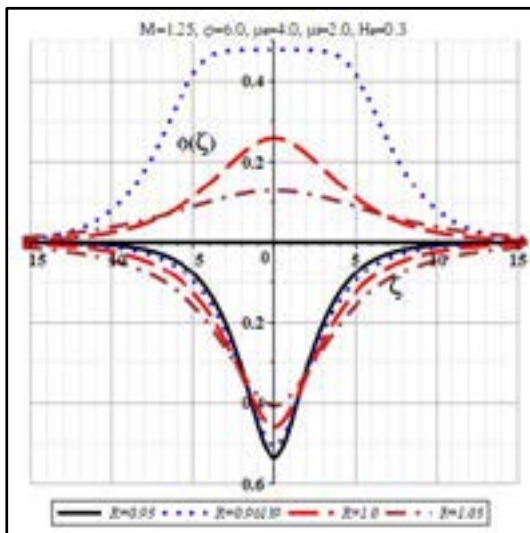
Figure 1 – Nonlinear structure functions at different values of M for $R = 1.0$, $\sigma = 6.0$, $\mu_e = 4.0$, $\mu_i = 2.0$, $H_e = 0.3$



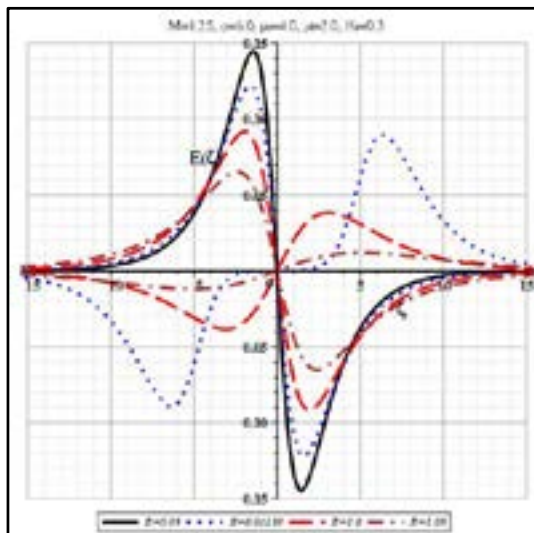
(a) Sagdeev pseudo-potential $V(\phi)$



(b) Phase portrait $d\phi/d\zeta$



(c) electrostatic potential $\phi(\zeta)$



(d) electrostatic field $E(\zeta)$

Figure 2 – Nonlinear structure functions at different values of R for $M = 1.25$, $\sigma = 6.0$, $\mu_e = 4.0$, $\mu_i = 2.0$, $H_e = 0.3$

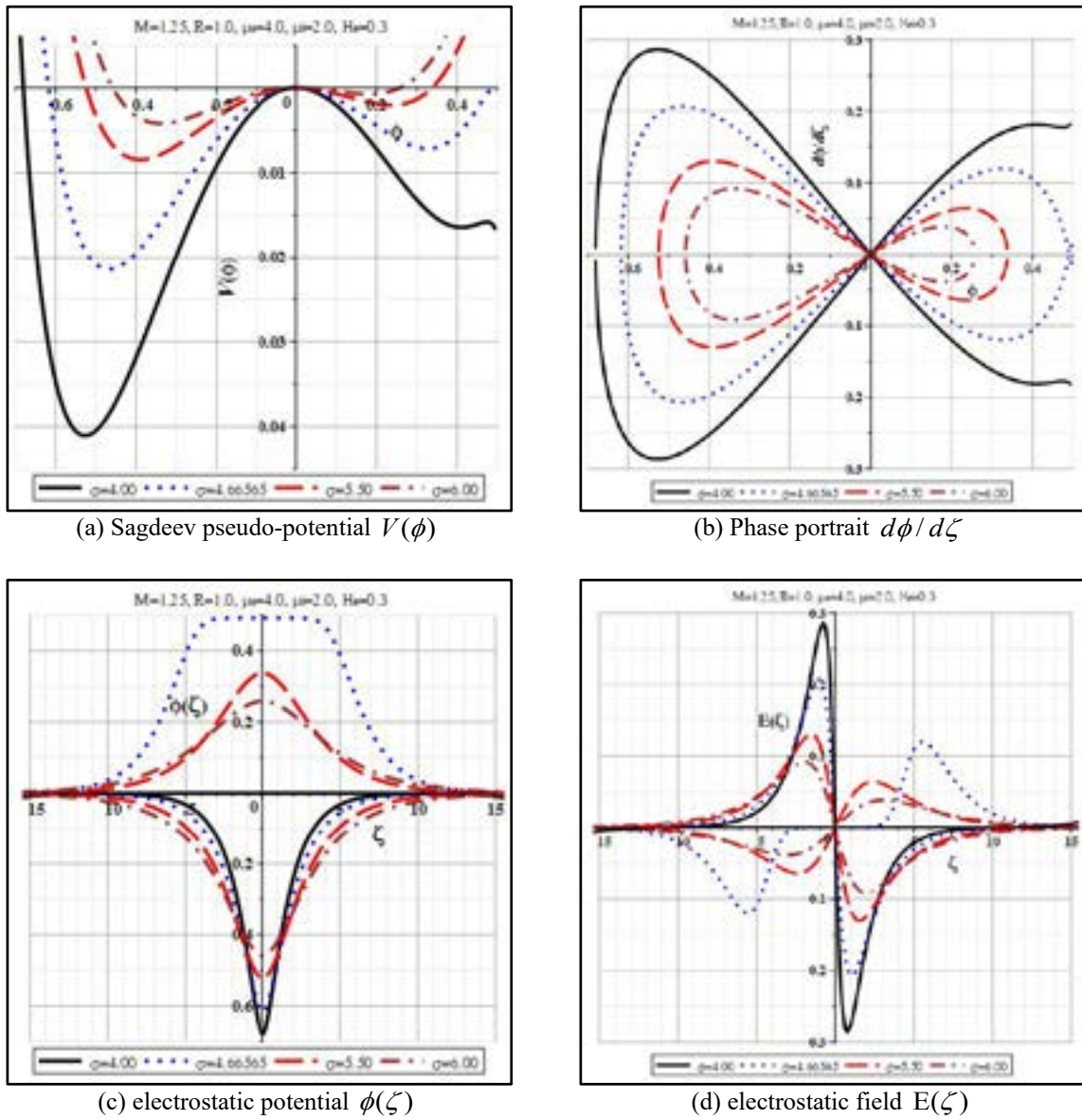


Figure 3 – Nonlinear structure functions at different values of σ for $M = 1.25, R = 1.0, \mu_e = 4.0, \mu_i = 2.0, H_e = 0.3$

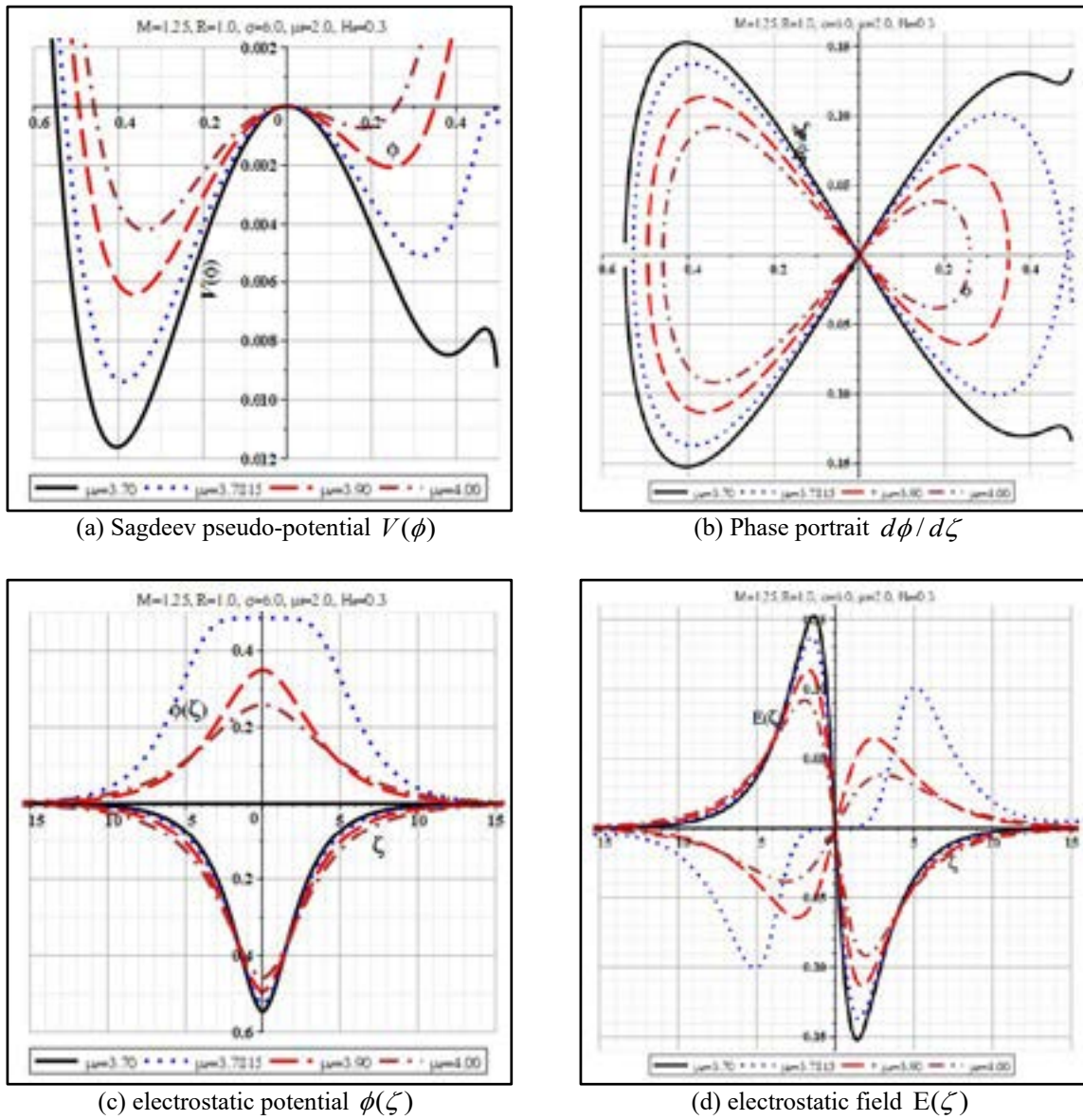


Figure 4 – Nonlinear structure functions at different values of μ_e for $M = 1.25$, $R = 1.0$, $\sigma = 6.0$, $\mu_i = 2.0$, $H_e = 0.3$

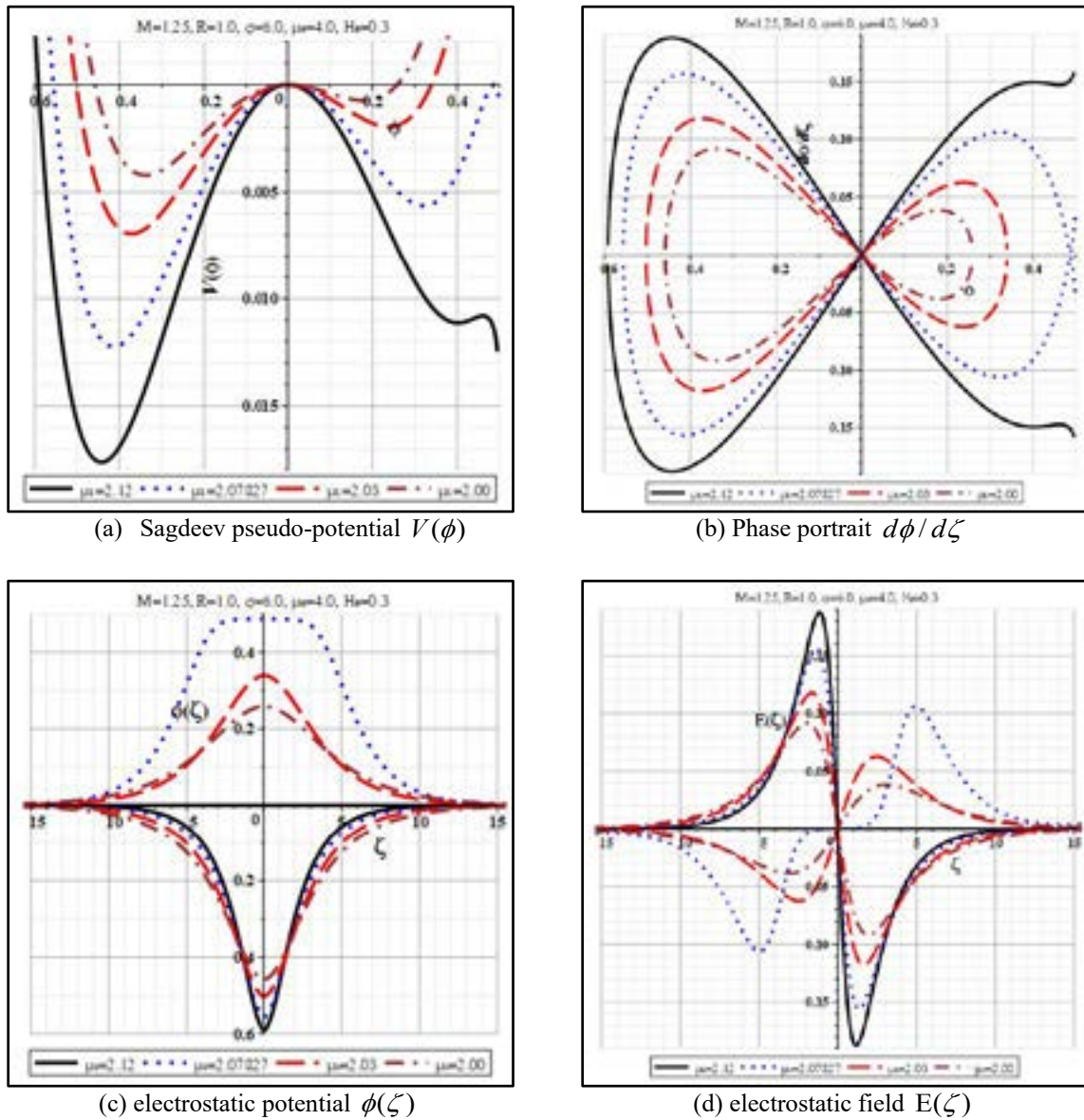
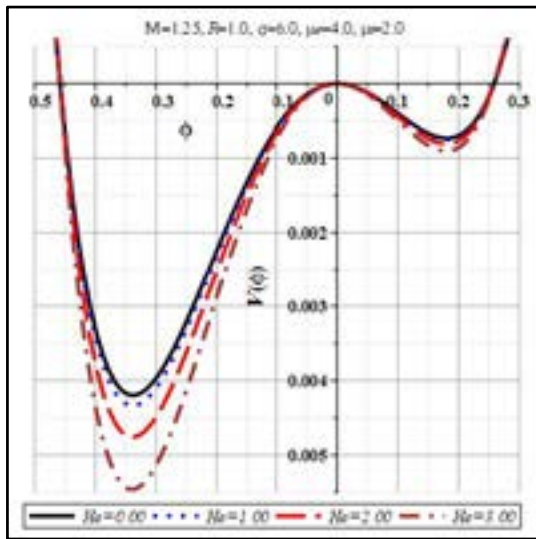
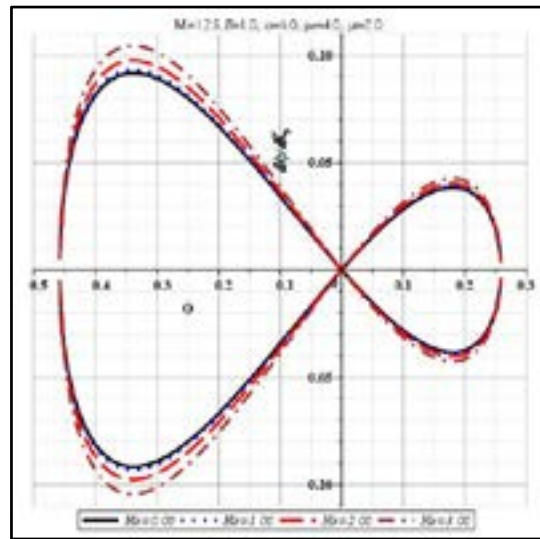


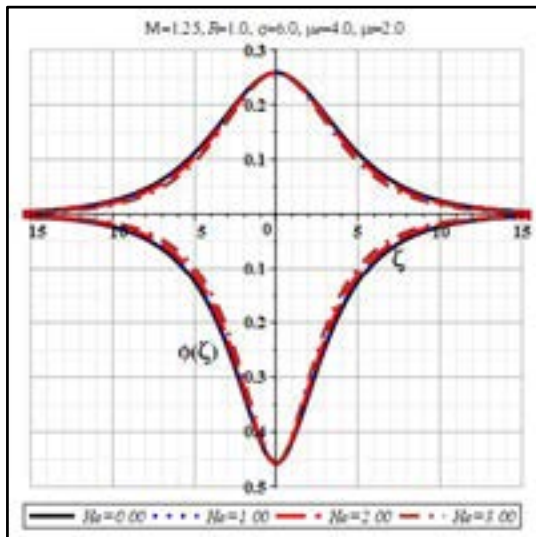
Figure 5 – Nonlinear structure functions at different values of μ_i for $M = 1.25$, $R = 1.0$, $\sigma = 6.0$, $\mu_e = 4.0$, $H_e = 0.3$



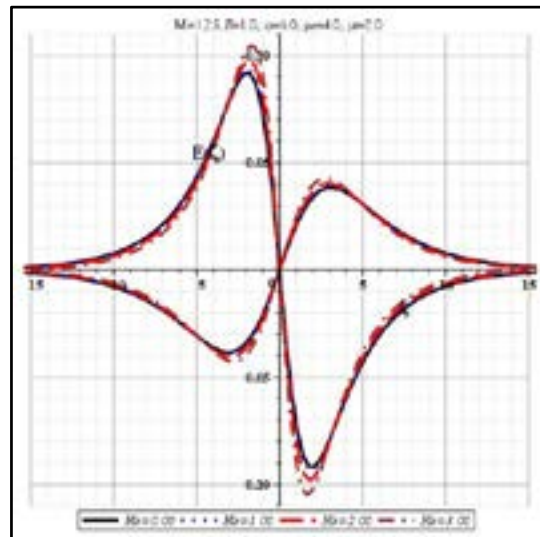
(a) Sagdeev pseudo-potential $V(\phi)$



(b) Phase portrait $d\phi/d\zeta$



(c) electrostatic potential $\phi(\zeta)$



(d) electrostatic field $E(\zeta)$

Figure 6 – Nonlinear structure functions at different values of H_e for $M = 1.25$, $R = 1.0$, $\sigma = 6.0$, $\mu_e = 4.0$, $\mu_i = 2.0$

Conclusions

In this work, we have considered a four-component quantum dusty plasma consisting of positive and negative dust particulates, electrons and ions that are assumed to be quantum mechanical. In order to examine the fully arbitrary nonlinear waves in such plasma model, Sagdeev pseudo-potential method has been first employed. The inclusion of the quantum effect makes the mathematical manipulations difficult task. Therefore, we recall the bifurcation analysis to achieve this task graphically rather than analytically. Based on bifurcation analysis, one may be able to distinguish three types of nonlinear arbitrary amplitude waves, namely compressive solitons, rarefactive solitons and double-layers depending on the magnitude of the configurational plasma parameters. The effects of some relevant plasma parameters on the profile of electrostatic potential $\phi(\zeta)$ and the associated bipolar electric field $E(\zeta)$ have been extensively studied. The nonlinear arbitrary solitary waves get stronger as the Mach number M and ion density ratio μ_i increase, while the dust charge-mass ratio R , temperature ratio σ and electron density ratio μ_e have opposite properties. Additionally, the analysis reveal that, in a certain plasma configuration, the coexistence of both compressive and rarefactive solitary waves occurs, while double-layer and rarefactive soliton are found to coexist also. The existence of double-layer provides us the existence range of compressive waves, for example Mach number M value of double-layer can be viewed as the maximum range of compressive solitons. In other plasma configuration, the analysis shows that the double-layer is no longer exist and we have left only with arbitrary amplitude rarefactive solitary waves. It is also found that the quantum index H_e influence the width of electrostatic potential profile only, while the amplitude remains nearly the same.

The present results of this work are applicable to investigate the dynamical characteristics of nonlinear waves in quantum space dusty plasmas.

Acknowledgements

This paper is dedicated to the spirit of Late Prof. S. A. El-Wakil, the sol-father of Mansoura University Theoretical Physics Group.

References

1. Misra A P, Samanta S. "Double-layer shocks in a magnetized quantum plasma". *Physical Review* 82, (2010): 037401 (DOI: 10.1103/PhysRevE.82.037401)
2. Moslem W M, Shukla P K, Ali S, Schlickeiser R. "Quantum dust-acoustic double layers". *Physics of Plasmas* 14(4) (2007): 042107 (DOI: 10.1063/1.2719633)
3. Sahu B, Sinha A, Roychoudhury R. "Electron acoustic waves in a 2-electron, dissipative, quantum magneto plasma". *European Physical J. Plus* 133(9) (2018): 360 (DOI: 10.1140/epjp/i2018-12167-x)
4. Hossen M R, Mamun A A. "Study of Nonlinear Waves in Astrophysical Quantum Plasmas". *Brazilian J Physics* 45(1) (2015): 200-205 (DOI: 10.1007/s13538-014-0297-4)
5. Pradhan B, Abdikian A, Saha A. "Characteristics of supernonlinear and coexistence features for electron-acoustic waves in an adiabatic quantum plasma". *European Physical J D* 75(2) (2021): 48 (1-11) (DOI: 10.1140/epjd/s10053-021-00045-3)
6. Thomas H M, Morfill G E, Fortov V E, Ivlev A V, Molotkov V I, Lipaev A M, Hagl T, Rothermel H, Khrapak S A, Suetterlin R K, Rubin-Zuzic M, Petrov O F, Tokarev V I, Krikalev S K. "Complex plasma laboratory PK-3 Plus on the International Space Station". *New J. Physics* 10 (2008): 33036 (DOI: 10.1088/1367-2630/10/3/033036)
7. Fortov V E, Morfill G E. *Complex and Dusty Plasmas: From Laboratory to Space*. Florida: CRC Press, 2009.
8. Pustynnik M Y, Fink M A, Nosenko V, Antonova T, Hagl T, Thomas H M, Zobnin A V, Lipaev A M, Usachev A D, Molotkov V I, Petrov O F, Fortov V E, Rau C, Deysenroth C, Albrecht S, Kretschmer M, Thoma M H, Morfill G E, Seurig R, Stettner A, Alyamovskaya V A, Orr A, Kufner E, Lavrenko E G, Padalka G I, Serova E O, Samokutyayev A M, Christoforetti S. "Plasmakristall-4: New complex (dusty) plasma laboratory on board the International Space Station". *Review of Scientific Instruments* 87 (2016): 093505 (DOI: 10.1063/1.4962696)
9. Gurevich A V, Istomin Y. *Physics of the pulsar magnetosphere*. Cambridge: Cambridge University Press, 1993

10. Goldreich P, Julian W H. "Pulsar electrodynamics". *Astrophysical Journal* 157 (2) (1969): 869-880 (DOI:10.1086/150119)
11. Goertz C K. "Dusty plasmas in the solar system". *Reviews of Geophysics* 27 (1989): 271 (DOI: 10.1029/RG027i002p00271)
12. Havens O, Melandso F, Aslaksen T K, Nitter T. "Collisionless braking of dust particles in the electrostatic field of planetary dust rings". *Physica Scripta* 45 (5) (1992): 491
13. Siddique M, Rasheed A, Jamil M, Javid A, Sumera P. "KdV acoustic structure with exchange-correlation potential in plasmas". *European Physical J. Plus* 134(6) (2019): 263 (DOI: 10.1140/epjp/i2019-12663-5)
14. Miller H R, Witter P J. *Active Galactic Nuclei*. Berlin: Springer, 1987.
15. Shukla P K, Mamun A A. *Introduction to dusty plasma physics*. Bristol: Institute of Physics Publishing, 2002.
16. Ou J, Zhao X Y, Lin B B. "Dust charging and levitating in a sheath of plasma containing energetic particles". *Chinese Physics B*. 27(2) (2018): 025204 (DOI: 10.1088/1674-1056/27/2/025204)
17. Mamun A A. "Electrostatic solitary structures in a dusty plasma with dust of opposite polarity". *Physical Review E* 77(2) (2008): 026406 (DOI: 10.1103/PhysRevE.77.026406)
18. Mannan A, Mamun A A. "Dust-acoustic solitary waves in a self-gravitating warm opposite polarity dusty plasma". *Waves Random & Complex Media* (2020) (In Press) (DOI: 10.1080/17455030.2020.1853849)
19. Bhowmick S, Sahu B. "Propagation of nonlinear excitations of dust acoustic waves by a moving charged object in superthermal plasmas". *Indian J Physics* (2021) (In Press) (doi: 10.1007/s12648-021-02224-9)
20. Khaled M A H, Shukri M A, Hager Y A A. "Dust acoustic solitons in an opposite polarity dusty plasma in the presence of generalized polarization force". *Physics of Plasmas* 26(10) (2019): 103702 (DOI: 10.1063/1.5099928)
21. Farooq M, Ahmad M, Jan Q. "Polarization force in an opposite polarity dusty plasma with hybrid Cairns-Tsallis distributed electrons". *Contributions to Plasma Physics* 61 (2021): e202000170 (DOI: 10.1002/ctpp.202000170)
22. Haas F. *Quantum Plasmas: An Hydrodynamic Approach*. New York: Springer-Verlag, 2011 (DOI: 10.1007/978-1-4419-8201-8)
23. Haas F. "An Introduction to Quantum Plasmas". *Brazilian J Physics* 41(4) (2011): 349-363 (DOI: 10.1007/s13538-011-0043-0)
24. McKerr M, Kourakis I, Haas F. "Freak waves and electrostatic wave packet modulation in a quantum electron-positron-ion plasma". *Plasma Physics & Controlled Fusion* 56(3) (2014): 035007 (DOI: 10.1088/0741-3335/56/3/035007)
25. Manfredi G, Hervieux P A, Yin Y, Crouseilles N. *Collective Electron Dynamics in Metallic and Semiconductor Nanostructures*, in: Massobrio C, Bulou H, Goyhenex C (eds.) *Advances in the Atomic-Scale Modeling of Nanosystems and Nanostructured Materials. Lecture Notes in Physics* 795 (2010): 1-44 (Springer, Berlin, Heidelberg) (DOI: 10.1007/978-3-642-04650-6_1)
26. Ludwig P, Balzer K, Filinov A, Stolz H, Bonitz M. "On the Coulomb-dipole transition in mesoscopic classical and quantum electron-hole bilayers". *New Journal of Physics* 10(8) (2008): 083031 (DOI: 10.1088/1367-2630/10/8/083031)
27. Markowich, P A., Ringhofer, C A., Schmeiser, C. *Semiconductor Equations*. Vienna: Springer, 1990. (DOI: 10.1007/978-3-7091-6961-2)
28. Killian T C. "Ultracold Neutral Plasmas". *Science* 316(5825) (2007): 705-708 (DOI: 10.1126/science.1130556)
29. Glenzer S H, Landen O L, Neumayer P, Lee R W, Widmann K K, Pollaine S W, Wallace R J, Gregori G, Holl A, Bornath T, Thiele R, Schwarz V, Kraeft W D, Redmer R. "Observations of plasmons in warm dense matter". *Physical Review Letters* 98 (2007): 065002 (DOI: 10.1103/PhysRevLett.98.065002)
30. Harding A K, Lai D. "Physics of Strongly Magnetized Neutron Stars". *Reports on Progress in Physics* 69 (2006): 2631 (DOI: 10.1088/0034-4885/69/9/R03)
31. Haas F, Garcia L G, Goedert J, Manfredi G. "Quantum ion-acoustic waves". *Physics of Plasmas* 10(10) (2003): 3858-3866 (DOI: 10.1063/1.1609446)
32. El-Hanbaly A M, Abulwafa E M, Darweesh H F. "Propagation features of head-on collision dust acoustic solitary waves in four-component quantum plasmas". *Waves Random & Complex Media* 30(4) (2020): 704-721 (DOI: 10.1080/17455030.2018.1555382)
33. Gao D-N. "Multi-dimensional Instability of Dust Acoustic Waves in Magnetized Quantum Plasmas with Positive or Negative Dust". *Brazilian J Physics* 51(1) (2021): 66-74 (DOI: 10.1007/s13538-020-00813-3)

34. Abulwafa E M, Elhanbaly A M, Mahmoud A A, Al-Araby A F. "Arbitrary amplitude double-layers in four-component dusty plasma with q-non-extensive electrons and ions". *Physics of Plasmas* 24(5) (2017): 053704 (DOI: 10.1063/1.4982806)
35. El-Monier S Y, Atteya A. "Bifurcation Analysis for Dust-Acoustic Waves in a Four-Component Plasma Including Warm Ions". *IEEE Transactions on Plasma Science* 46(4) (2018): 815-824 (DOI: 10.1109/TPS.2017.2766097)
36. Abulwafa E M, El-Hanbaly A M, Darweesh H F. "The existence and propagation of dust acoustic waves in quantum four-component plasma". *Waves Random & Complex Media* (2021) (In Press) (DOI: 10.1080/17455030.2021.1963007)
37. Chow V W, Mendis D A, Rosenberg M. "Role of grain size and particle velocity distribution in secondary electron emission in space plasmas". *J Geophysical Research* 98 (11A) (1993): 19065-19076 (DOI: 10.1029/93JA02014)
38. Horanyi M, Mendis D A. "The effects of electrostatic charging on the dust distribution at Halley's Comet". *Astrophysical J* 307(2) (1986): 800-807 (DOI: 10.1086/164466)
39. Mendis D A, Rosenberg M. "Cosmic dusty plasma". *Annual Review of Astronomy & Astrophysics* 32 (1994): 419-463 (DOI: 10.1146/annurev.aa.32.090194.002223)
40. Rao N N, Shukla P K, Yu M Y. "Dust-acoustic waves in dusty plasmas". *Planetary & Space Science* 38(4) (1990): 543-546 (DOI: 10.1016/0032-0633(90)90147-I)
41. Law D A, Steet W H, Annaratine B M, Allen J E. "Probe-induced particle circulation in a plasma crystal". *Physical Review Letters* 80(19) (1998): 4189-4192 (DOI: 10.1103/PhysRevLett.80.4189)
42. Banerjee G, Maitra S. Dust Ion Acoustic Solitary Waves in Quantum Dusty Plasmas: A New Approach to Obtain Sagdeev Potential, in "Applications of Fluid Dynamics", Singh M K, Kushvah B S, Seth G S, Parkash J (Editors) (2018): 483-494 (DOI: 10.1007/978-981-10-5329-0_35)
43. Chaudhuri S, Chowdhury A R. "Four component strongly coupled quantum dusty plasma and generation of dark-bright solitons and double-layers". *Communications in Nonlinear Science & Numerical Simulation* 75 (2019): 236-250 (DOI: 10.1016/j.cnsns.2018.12.002)

© This is an open access article under the (CC)BY-NC license (<https://creativecommons.org/licenses/by-nc/4.0/>). Funded by Al-Farabi KazNU.

P.F. Kashaykin^{2,3} , E.A. Pospelova² , I.E. Kenzhina^{1,5*} ,
 Zh.A. Zaurbekova¹ , S. K. Askerbekov¹ , M.Yu. Salgansky⁴ ,
 A.A. Shaimerdenov¹ , A.U. Tolenova^{1,5} , A.L. Tomashuk² 

¹Kazakh-British Technical University, Almaty, Kazakhstan

²Prokhorov General Physics Institute of the Russian Academy of Sciences,
 Dianov Fiber Optics Research Center, Moscow, Russia

³Institute of Automation and Electrometry SB RAS, Novosibirsk, Russia

⁴G.G. Devyatkh Institute of Chemistry of High-Purity Substances
 of the Russian Academy of Sciences, Nizhny Novgorod, Russia

⁵Satbayev University, Almaty, Kazakhstan

*e-mail: kenzhina@physics.kz

(Received 2 May 2022; received in revised form 18 May 2022; accepted 3 June 2022)

Gamma-radiation-induced attenuation of light in pure-silica core optical fiber in long-wavelength region

Abstract. The dependences of the spectra of radiation-induced attenuation (RIA) of light in a pure-silica core (PSC) optical fiber (OF) during and after gamma-irradiation up to 590 kGy at a dose rate of 7.6 Gy/s in the near infrared range have been investigated. It was shown that starting with an absorbed dose of ~100 kGy, the RIA at 1550 nm becomes larger than at 1310 nm due to an increase in long-wavelength (LWL) RIA. The absorption band, with a maximum at a wavelength near 1800 nm, responsible for the LWL RIA is fully defined for the first time. At an absorbed dose of 590 kGy at wavelengths of 1310 and 1550 nm, the RIA is 14.1 and 23.3 dB/km, respectively. During 3.5 years of annealing of the OF at room temperature the RIA in the entire spectral range of 1100-1700 nm decreases by 40-50%. The LWL RIA can be complex, consisting of short-lived and long-lived components. The short-lived component may be LTIRA (low temperature infra-red absorption).

Key words: Optical fibers, radiation-induced attenuation, RIA, pure-silica core fiber, long-wavelength RIA.

Introduction

Optical fibers (OF) have currently found wide application in various fields of science and technology from high-speed information transmission to fiber lasers and precision sensors of various physical quantities. Nevertheless, the use of OFs in nuclear and fusion installations, including the international experimental fusion reactor ITER, leads to degradation of their optical properties due to the appearance of additional radiation-induced attenuation (RIA) of light [1-4]. This phenomenon considerably limits the use of OF in conditions of increased radiation levels and, therefore, there is an urgent need to reduce RIA to an acceptable level for a particular application.

It is known [5] that OFs will be used in the ITER diagnostic systems as transport from fiber-optic sensors operating at a wavelength of $\lambda=1550$ nm. When exposed to ionizing radiation, the optical transmittance at this wavelength is significantly reduced due to the long-wavelength (LWL) RIA with a maximum at wavelengths $\lambda>1600$ nm. Unfortunately, the physical nature and basic properties of this RIA remain questionable. It is worth noting that it is the LWL RIA that limits the radiation resistance of OF in applications in intense gamma-neutron fields and is a limiting factor for a wider implementation of OF in diagnostic and control systems in nuclear and fusion facilities. Therefore, the study of the mechanisms of occurrence and properties of long-wavelength RIA

is an important and urgent task for OF applications at increased levels of ionizing radiation, especially in strong radiation fields.

It is known that the most radiation-resistant are OFs with a pure silica core (PSC) and fluorine-doped silica core [6]. During reactor irradiation, radiation color centers (RCCs) are formed in the glass network of a fiber core, which absorb the light signal propagating through the fiber at the operating wavelength. This is the main cause of the RIA. The relevant wavelength for many OF applications is telecommunication wavelengths of 1310-1550 nm. RIA at these wavelengths is determined by the "tails" of the RCC absorption bands with maximums in the short-wavelength (SWL) and LWL regions. Since the majority of RCCs are located in the visible and UV range, the main works available in the scientific literature [1, 2, 7] are devoted specifically to the study of SWL RIA. And, thus, the main RCCs responsible for SWL RIA, the mechanisms of their formation, and their main properties are known. However, all these data are practically absent in the case of LWL RIA. In general, there are no papers on systematic studies of the properties of LWL RIA in the scientific literature.

It is only known that it is determined by the appearance of an absorption band with a maximum at a wavelength of $\lambda > 1700$ nm [8]. The amplitude of this band grows monotonically with irradiation and becomes the main mechanism of RIA, limiting the radiation resistance in the near-infrared range at high absorbed doses [8-10], corresponding to applications in reactor facilities.

There are two main hypotheses about the nature of this RIA. The first one was formulated back in the late 1990s and consists in the fact that the LWL RIA, according to the authors [11], is caused by changes in the vibrational spectra of the glass network due to the appearance of structural defects of the three-coordinated silicon atom type due to the breaking of regular Si-O bonds. However, in this case, the RIA would have to grow structureless with increasing wavelength in the 1500-2500 nm wavelength range, but subsequent work has shown that the absorption band of LWL RIA should reach a maximum at 1800-2200 nm [8], with its behavior similar to LTIRA (low temperature infrared-red absorption) [12, 13] of self-trapped holes (self-trapped holes STH). Therefore, a number of papers [8, 9, 14] have suggested that this RIA is also caused by STH absorption. However, it is known that STH have extremely low thermostability [15],

and LWL absorption is highly stable even at room temperature.

Hence, the lack of understanding of the physical nature of LWL RIA, the mechanisms of appearance and its properties is a weighty limiting factor for further implementation of fiber-optic controls in applications in intense radiation fields.

This work is devoted to a study of the behavior of LWL RIA in pure-silica-core OF during and after gamma irradiation in the near-infrared range.

Materials and Methods

In Devyatykh Institute of Chemistry of High-Purity Substances of RAS a preform with a pure-silica-core and a F-doped cladding with refractive index difference $\Delta n \sim 0.0095$ (Figure 1) was made by MCVD (Modified Chemical Vapor Deposition). The reflective cladding (2 in Figure 1) contained about 2 wt% fluorine appearance.

An OF with an outer diameter of 125 μm in acrylate coating was drawn from the preform at the Dianov Fiber Optics Research Center of RAS. Optical loss at a wavelength of 1550 nm did not exceed 0.3 dB/km. The cutoff wavelength of the first higher mode was $\lambda_c = 1480$ nm.

Investigations of optical loss in the initial and gamma-irradiated lightguide were performed by the "cut-off" technique in the range of 900-2100 nm using a spectral setup based on the MDR-12 monochromator, the light source was a halogen lamp.

To study the RIA spectra, 100 m of OF was wound on a plastic coil 160 mm in diameter and 100 mm in height. The OF was irradiated with a ^{60}Co γ -source with an average gamma-quantum energy of 1.25 MeV at a dose rate of 7.6 Gy/s. The entire irradiation process can be divided into two stages. In the first one, the OF was irradiated for 180 min followed by relaxation for 30 min. In the second one, the OF was irradiated for 1112 min followed by relaxation for 15 min. The irradiation was conducted at $+25^\circ\text{C}$ until the time of 1082 min, after which the temperature increased to $+40^\circ\text{C}$ when the ventilation was switched off.

Near-infrared spectra were recorded using an Avantes AvaNIR 128 spectrometer (900-1700 nm) with a HL-2000 halogen lamp as the light source. In the first stage of the irradiation, the recording step was 1 min, and in the second stage, 30 min, except for the second relaxation, where the step was also 1 min. To minimize the photobleaching phenomenon,

the visible light was cut off using a $\lambda > 900$ nm filter, so that the injected light power did not exceed 0.5 μ W. The absorbed dose for the whole irradiation

was ~ 590 kGy. The spectra of total optical loss of the irradiated OF were taken after 3.5 years of irradiation.

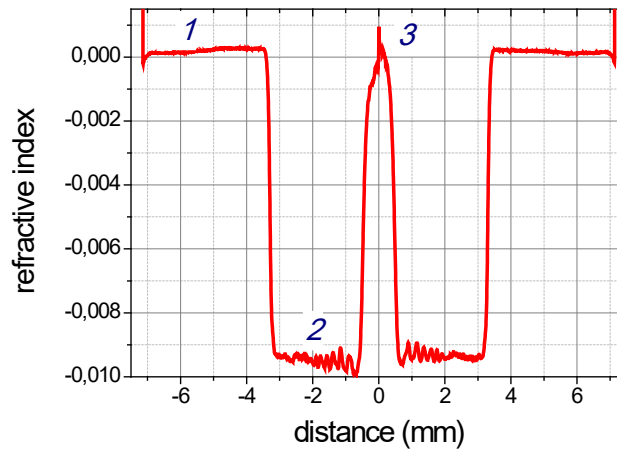


Figure 1 – Fiber refractive-index profile:
1- substrate tube, 2- F-doped reflective cladding, 3- pure silica core.

Results and Discussion

Figure 2 shows the dependence of RIA during irradiation and relaxation at wavelengths of 1310 nm and 1550 nm. At the first stage of irradiation RIA (up to 180 min) at wavelength 1310 nm is greater than at 1550 nm. At the very beginning of gamma exposure there is a sharp increase in RIA up to absorbed dose ~ 3.7 kGy (point 1 on Figure 2), after that RIA begins to decrease, herewith so-called transient absorption is greater at 1310 nm, at maximum it reaches 17.5 dB/km.

The spectra (Figure 3a) show that this RIA is due to the absorption band with a maximum at wavelengths $\lambda < 1000$ nm. This dependence of the RIA is standard for PSC OF [16-18]. This behavior is known to be characteristic of the absorption of self-trapped holes STH, which have absorption bands at 660 and 760 nm [15, 16]. The rapid relaxation after 180 min of irradiation is also due to the thermal decay of STH at room temperature because of their low thermal stability [15, 19].

We can see from the spectra (Figure 3a) that the SWL RIA tail from STH actually decreases during irradiation (spectra 1, 2) and relaxation (spectrum 3). However, the spectra also show that the LWL RIA begins to grow as well. The LWL RIA is due to the relaxation of loss at 1550 nm to a higher level (Figures 2 and 3a).

At the beginning of the second stage of irradiation we see a similar picture: RIA at 1310 nm increases sharply up to the level of 15 dB/km and then begins to decrease during irradiation (Figures 2 and 3b). Starting with an absorbed dose of 96.7 kGy (242 min. in Figure 2) the RIA at 1550 nm wavelength already becomes larger than at 1310 nm. The spectra (Figure 3b) show that this is due to the fact that the LWL RIA begins to prevail over the SWL RIA. Similar RIA kinetics are also observed during reactor irradiation of OF [3,4], which suggests similar mechanisms for the appearance of LWL RIA during both gamma- and mixed gamma-neutron irradiation.

Interesting is the behavior of RIA when the temperature increases from 25 to 40 °C (points 5-6 in Figure 2). It can be seen that there is a decrease in RIA caused by the thermal decay of the RCC. The spectra (Figure 3b) show that the SWL tail mainly decreases, indicating the low thermal stability of STH. However, there is a small relaxation in the LWL region as well (Figure 2). Indeed, it was shown in [3] that increasing the temperature during reactor irradiation from 200 to 350 °C results in a 15-30% decrease in RIA at the 1550 nm wavelength. Therefore, increasing the temperature can be used to reduce the LWL RIA.

After stopping irradiation at an absorbed dose of 590 kGy for 15 minutes, relaxation of RIA occurs at

both wavelengths (Figure 2). From RIA spectra (Fig. 3b) one can see that the SWL tail relaxes to a greater extent and the LWL one much less. At an absorbed dose of 590 kGy, the RIA at 1310 nm was 14.1 dB/km and 23.3 dB/km at 1550 nm. After 15 minutes of relaxation, the RIA at 1310 and 1550 nm was 11.1 and 20.7

dB/km, respectively. The presence of a fast relaxation component of the LWL absorption (Figure 3b) may indicate that the LWL RIA is complex, the fast component of which may be LTIRA (low temperature infra-red absorption) [12], whose maximum band also lies in the spectral region of $\lambda > 1700$ nm.

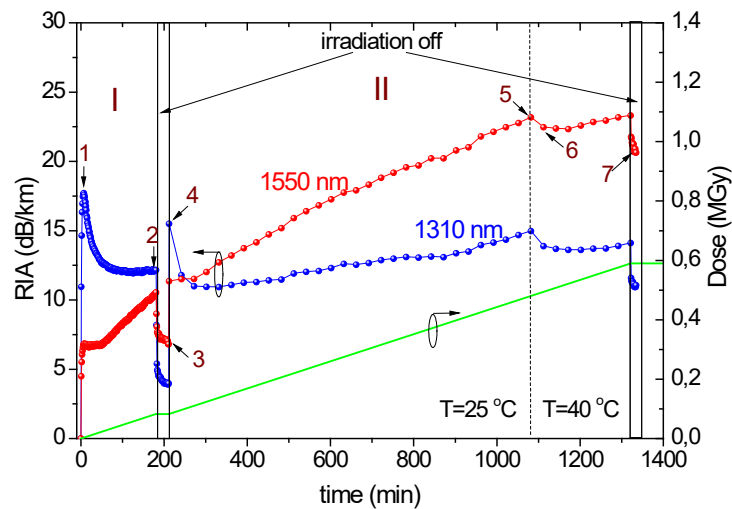


Figure 2 – RIA and dose (green curve) evolution with time of irradiation and post-irradiation recovery at wavelengths 1310 nm (red curve), 1550 nm (blue curve).

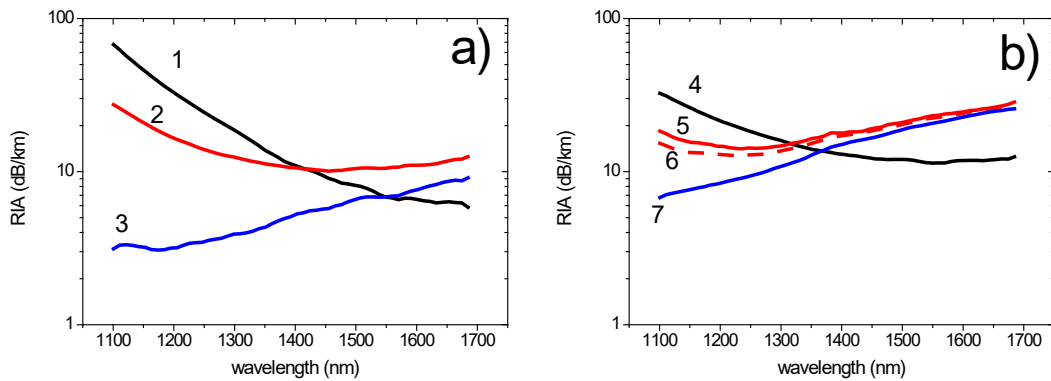


Figure 3 – a) RIA spectra during irradiation and relaxation at I stage of irradiation (points 1 – 3.7 kGy, 2 – 82 kGy, 3 – 30 min of relaxation after 82 kGy), b) – at II stage of irradiation 4 – 82.5 kGy, 5- 479.7 kGy, 6 – 480.2 kGy, 7 – 15 min of relaxation after 590 kGy). Temperature $T=25$ °C for spectra 1-5 and $T=40$ °C for -6-7.

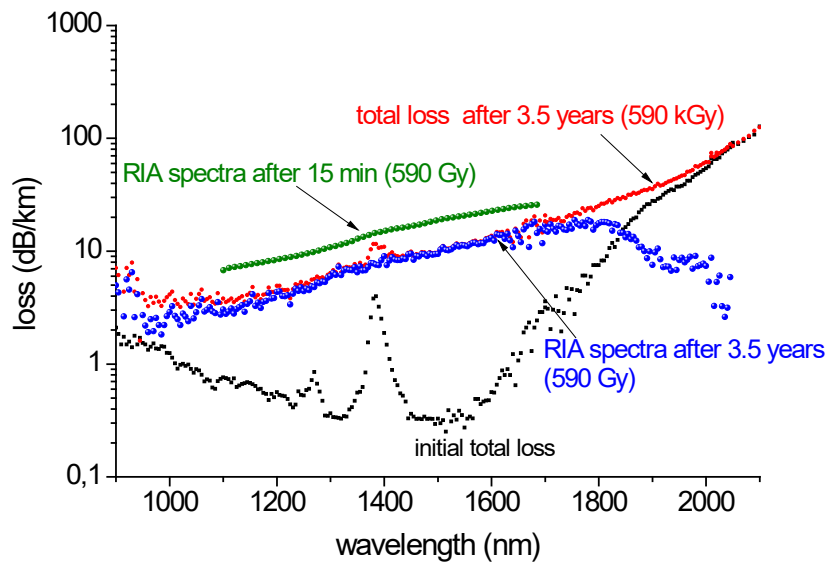


Figure 4. Spectrum of optical loss. Initial loss (black dots), loss 3.5 years after irradiation with a dose of 590 kGy (red dots), RIA spectrum after 15 min (green dots) and 3.5 years (blue dots) after irradiation.

Figure 4 shows the spectra of total and radiation-induced optical loss. From the spectra of total optical loss for the initial OF and irradiated to a dose of 590 kGy it is clear that in the LWL region starting from 2000 nm the spectra coincide (Figure 4). Similar spectra of initial and irradiated optical fibers were obtained in [10] for light guides with a germanium-doped core and in [8] for optical fibers with pure- and nitrogen-doped silica core. From the difference in the spectra of total loss of the irradiated and initial OF, we find the RIA spectrum, from which it is clear that an asymmetric band with a maximum at a wavelength near 1800 nm with a gentle SWL part and a steep decline in the LWL part is responsible for the LWL absorption. Note that a similar RIA band was observed in [8], but the LWL decline of the RIA band was not prescribed. Therefore, in this study, we observed the absorption band responsible for the LWL RIA in its full form for the first time.

This band is very similar to LTIRA by its maximum position and spectrum shape, which is caused by STH absorption [12]. The hypothesis that the LWL RIA belongs to LTIRA, as noted above, was previously stated in [9, 14, 20] and the obtained RIA spectrum (Fig.4) also supports this hypothesis. However, LTIRA is known to be stable only at low temperatures, while long-wave RIA is highly stable at room temperature. Comparing the spectrum of RIA registered after

15 min and after 3.5 years, we can see that after irradiation in the entire spectral range 1100-1700 nm at room temperature, the relaxation of RIA occurs by only 40-50%. Despite the new information obtained on the behavior of long-wave RIA, the question of determining the physical nature of LWL RIA and its main properties remains open.

Conclusion

The dependence of RIA in the PSC OF during and after gamma-irradiation up to 590 kGy at a dose rate of 7.6 Gy/s in the near-IR range has been investigated. The mechanisms affecting RIA in the near-infrared range have been established: absorption of STHs having bands with maximums at 660 and 760 nm and LWL absorption.

It was shown that starting with an absorbed dose of ~100 kGy, the RIA at 1550 nm becomes larger than at 1310 nm because of the prevalence of LWL RIA over STH absorption. For the first time, the absorption band, with a maximum at wavelength around 1800 nm, responsible for the LWL RIA is fully defined. At an absorbed dose of 590 kGy at wavelengths of 1310 and 1550 nm, the RIA is 14.1 and 23.3 dB/km, respectively. During 3.5 years of annealing of the OF at room temperature the RIA in the entire spectral range of 1100-1700 nm decreases by 40-50%.

Acknowledgments

The work is supported by the Committee of Science of Ministry of Education and Science of the Republic of Kazakhstan with Grant No. AP13068019.

Authors thank the staff of the Large-scale research facilities "Fibers" (UNU Fibers) of GPI RAS for the fabrication and characterization of the used fibers. IA&E part is supported by RF state budget (№ 121030500067-5).

References

- Girard, S., et al. "Overview of radiation induced point defects in silica-based optical fibers." *Reviews in Physics* 4 (2019): 100032.
- Girard S. et al. "Radiation effects on silica-based optical fibers: Recent advances and future challenges." *IEEE Transactions on Nuclear Science* 60, 3 (2013): 2015-2036.
- Kashaykin, P. F., et al. "Radiation Resistance of Single-Mode Optical Fibers at $\lambda = 1.55 \mu\text{m}$ Under Irradiation at IVG. 1M Nuclear Reactor." *IEEE Transactions on Nuclear Science* 67, 10 (2020): 2162-2171.
- Kashaykin, P. F., et al. "Radiation resistance of single-mode optical fibres with view to in-reactor applications." *Nuclear Materials and Energy* 27 (2021): 100981.
- Dulon, Krista. Optic sensors. Testing the resistance to radiation ITER Newsline. <https://www.iter.org/newsline/-/3062>. (accessed April, 12, 2022).
- Wijnands, Th., De Jonge, L. K., Kuhnhen, J., Hoeffgen, S. K., and Weinand, U. "Optical absorption in commercial single mode optical fibers in a high energy physics radiation field." *IEEE Transactions on Nuclear Science* 55, 4 (2008): 2216-2222.
- Girard, Sylvain, et al. "Recent advances in radiation-hardened fiber-based technologies for space applications." *Journal of Optics* 20, 9 (2018): 093001.
- Zabekhailov, M. O., et al. "Radiation-induced absorption in optical fibers in the near-infrared region: the effect of H₂-and D₂-loading." *IEEE RADECS 2001. 2001 6th European Conference on Radiation and Its Effects on Components and Systems (Cat. No. 01TH8605)* (2001): 192-194.
- Anoikin, E. V., et al. "UV and gamma radiation damage in silica glass and fibres doped with germanium and cerium." *Nuclear Instruments and Methods in Physics Research Section B: Beam Interactions with Materials and Atoms* 65, 1-4 (1992): 392-396.
- Henschel, H., and Kohn, O. "Regeneration of irradiated optical fibres by photobleaching?." *IEEE Transactions on Nuclear Science* 47, 3 (2000): 699-704.
- Kyoto, M., et al. "Gamma-ray irradiation effect on loss increase of single mode optical fibers (I) loss increase behavior and kinetic study." *Journal of Nuclear Science and Technology* 26, 5 (1989): 507-515.
- Chernov, P. V., et al. "Spectroscopic manifestations of self-trapped holes in silica." *Physica Status Solidi B* 156, 2 (1989): 663-675.
- Kashaykin, P.F., Tomashuk, A.L., Khopin, V.F., Firstov, S.V., Guryanov, A.N., Dianov, E.M. "Observation of radiation-induced absorption of self-trapped holes in Ge-doped silica fiber in near infrared range at reduced temperature." *Journal of Non-Crystalline Solids* 496 (2018): 24-28.
- Tomashuk, A. L., et al. "Performance of special radiation-hardened optical fibers intended for use in the telecom spectral windows at a megagray level." *IEEE RADECS 97. Fourth European Conference on Radiation and its Effects on Components and Systems (Cat. No. 97TH8294)* (1997): 1566-1569.
- Griscom, D. L. "Self-trapped holes in pure-silica glass: A history of their discovery and characterization and an example of their critical significance to industry." *Journal of non-crystalline solids* 352, 23-25 (2006): 2601-2617.
- Kashaykin, Pavel F., et al. "Anomalies and peculiarities of radiation-induced light absorption in pure silica optical fibers at different temperatures." *Journal of Applied Physics* 121, 21 (2017): 213104.
- Kashaykin, P. F., et al. "Radiation-induced attenuation in silica optical fibers fabricated in high O₂ excess conditions," *Journal of Lightwave Technology* 33, 9 (2015): 1788-1793.
- Kashaykin, Pavel F., et al. "Silica optical fibers with high oxygen excess in the core: a new type of radiation-resistant fiber." *Micro-structured and Specialty Optical Fibres IV. International Society for Optics and Photonics, 2015. Proceedings of the SPIE 9507* (2015): 950705.

19. Tomashuk, A. L., et al. "1.55- μm -light absorption induced by pulsed-X-ray radiation in pure-silica-core fiber: Effects of light power and temperature." *Journal of Non-Crystalline Solids* 521 (2019): 119504.

20. Regnier, E., et al. "Low-dose radiation-induced attenuation at infrared wavelengths for P-doped, Ge-doped and pure silica-core optical fibres." *IEEE transactions on nuclear science* 54, 4 (2007): 1115-1119.

© This is an open access article under the (CC)BY-NC license (<https://creativecommons.org/licenses/by-nc/4.0/>). Funded by Al-Farabi KazNU.

G.B. Suliyeva¹ , K.A. Boshkayev^{1,2*} , G. Nurbakyt¹ ,
 H. Quevedo^{1,3,4} , A.S. Taukenova^{1,2} , A.T. Tlemissov⁵ ,
 Zh.A. Tlemissova⁵ , A. Urazalina^{1,2} 

¹Al-Farabi Kazakh National University, Almaty, Kazakhstan

²National Nanotechnology Laboratory of Open Type (NNLOT), Almaty, Kazakhstan

³Universidad Nacional Autónoma de México, Mexico

⁴Università di Roma “La Sapienza”, Roma, Italy

⁵Silesian University in Opava, Opava, Czech Republic

*e-mail: kuantay@mail.ru

(Received 22 April 2022; accepted 30 May 2022)

Adiabatic theory of motion of bodies in the hartle-thorne spacetime

Abstract: We study the motion of test particles in the gravitational field of a rotating and deformed object within the framework of the adiabatic theory. For this purpose, the Hartle-Thorne metric written in harmonic coordinates is employed in the post-Newtonian approximation where the adiabatic theory is valid. As a result, we obtain the perihelion shift formula for test particles orbiting on the equatorial plane of a rotating and deformed object. Based on the perihelion shift expression, we show that the principle of superposition is valid for the individual effects of the gravitational source mass, angular momentum and quadrupole moment. The resulting formula was applied to the inner planets of the Solar system. The outcomes are in a good agreement with observational data. It was also shown that the corrections related to the Sun's angular moment and quadrupole moment have little impact on the perihelion shift. On the whole, it was demonstrated that the adiabatic theory, along with its simplicity, leads to correct results, which in the limiting cases correspond to the ones reported in the literature.

Key words: adiabatic theory, the Hartle-Thorne metric, post-Newtonian approximation, harmonic coordinates, perihelion shift.

Introduction

In most cases, real astrophysical objects rotate and their shapes are different from a sphere. Therefore, when one considers the motion of test particles in the gravitational field of real objects, it is necessary to account for the influence of both proper rotation and deformation of the source. A convenient way to consider the geometry of the source is to study its multipole moments of which the most important are the mass M , angular momentum J , and quadrupole moment Q . The solution to the field equations for a static, spherically symmetric object in vacuum is well-known in the literature as the Schwarzschild metric [1]. This solution describes new effects that could not be explained within the classical Newtonian theory of gravity [2, 3]. In 1918, Lense and Thirring derived an approximate external solution that takes into account the rotation of the source up to the first order in the angular momentum [4]. According to

this work, rotation generates an additional gravitational field which leads to the dragging of inertial frames (known as the Lense-Thirring effect). In 1959, Erez and Rosen derived a solution for a static, axially symmetric object by including of a quadrupole parameter [5]. However, the first approximate solution that takes into account both angular momentum and quadrupole moment was found by Hartle and Thorne in 1968 [6, 7]. This solution allows us to investigate the external gravitational field of astrophysical objects, starting from massive main sequence stars up to neutron and quark stars [8]. It should be mentioned that there are several vacuum exact solutions to the Einstein field equation, which account for higher-order multipole moments with additional parameters such as electric charge, dilatonic charge, scalar fields, etc [9 – 12]. However, for simplicity, here we will focus on the approximate Hartle and Thorne solution and will study the motion of test bodies within the adiabatic theory.

An interesting approach for studying the motion of test particles in general relativity was proposed by Abdildin [13, 14], by using the conceptual framework developed by Fock [15]. In Ref. [13], the Fock metric was generalized to consider the rotation of the source (up to the second order in the angular momentum) and its internal structure in the post-Newtonian ($\sim 1/c^2$) approximation, where c is the speed of light in vacuum. This extended Fock metric was originally presented in harmonic coordinates, which facilitate the study of the motion of test particles by using the vectors associated to the trajectories. One of the most important consequences of Abdildin's works was the implementation of the adiabatic theory to study the motion of bodies in general relativity [14], which drastically simplifies the form of the equations of motion derived previously in [16, 17]. In this work, we will show this advantage explicitly for the motion of test particles in the gravitational field of a rotating deformed object.

The work is organized as follows. In Section 1, we introduce the basic concepts of the adiabatic theory. In Section 2, we present the external Hartle-Thorne solution, which is then implemented in Section 3 within the framework of the adiabatic theory to obtain an expression for the perihelion shift. Then, in Section 4, we compute the shift for the inner planets of the Solar system. Finally, Section 5 contains the conclusions of our analysis.

Adiabatic theory

The application of adiabatic theory for the investigation of motion in general relativity, as proposed in [14] for closed orbits, is based on the use of the vector elements of the orbits, asymptotic methods of the theory of nonlinear oscillations, and adiabatic invariants.

The main idea is that the motion can be described by a Lagrangian which is essentially the perturbation of a known Lagrangian. Consider, for instance, the Kepler problem for the motion of a relativistic particle in a central field. Then, corresponding perturbed Lagrangian function can be expressed as

$$L = -mc^2 + \frac{mv^2}{2} + \frac{Gmm_0}{r} + F(\vec{r}, \vec{v}), \quad (1)$$

where F is the perturbation function. Accordingly, the corresponding Hamilton function is written as

$$H = mc^2 - \frac{p^2}{2m} - \frac{Gmm_0}{r} - F(\vec{r}, \vec{v}), \quad (2)$$

where $\vec{p} = \partial L / \partial \vec{v}$ is the momentum of the test particle.

The motion of a test particle can be described by the orbital angular momentum vector \vec{M} and the Laplace-Runge-Lenz vector \vec{A} , which are integrals of motion defined as:

$$\vec{M} = [\vec{r} \times \vec{p}], \quad (3)$$

$$\vec{A} = \left[\frac{\vec{p}}{m} \times \vec{M} \right] - \frac{Gm_0 m}{r} \vec{r}, \quad A = Gm_0 m e, \quad (4)$$

where A is the magnitude (absolute value) of the Laplace-Runge-Lenz vector, \vec{r} is the radius vector of the test particle, G is the gravitational constant, m_0 is the mass of a gravitational source (central object), m is the mass of the test particle, and e is the orbit eccentricity. The vectors \vec{M} and \vec{A} characterize the shape and position of the orbit in space. Namely, the vector \vec{M} is directed perpendicularly to the orbit plane and the vector \vec{A} is directed towards the perihelion of the orbit. Thus, one can write the equations of motion in a general form as follows:

$$\frac{d\vec{M}}{dt} = \frac{dM}{dt} \vec{e}_M + [\vec{\Omega} \times \vec{M}], \quad (5)$$

$$\frac{d\vec{A}}{dt} = \frac{dA}{dt} \vec{e}_A + [\vec{\Omega} \times \vec{A}], \quad (6)$$

where \vec{e}_M , \vec{e}_A are the unit vectors directed along \vec{M} and \vec{A} , respectively, and $\vec{\Omega}$ is the angular velocity of rotation of the ellipse "as a whole", which is the sought function in this theory. The explicit form of $\vec{\Omega}$ depends on the considered physical system. In Ref. [13], it is shown that the angular velocity can be computed as

$$\vec{\Omega} = \frac{\partial \bar{H}}{\partial \vec{M}}, \quad (7)$$

where \bar{H} is the Hamiltonian averaged over the period of the test particle's Keplerian orbit. The averaged Hamiltonian depends on the orbital angular momentum \vec{M} and the adiabatic invariant M_0 of the system

$$M_0 = \frac{M}{\sqrt{1 - \frac{A^2}{\alpha^2}}}. \quad (8)$$

where $\alpha = Gm_0m$.

The knowledge of the angular velocity $\vec{\Omega}$ allows us to investigate many relativistic effects without solving Eqs. (5) and (6) explicitly. The invariant (8) allows to write Eqs. (5) and (6) in a more compact form as

$$\frac{d\vec{M}}{dt} = \frac{dM}{dt} \vec{e}_M + [\vec{\Omega} \times \vec{M}], \quad (9)$$

$$\frac{d\vec{e}_A}{dt} = [\vec{\Omega} \times \vec{e}_A], \quad (10)$$

Thus, in the adiabatic theory, Eqs. (9) and (10) and the expression (7) are the mathematical basis for

the investigation of the motion of bodies. In other words, these equations completely solve the problem of evolution in the quasi-Kepler problem.

In Fig. 1, we show the position of the vector elements and the proper angular momentum of the central object \vec{J} , which is directed along the z axis. Note that when $\theta = \pi/2$ the directions of \vec{M} and \vec{J} coincide with the z axis.

Hartle-Thorne metric

The Hartle-Thorne metric is an approximate vacuum solution of the Einstein field equations. It describes well enough the gravitational field of rotating deformed astrophysical objects and, therefore, it is chosen as an example in this work. Its general form (in geometric units $G = c = 1$) in spherical coordinates (t, R, Θ, φ) is given by

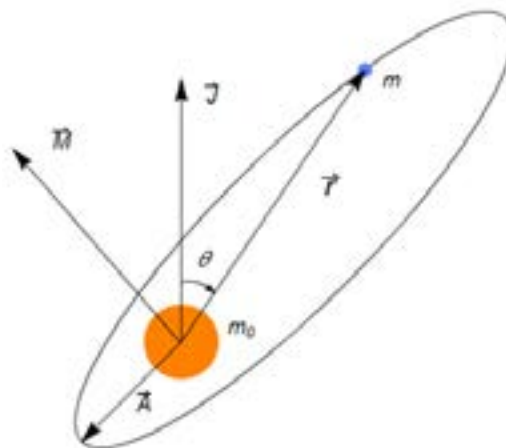


Figure 1 – Schematic illustration of a central object and a test particle with its vector elements, where θ is the polar angle between the z axis and the radius vector \vec{r}

$$ds^2 = - \left(1 - \frac{2m_0}{R}\right) \left[1 + 2k_1 P_2(\cos \Theta) - 2 \left(1 - \frac{2m_0}{R}\right)^{-1} \frac{J^2}{R^4} (2 \cos^2 \Theta - 1)\right] dt^2 + \\ + \left(1 - \frac{2m_0}{R}\right)^{-1} \left[1 - 2 \left(k_1 - \frac{6J^2}{R^4}\right) P_2(\cos \Theta) - 2 \left(1 - \frac{2m_0}{R}\right)^{-1} \frac{J^2}{R^4}\right] dR^2 + \\ + R^2 [1 - 2k_2 P_2(\cos \Theta)] (d\Theta^2 + \sin^2 \Theta d\varphi^2) - \frac{4J}{R} \sin^2 \Theta dt d\varphi, \quad (11)$$

where

$$k_1 = \frac{J^2}{m_0 R^3} \left(1 + \frac{m_0}{R}\right) + \frac{5Q - J^2/m_0}{8 m_0^3} Q_2^2(x), \quad (12)$$

$$k_2 = k_1 + \frac{J^2}{R^4} + \frac{5Q - J^2/m_0}{4m_0^2 R} \left(1 - \frac{2m_0}{R}\right)^{-1/2} Q_2^1(x) \quad (13)$$

are functions of the R coordinate, and

$$\begin{aligned} Q_2^1(x) &= (x^2 - 1)^{1/2} \left[\frac{3x}{2} \ln \left(\frac{x+1}{x-1} \right) - \frac{3x^2 - 2}{x^2 - 1} \right], \\ Q_2^2(x) &= (x^2 - 1) \left[\frac{3}{2} \ln \left(\frac{x+1}{x-1} \right) - \frac{3x^3 - 5x}{(x^2 - 1)^2} \right] \end{aligned} \quad (14)$$

are the associated Legendre functions of the second kind [18, 19], $P_2(\cos \Theta)$ is the Legendre polynomial, and $x = R/m_0 - 1$. This metric is characterized by three parameters: the source mass m_0 , angular momentum J (up to the second order), and quadrupole moment Q (up to the first order).

The Hartle-Thorne metric describes the gravitational field of slowly rotating and slightly deformed astrophysical objects [20]. The metric [11] can be reduced by appropriate coordinate transformations to the Fock metric [21], to the Kerr metric [22], and to the Erez-Rosen metric [23, 24] in the corresponding limiting cases. For the purpose of this work, the metric [11] must be written in harmonic coordinates and expanded in a series of powers of $1/c^2$.

Harmonic coordinates are important for many problems in general relativity [15]. Such coordinates are associated with the conditions under which spacetime is considered homogeneous and isotropic at large distances from the gravitational field source. In turn, a consequence of the homogeneity and

isotropy of the spacetime is the conservation of energy, momentum and angular momentum, which are in fact first integrals of the motion equations. In general, harmonic coordinates can be used in the study of gravitational fields generated by ordinary stars [25], black holes [26], as well as in the study of quantum gravity [27], supergravity [28], and in numerical relativity [29].

It should be emphasized that the geodesics in the Hartle-Thorne spacetime have been studied in the literature both analytically and numerically [30 – 32]. Here, unlike in the literature, we employ an alternative method to derive the perihelion shift formula in post-Newtonian physics.

Method

As already mentioned, in the present work we need the Hartle-Thorne metric expanded in powers of $1/c^2$. In harmonic coordinates it is written as follows [21, 33]:

$$\begin{aligned} ds^2 &= \left[1 - \frac{2Gm_0}{c^2 r} + \frac{2GQ}{c^2 r^3} P_2(\cos \theta) + \frac{2G^2 m_0^2}{c^4 r^2} - \frac{4G^2 m_0 Q}{c^4 r^4} P_2(\cos \theta) \right] c^2 dt^2 - \\ &- \left[1 + \frac{2Gm_0}{c^2 r} - \frac{2GQ}{c^2 r^3} P_2(\cos \theta) \right] [dr^2 + r^2(d\theta^2 + \sin^2 \theta d\varphi^2)] + \frac{4GJ}{c^2 r} \sin^2 \theta dt d\varphi, \end{aligned} \quad (15)$$

This representation allows us to explicitly identify relativistic corrections. Thus, in the g_{tt} component of the metric tensor, the first three terms refer to the Newtonian theory and the last two terms to the relativistic theory because of the multiplier c^2

outside the parenthesis. Moreover, terms proportional to $1/c^2$ also appear in the spatial part of the metric.

Now, directly from the metric (15) one finds the Lagrange function of the test particle

$$\begin{aligned} L = -mc \frac{ds}{dt} &= -mc^2 + \frac{mv^2}{2} + \frac{Gm_0 m}{r} - \frac{GmQ}{r^3} P_2(\cos \theta) + \frac{m}{2c^2} \left[\frac{v^4}{4} + \frac{3Gm_0 v^2}{r} - \frac{G^2 m_0^2}{r^2} \right] + \\ &+ \frac{m}{2c^2} \left[-\frac{3Gv^2 Q}{r^3} P_2(\cos \theta) + \frac{2G^2 m_0 Q}{r^4} P_2(\cos \theta) - \frac{4G(\vec{v} \cdot [\vec{r} \times \vec{J}])}{r^3} \right], \end{aligned} \quad (16)$$

and besides

$$\vec{v} = \frac{d\vec{r}}{dt}, v^2 = \frac{dr^2 + r^2(d\theta^2 + \sin^2 \theta d\varphi^2)}{dt^2}. \quad (17)$$

Only in harmonic and isotropic coordinates, it is possible to write the linear velocity in the form indicated above.

Next, it is necessary to derive the Hamiltonian, which we will subsequently average. The expression to determine the Hamilton function is given as [34]:

$$H = (\vec{p} \cdot \vec{v}) - L, \quad (18)$$

First, we look for the form of the generalized momentum \vec{p} . Thus,

$$\vec{p} = \frac{\partial L}{\partial \vec{v}} = \left[1 + \frac{v^2}{2c^2} + \frac{3Gm_0}{c^2 r} - \frac{3GQ}{c^2 r^3} P_2(\cos \theta) \right] m\vec{v} - \frac{2Gm}{c^2 r^3} [\vec{r} \times \vec{J}]. \quad (19)$$

Taking into account (16) – (19), the Hamiltonian takes the following form:

$$H = mc^2 + \frac{p^2}{2m} - \frac{Gm_0 m}{r} + \frac{GmQ}{r^3} P_2(\cos \theta) - \frac{p^4}{8c^2 m^3} - \frac{3Gm_0 p^2}{2c^2 m r} + \frac{G^2 m_0^2 m}{2c^2 r^2} + \frac{3GQ p^2}{2c^2 m r^3} P_2(\cos \theta) - \frac{G^2 m_0 m Q}{c^2 r^4} P_2(\cos \theta) + \frac{2G(\vec{p} \cdot [\vec{r} \times \vec{J}])}{c^2 r^3}. \quad (20)$$

For simplicity, we consider the motion of test particle on the equatorial plane, i.e., $\theta = \pi/2$. Now, according to the adiabatic theory, we should average each term in (20) over the period T , where the average of a function f is defined as:

$$\bar{f} = \frac{1}{T} \int_0^T f dt. \quad (21)$$

In this work, for convenience, averaging is carried out using the non-relativistic orbital angular momentum M in polar coordinates

$$M = mr^2 \frac{d\varphi}{dt}, \quad (22)$$

which allows us to change from an integral over t to and integral over φ . Here, we use the solution to the Kepler problem [34]

$$r = \frac{P}{1 + e \cos \varphi}, 0 < \varphi < 2\pi, \quad (23)$$

where e is the orbit eccentricity as before, P is the semilactus rectum, and φ is the polar angle. Therefore, it turns out that

$$\begin{aligned} \bar{f} &= \frac{1}{T} \int_0^{2\pi} f(\varphi) \frac{dt}{d\varphi} d\varphi = \\ &= \frac{m}{TM} \int_0^{2\pi} f(\varphi) r^2 d\varphi. \end{aligned} \quad (24)$$

In addition, to average terms in Eq. (20) with the momentum $\vec{p} = m\vec{v}$, we use the following form of the test particle velocity:

$$\vec{v} = \frac{M}{mP} \{-\vec{i} \sin \varphi + \vec{j}(e + \cos \varphi)\}. \quad (25)$$

It is also important to mention that one is free to choose the direction of the central body rotation. For simplicity and practical purposes, it is preferred to align it along the z axis as $\vec{J} = J\vec{k}$. For a test particle moving in the equatorial plane, its orbital angular momentum direction coincides with the proper angular momentum of the central body, i.e., $\vec{M} \uparrow\uparrow \vec{J}$, hence $\vec{M} = M\vec{k}$.

Applying Eq. (21) to each term in Eq. (20) and using the formula for the period $T = \frac{2\pi M_0^3}{m\alpha^2}$ [34], one obtains the averaged Hamilton function:

$$\begin{aligned} \bar{H} = mc^2 - \frac{m\alpha^2}{2M_0^2} - \frac{3m\alpha^4}{c^2M_0^3M} + \frac{15m\alpha^4}{8c^2M_0^4} + \frac{2m^2\alpha^4J}{m_0c^2M_0^3M^2} - \\ - \frac{m^3\alpha^4Q}{2m_0M_0^3M^3} - \frac{3m^3\alpha^6Q}{2m_0c^2M_0^3M^5} + \frac{5m^3\alpha^6Q}{4m_0c^2M_0^5M^3}. \end{aligned} \quad (26)$$

As expected, the averaged Hamiltonian depends on the adiabatic invariant M_0 and the orbital angular momentum M . The next step is to find the form of

the angular velocity $\vec{\Omega}$. For this, according to Eq. (7), we need to take the partial derivative of \bar{H} with respect to \vec{M} . The result is the following:

$$\vec{\Omega} = \left(\frac{3m\alpha^4}{c^2M_0^3M^2} - \frac{4m^2\alpha^4J}{m_0c^2M_0^3M^3} + \frac{3m^3\alpha^4Q}{2m_0M_0^3M^4} + \frac{15m^3\alpha^6Q}{2m_0c^2M_0^3M^6} - \frac{15m^3\alpha^6Q}{4m_0c^2M_0^5M^4} \right) \vec{e}_M. \quad (27)$$

Finally, to find the perihelion shift angle Δg , we multiply the angular velocity module $\vec{\Omega}$ by the orbital period T of a test particle. Thereby, we get the form:

$$\begin{aligned} \Delta g = \frac{6\pi Gm_0}{c^2P} - \frac{8\pi GmJ}{c^2MP} + \\ + \frac{3\pi Q}{m_0P^2} + \frac{15\pi GQ(1+e^2)}{2c^2P^3}, \end{aligned} \quad (28)$$

where $P = M^2/m\alpha = a(1 - e^2)$, a is the semi-major axis of the orbit.

From Eq. (28), we can see that for the considered problem the principle of superposition of effects is valid due to the approximate character of the solution as given in terms of the source mass, angular momentum and quadrupole moment. The first term corresponds to the solution of the Schwarzschild problem (i.e., due to the curvature of spacetime caused by the mass of the central body); the second term arises as a result of accounting for the rotation of the source (it appears as the frame dragging effect – the Lense-Thirring effect); the third term is the classical correction due to the quadrupole moment, as a consequence of the source deformation; and the fourth term is the relativistic correction for the quadrupole moment.

It should be noted, that the effect of perihelion shift (rotation) in the Schwarzschild problem is associated with the appearance in the Hamiltonian of the dependence on orbital momentum M . In classical mechanics, i.e., in the Kepler problem,

there is no such dependence and the perihelion remains motionless.

Furthermore, the resulting expression (28) for the perihelion shift in the limits

- $\vec{J} = 0, Q = 0$ reduces to the Schwarzschild case [14, 35];
- $\vec{J} \neq 0 (J^2 = 0), Q = 0$ reduces to the Lense-Thirring effect [14, 35];
- $\vec{J} = 0, Q \neq 0$ reduces to the case c of a static deformed source [36];
- $\vec{J} \neq 0 (J^2 \neq 0), Q \neq 0$ reduces to the case of the external Fock's metric [33].

To be more precise, in the extended Fock metric $Q = \kappa \frac{J^2}{m_0c^2}$, different values of κ , correspond to the following limiting cases (in the $\sim 1/c^2$ approximation):

- at $\kappa = 1$ for the Kerr metric;
- at $\kappa = 4/7$ for the liquid body metric;
- at $\kappa = 15/28$ for the solid body metric.

When comparing, one must keep in mind that in Ref. [14] the angular momentum of the central body is denoted by $S_0 = J$ and quadrupole moment in [36] is denoted by D , which is linked with Q of this work by $Q = -D/2$.

Analysis of the results

Now we apply Eq. (28) to estimate the perihelion shift of the Solar system inner planets: Mercury, Venus and Earth. For calculations, we use the Sun mass, radius, angular momentum and quadrupole moment. The test body is a planet so that its shape and size are not taken into account.

Usually, the quadrupole parameter J_2 is chosen instead of the quadrupole moment Q . There is a straightforward relation between them [35]:

$$J_2 = \frac{Q}{4m_0R^2}, \quad (29)$$

where m_0 , R are the Sun mass and radius, correspondingly. The last experimentally measured value of the solar quadrupole parameter is given in [37] as $J_2 = (2.25 \pm 0.9) \cdot 10^{-7}$. As for the Sun angular momentum, unfortunately, there are no values in the literature based on observational and experimentally studied data. Therefore, to find it, we can use the general formula for the angular momentum [34]:

$$J = I\omega, \quad (30)$$

where ω is the angular velocity of a body rotating around its axis and $I = \frac{2}{5}m_0R^2$ is the moment of inertia of a sphere. It should be noted that the rotation of the Sun is differential, i.e., it decreases with the distance from the equator to the poles. However, as an example, one can choose the value of the angular velocity on the equator $\omega = 2.9 \cdot 10^{-6}$ rad/s [38]. So, the Sun angular momentum is approximately $J = 2.79 \cdot 10^{42}$ kg · m²/s.

Table 1 presents the orbital parameters of Mercury, Venus, and the Earth [39, 40]. Moreover, all the corrections given in Eq. (28) are calculated separately to estimate the individual contribution of each effect. All values are calculated for 100 Earth years.

Table 1 – Orbital parameters and perihelion shift angles of Mercury, Venus, and the Earth

Planets	Mercury	Venus	Earth
Semi-major axis, a (km)	57909082	108208600	149597870
Eccentricity, e	0.2056	0.0068	0.0167
Semilactus rectum, P (km)	55460308	108203681	149556105
Sidereal period, T (earth day)	87.968	224.6950	365.242
$6\pi Gm_0/c^2P$	43''	8.63''	3.84''
$8\pi Gm/c^2MP$	0.116''	0.017''	0.006''
$3\pi Q/m_0P^2$	0.03''	0.003''	0.001''
Observational data	(43.11±0.45)''	(8.4±4.8)''	(5.0±1.2)''

As can be seen from Table 1, the Mercury orbit has the largest value of the perihelion shift. This is due to several factors. Firstly, Mercury is closer than other planets to the Sun and, therefore, is more influenced by its gravitational field. Secondly, Mercury rotates around the Sun faster (in one hundred Earth years, it makes about 415 revolutions, while Venus makes about 162 revolutions, only).

As for Mercury, Venus and the Earth, a significant contribution to the perihelion shift is made by the effect related to the Sun mass. Compared to this, the correction due to the Sun rotation for all three planets has less of an impact; the classical quadrupole moment correction is even less than the latter. In this case, the relativistic quadrupole moment correction $15\pi GQ(1 + e^2)/2c^2P^3$ is negligible in magnitude, so its contribution can be ignored for the Solar system.

The calculated values are in good agreement with the observational data. According to observations, the measurement error for Mercury is 0.45'', for Venus is 4.8'', and for the Earth is 1.2''.

This is due to the fact that the perihelion shift is more certain for orbits with a large eccentricity (as for Mercury). If the orbit is close to circular in shape (as for Venus), it becomes much more difficult to observe the displacement of its perihelion.

Conclusion

In this article, we considered the motion of test particles in the gravitational field of a slowly rotating and slightly deformed object within the framework of the adiabatic theory. For this purpose, the Hartle-Thorne metric was used, expanded in a series in powers of $\sim 1/c^2$, and written in harmonic coordinates.

The perihelion shift expression was derived for the Hartle-Thorne metric. The influence of the central body rotation and deformation on the test particles trajectory was shown. It was also demonstrated that the resulting formula satisfies the principle of superposition of relativistic effects due to the approximate character of the solution as given in terms of the source mass, angular momentum and quadrupole moment. In the limiting cases, the

perihelion shift formula corresponds to the values presented in literature.

As an example, the results of this work were applied to the inner planets of the Solar system. As expected, the main influence on the planets motion is exerted by the curvature of spacetime related to the Sun mass. Although taking into account the Sun rotation and deformation has a minor role, the obtained formula for the perihelion shift can be applied to exoplanetary or other relativistic systems, where their contribution may be more significant.

It would also be interesting to study the motion of test particles in the non-equatorial plane applying both perturbation and adiabatic theories. This task will be considered in future studies.

Acknowledgements

KB, AU and AT acknowledge the Ministry of Education and Science of the Republic of Kazakhstan, Grant: IRN AP08052311.

References

- Schwarzschild, K. "On the Gravitational Field of a Mass Point According to Einstein's Theory". *Sitzungsber. Preuss. Akad. Wiss. Phys.Math.* Vol.1 (1916): 189.
- Misner, C.W., Thorne, K.S., and Wheeler, J.A. *Gravitation*. San Francisco: W.H. Freeman Press, 1973.
- Ohanian, H.C. and Ruffini, R. *Gravitation and Spacetime*, third edition. Cambridge University Press, 2013.
- Lense, J. and Thirring H. *Phys. Z.* Vol.19 (1918): 156.
- Erez, G. and Rosen, N. *Bull. Res. Council Israel F* Vol.8 (1959): 47.
- Hartle, J.B. "Slowly Rotating Relativistic Stars. I. Equations of Structure". *Astrophys. J.* Vol.150 (1967): 1050.
- Hartle, J.B. and Thorne, K.S. "Slowly Rotating Relativistic Stars. II. Models for Neutron Stars and Supermassive Stars". *Astrophys. J.* Vol.153 (1968): 807.
- Berti, E. and Stergioulas, N. "Approximate matching of analytic and numerical solutions for rapidly rotating neutron stars". *Mon. Not. R. Astron. Soc.* Vol.350 (2004): 1416.
- Abishev, M.E., Boshkayev, K. A., Dzhunushaliev, V.D., and Ivashchuk, V.D. "Dilatonic dyon black hole solutions". *Classical and Quantum Gravity* Vol.32, no.16 (2015): 165010.
- Abishev, M.E., Boshkayev, K.A., and Ivashchuk, V.D. "Dilatonic dyon-like black hole solutions in the model with two Abelian gauge fields". *European Physical Journal C* Vol.77, no.3 (2017): 180.
- Belissarova, F.B., Boshkayev, K.A., Ivashchuk, V.D., and Malybayev, A.N. "Special dyon-like black hole solution in the model with two Abelian gauge fields and two scalar fields". *Journal of Physics Conference Series* Vol.1690 (2020): 012143.
- Malybayev, A.N., Boshkayev, K.A., and Ivashchuk, V.D. "Quasinormal modes in the field of a dyon-like dilatonic black hole". *European Physical Journal C* Vol.81, no.5 (2021): 475.
- Abdil'din, M.M. *Mechanics of Einstein's gravitation theory [Mekhanika teorii gravitatsii Ehjnshtejna]*. Alma-Ata: Nauka, 1988 (in Russ).
- Abdil'din, M.M. *The problem of motion of bodies in General Relativity [Problema dvizhenia tel v obshchey teorii otноситel'nosti]*. Almaty: Qazaq Universiteti, 2006 (in Russ).
- Fock, V.A. *Theory of space, time and gravitation*. Pergamon Press – Macmillan Company, 1961.
- Infeld, L. "Equations of Motion in General Relativity Theory and the Action Principle". *Reviews of Modern Physics* Vol.29, no.3 (1957): 398.
- Infeld, L. and Plebanski, E. *Motion and relativism [Dvijenie i relativizm]*. Moskow: Nauka, 1962 (in Russ).
- Tikhonov, A.N. and Samarskii, A.A. *Equations of mathematical physics [Urvnenniia matematicheskoy fiziki]*. Moskow: Nauka, 1977 (in Russ).
- Abramowitz, M. and Stegun, I.A. *Handbook of Mathematical Functions*. Dover Publications, 1972.
- Stergioulas, N. "Rotating Stars in Relativity". *Living Reviews in Relativity* Vol.6, no.1 (2003): 3.
- Boshkayev, K. A., Quevedo, H., Abishev, M.E., Toktarbay, S., and Aimuratov, Ye. K. "Correspondence of Fock and Hartle-Thorne metrics" ["Sootvetstvie metric Foka i Hartla-Torna"]. *News of the National Academy of Sciences of the Republic of Kazakhstan* Vol.4, no.290 (2013):3 (in Russ).

22. Boshkayev, K.A., Suleymanova, Sh.S., Aimuratov, Ye.K., Zhami, B.A., Toktarbay, S., Taukenova, A.S., and Kalymova, Zh.A. “Correspondence of the Kerr and Hartle-Thorne metrics” [“Sootvetstvie metric Kerra i Hartla-Torna”]. *News of the National Academy of Sciences of the Republic of Kazakhstan* Vol.5, no.303 (2015): 151 (in Russ).
23. Boshkayev, K., Quevedo, H., Nurbakyt, G., Malybayev, A., and Urazalina, A. “The Erez-Rosen solution versus the Hartle-Thorne solution”. *Symmetry* Vol.11 (2019): 1324.
24. Boshkayev, K.A., Malybayev, A.N., Quevedo, H., and Nurbakyt, G. “The correspondence of the Erez-Rosen solution with the Hartle Thorne solution in the limiting case of $\sim Q$ and $\sim M^2$ ”. *News of the National Academy of Sciences of the Republic of Kazakhstan* Vol.5, no.333 (2020): 19.
25. Weinberg, S. and Wagoner, R.V. “Gravitation and Cosmology: Principles and Applications of the General Theory of Relativity”. *American Journal of Physics* Vol.41, no.4 (1973): 598.
26. Liu, Q.H. “The Most General Harmonic Coordinates for Kerr Metric”. *Chinese Physics Letters* Vol.15, no.5 (1998): 313.
27. Gielen, S. “Group Field Theory and Its Cosmology in a Matter Reference Frame”. *Universe* Vol.4, no.10 (2018): 103.
28. Galperin, A., Ivanov, E., and Ogievetsky, O. “Harmonic Space and Quaternionic Manifolds”. *Annals of Physics* Vol.230, no.2 (1994): 201.
29. Garfinkle, D. “Numerical Simulations of Generic Singularities”. *Phys. Rev. D* Vol.65 no.4 (2004): 044029.
30. Abramowicz, M.A., Almergren, G.J.E., Kluzniak, W., and Thampan, A.V. “The Hartle-Thorne circular geodesics” // arXiv e-prints gr-qc/0312070 (2003).
31. Bini, D., Boshkayev, K., Ruffini, R., and Siutsou, I. “Equatorial circular geodesics in the Hartle-Thorne spacetime”. *Nuovo Cimento C Geophysics Space Physics C* Vol.36 (2013): 31.
32. Boshkayev, K.A., Quevedo, H., Abutalip, M.S., Kalymova, Zh.A., and Suleymanova Sh.S. “Geodesics in the field of a rotating deformed gravitational source”. *International Journal of Modern Physics A* Vol.31 (2016): 1641006.
33. Boshkayev, K., Quevedo, H., and Ruffini, R. “Gravitational field of compact objects in general relativity”. *Phys. Rev. D* Vol.86, no.6 (2012): 064043.
34. Landau, L.D. and Lifshitz, E.M. *Mechanics*, third edition. Dover Publications, 1976.
35. Landau, L.D. and Lifshitz, E.M. *The classical theory of fields*, fourth edition. Butterworth-Heinemann, 1975.
36. Boshkayev, K.A., Kalymova, Zh.A., Abdualiyeva, B.S., Brisheva, Zh. N., and Taukenova, A.S. “Investigation of a test particle motion in the equatorial plane of the axially symmetric gravitational field in terms of the adiabatic theory” [“Aksialdy-simmetriialy gravitaciialyk oristin ekvatorlyk zhazyktygynda synak denenin kozgalysyn adiabattyk teoriia arkyly zertteu”]. *Recent contributions to physics* Vol.1, no.1 (2018): 64 (in Kaz).
37. Park, R.S., Folkner, W.M., Konopliv, A.S. and et al. “Precession of Mercury’s Perihelion from Ranging to the MESSENGER Spacecraft”. *Astrophysical Journal* Vol.153, no.3 (2017): 121.
38. Kippenhahn, R. and Weigert, A. *Stellar Structure and Evolution*. Springer-Verlag, 1994.
39. Will, C.M. *Theory and experiment in gravitational physics*. Cambridge University Press, 1993.
40. Will, C.M. “The Confrontation between General Relativity and Experiment”. *Living Reviews in Relativity* Vol.9, no.3 (2006): 100.

© This is an open access article under the (CC)BY-NC license (<https://creativecommons.org/licenses/by-nc/4.0/>). Funded by Al-Farabi KazNU.

A.L. Kozlovskiy^{*1,2} , K. Egizbek^{1,2} , K.K. Kadyrzhanov² ¹Institute of Nuclear Physics, Almaty, Kazakhstan²L.N.Gumilyov Eurasian National University, Nur-Sultan, Kazakhstan

*e-mail: kozlovskiy.a@inp.kz

(Received 6 May 2022; received in revised form 26 May 2022; accepted 4 June 2022)

Effect of thermal annealing on phase transformations and ordering of the magnetic texture of Fe₃O₄/Nd₂O₃ nanocomposites

Abstract. The paper presents the results of a study of the effect of thermal annealing on the phase transformations and subsequent ordering of the magnetic texture and superfine magnetic parameters in Fe₃O₄/Nd₂O₃ nanocomposites obtained by chemical deposition and subsequent mechanochemical synthesis. X-ray phase analysis and Mössbauer spectroscopy were used to characterize the properties of the obtained Fe₃O₄/Nd₂O₃ nanocomposites. Thermal annealing was carried out in an oxygen-containing medium in the temperature range of 400°C – 1000°C for 5 hours followed by cooling for 24 hours until reaching room temperature. The phase transformation dynamics of Fe₂O₃/NdFeO₃ → NdFeO₃ >> Fe₂O₃ → NdFeO₃ type was established using X-ray phase analysis. According to the data of Mössbauer spectroscopy it was established that the domination of the NdFeO₃ phase in the nanocomposite structure at annealing temperatures above 800°C leads to an ordering of the magnetic texture and an increase in the value of the superfine magnetic field to 502.8 kE, approaching the values characteristic of the Fe₂O₃ structure (513 kE).

Key words: magnetic nanocomposites, thermal annealing, structural ordering, Mössbauer spectroscopy, phase transformations.

Introduction

One of the important conditions for the practical application of magnetic nanocomposites or nanoparticles as the basis for magnetic sensors, catalysts for the decomposition of organic dyes, or purification of aqueous media from heavy metals is knowledge of the ultrafine magnetic parameters and their correlation between the degree of structural ordering, phase composition, and magnetic characteristics [1-5]. In most cases, the magnetic properties of nanocomposites are strongly dependent on the phase composition, as well as on the presence of disordered regions in the structure related to the processes of particle formation during synthesis. As a rule, the formation of nanostructures proceeds due to non-equilibrium processes and is accompanied by the formation of metastable states, leading to distortion and deformation of the crystal lattice [4-7]. As a result, these deformations lead to the formation of vacancy defects, or voids, in the structure, which negatively affect the domain structure and superfine parameters. Dopants, which are used to modify and enhance the performance of the investigated

composites, also play an important role in the magnetic properties of nanocomposites, especially of complex compositions. The introduction of dopant into the structure may be accompanied by partial substitution of atoms in the lattice nodes, thereby deforming not only the crystal structure, but also changing the magnetic properties and the nearest environment of the atoms [8,9]. As a rule, doping or substitution of atoms occurs during the formation of nanocomposites, including the initiation of phase transformations processes as a result of external influence, one of which is thermal annealing at increased temperatures [10-12].

During thermal annealing, the main effect of changing the properties of materials is associated with a change in the value of thermal vibrations of atoms, which leads to an increase in their mobility and the possibility of filling the voids formed during synthesis with free atoms, which in turn leads to both ordering and the formation of new phases. Moreover, thermal annealing has a great influence on the change in the stoichiometric ratio of the elements at high temperatures, which is associated with a partial displacement of oxygen from the structure, which

leads to an increase in the contributions of metals to the stoichiometry of nanocomposites. Therefore, in spite of the large number of scientific works and previous studies in this direction, there are still many unresolved questions in this direction related to the study of the effect of structural features and phase composition [13-20] changing as a result of thermal annealing in the $\text{Fe}_3\text{O}_4/\text{Nd}_2\text{O}_3$ -based nanocomposites, the interest in which is due to their great potential for application as photocatalysts, absorbents for water purification and biomedical applications, including hyperthermia [15-20].

The aim of this work is to establish the correlation between the degree of structural ordering and phase transformations in $\text{Fe}_3\text{O}_4/\text{Nd}_2\text{O}_3$ nanocomposites with the parameters of the superfine magnetic structure as well as the value of the superfine magnetic field.

Experimental part

The synthesis of $\text{Fe}_3\text{O}_4/\text{Nd}_2\text{O}_3$ nanocomposites was conducted in two stages. The first stage included chemical precipitation of Fe_3O_4 nanoparticles from iron chloride solutions followed by reduction in the form of chemical precipitate, purification from impurities by washing and drying. The second stage consists of mechanochemical mixing of Fe_3O_4 nanoparticles obtained by chemical precipitation with Nd_2O_3 nanoparticles. The mechanochemical synthesis was carried out using a PULVERISETTE 6 planetary mill (Fritsch, Germany), with a grinding speed of 400 rpm and grinding time of 1 hour. For mixing, Fe_3O_4 and Nd_2O_3 were used in a 1:1 ratio. The resulting mixture was removed from the stirring cup made of tungsten carbide and placed in sealed flasks to avoid oxidation processes.

Thermal annealing was chosen to initiate the processes of phase transformations in the synthesized structures, since according to the X-ray phase analysis in the initial state the obtained mixture is an amorphous-like structures without a pronounced crystalline phase. Thermal isochronous annealing was carried out in a SNOL muffle furnace (SNOL, Russia) in the temperature range of 400-1000°C for 5 hours followed by cooling the samples together with the furnace for 24 hours until reaching room temperature. The choice of the temperature range is due to the processes of phase transformations initiated in this range, which makes it possible to study them in more detail.

The phase composition of the investigated $\text{Fe}_3\text{O}_4/\text{Nd}_2\text{O}_3$ nanocomposites was studied by X-ray phase analysis realized on an X-ray diffractometer D8 Advance Eco (Bruker, Germany). Diffractograms were taken in Bragg-Brentano geometry, in the angular range of $2\theta=25-75^\circ$. The diffractograms were interpreted using the Diffrac EVA v.4.2 software code.

The superfine magnetic field parameters of synthesized $\text{Fe}_3\text{O}_4/\text{Nd}_2\text{O}_3$ nanocomposites were studied by Mössbauer spectroscopy. The measurements were carried out on a MS1104Em spectrometer (Rostov-on-Don, Russia). A ^{57}Co source in the Rh matrix was used as a gamma ray source. Mössbauer spectra were taken at room temperature. Decoding was performed using the SpectrRelax software code.

Results and discussion

For the dynamics of phase transformations in $\text{Fe}_3\text{O}_4/\text{Nd}_2\text{O}_3$ nanocomposites as a function of thermal annealing temperature, the X-ray phase analysis method was applied to determine the phase composition of the investigated structures. The change in phase composition reflects the processes of phase transformations as well as the mechanisms accompanying the change in the properties of the materials depending on the conditions of external influences. The results are presented as a series of diffractograms of the studied $\text{Fe}_3\text{O}_4/\text{Nd}_2\text{O}_3$ nanocomposites in Figure 1. The general view of the obtained diffractograms reflects not only the change in the phase composition of the studied structures, but also the processes associated with the deformation and ordering of the crystal structure depending on the annealing temperature. At an annealing temperature of 400°C two phases were observed in the structure of nanocomposites: Fe_2O_3 with a rhombohedral lattice type and NdFeO_3 with an orthorhombic lattice type. The ratio of these phases in the structure is close to the ratio of 1:1. However, the analysis of the shape of the lines indicates a strong disorder of the crystal structure, as well as its unformed and the presence of a large number of amorphous inclusions in the structure. The presence of the Fe_2O_3 phase in the nanocomposite structure is characteristic for phase transformations of the $\text{Fe}_3\text{O}_4 \rightarrow \text{Fe}_2\text{O}_3$ type occurring at sintering temperatures above 300°C. At the same time in the temperature range of 300-500°C this phase is strongly disordered due to the

incompleteness of the phase formation processes. The presence of the NdFeO_3 phase in the structure of nanocomposites is due to the processes of mechanochemical synthesis and subsequent thermal annealing, leading to a partial replacement of iron ions by neodymium ions in the nodes of the crystal lattice, due to the presence of Nd_2O_3 in the structure.

Increasing the annealing temperature to 600°C leads to an increase in the contribution of the NdFeO_3 phase in the structure, which indicates the processes of substitution and partial displacement of the Fe_2O_3 phase. In this case, the $\text{Fe}_2\text{O}_3/\text{NdFeO}_3$ phase ratio according to the X-ray phase analysis is 35/65 with NdFeO_3 dominance. It can also be noted that thermal annealing leads to an increase in the contribution of structural ordering expressed in a change in the shape of diffraction lines and a decrease in their asymmetry, which indicates ordering and a decrease in strain stresses. This ordering is due to the processes of thermal annealing of point defects and filling of

vacancies, as well as a change in the ratio of phases in the composite under study, which indicates an ordering of the structure.

At a temperature of 800°C the process of phase transformations of the type $\text{NdFeO}_3 \gg \text{Fe}_2\text{O}_3 \rightarrow \text{NdFeO}_3$ ends with the complete dominance of the NdFeO_3 phase and the displacement of the Fe_2O_3 phase. Meanwhile, changes in the shape of the diffraction lines, indicating ordering of the structure, are also observed. This process is due to the fact that for magnetic nanoparticles based on iron oxide, at temperatures above 600°C the processes of phase transformations stop, and further change in annealing temperature leads only to structural ordering accompanied by enlargement of particle size and change in their geometry. In this connection, the presented results of X-ray diffraction of the studied samples at 1000°C indicate ordering processes, and are expressed in clear symmetric diffraction reflexes, characteristic of highly ordered crystal structures.

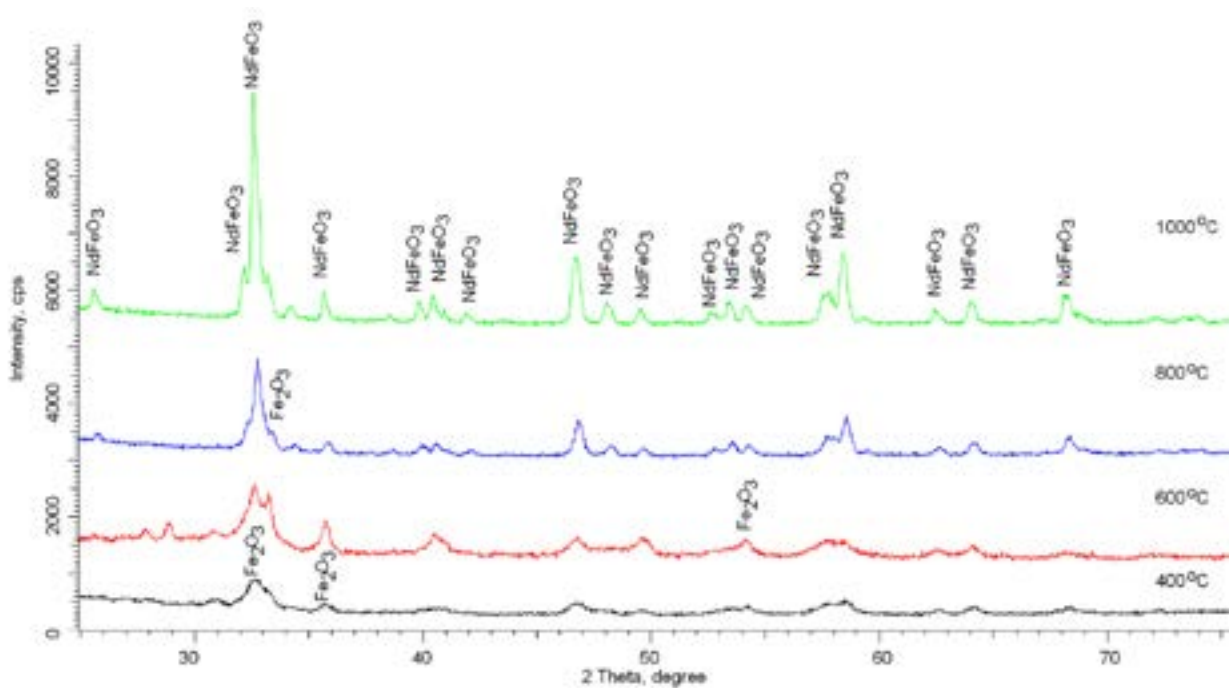


Figure 1 – Dynamics of X-ray diffractograms of the studied $\text{Fe}_3\text{O}_4/\text{Nd}_2\text{O}_3$ nanocomposites.

Figure 2 shows the results of measuring Mössbauer spectra of the studied $\text{Fe}_3\text{O}_4/\text{Nd}_2\text{O}_3$ nanocomposites obtained by mechanochemical synthesis by grinding the initial components in the ratio 1:1 and subsequent thermal isochronous annealing in the temperature range of $400\text{--}1000^\circ\text{C}$ for

5 hours. According to the general concepts, the obtained spectra can be characterized by the presence of a quadrupole doublet, characteristic of the disordered structure, and a Zeeman sextet, characterizing the magnetically ordered component of nanocomposites.

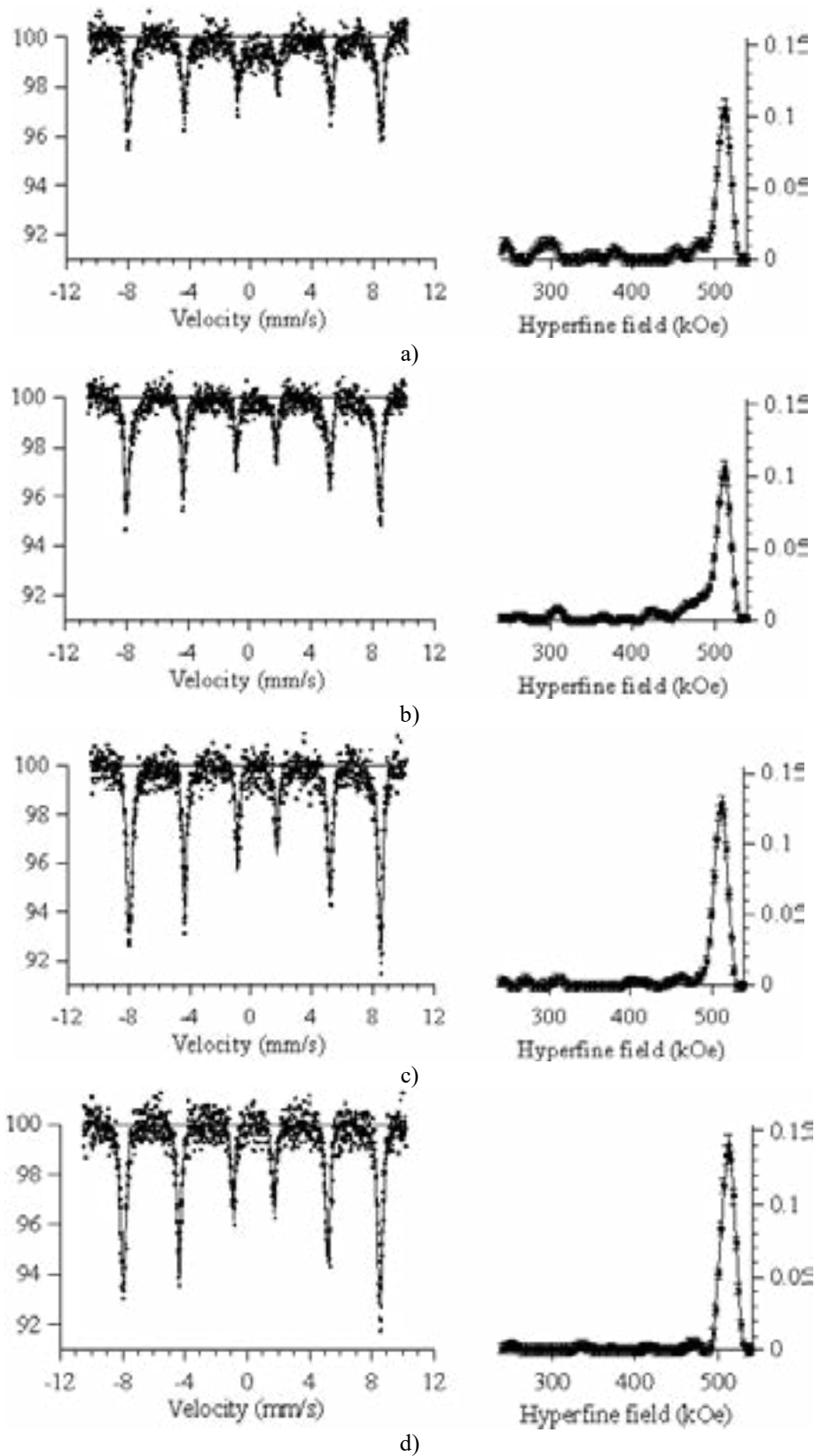


Figure 2 – Mössbauer spectroscopy results of the samples annealed at different temperatures: (a) 400°C; (b) 600°C; (c) 800°C; (d) 1000°C.

The general appearance of the obtained spectra depending on the annealing temperature is characterized by two types of changes. The first type is characterized by changes in the intensities of the partial spectra lines characteristic of the doublet and sextet, which indicates changes in the intensities of the contributions characteristic of the ordered and disordered magnetic structure in nanocomposites. This behavior is caused by a change in the concentration of point defects in the structure due to their partial annealing and subsequent annihilation, which leads to an ordering of the structure. Figure 3 shows the results of changes in the contribution intensities for the doublet and sextet as a function of the annealing temperature of the nanocomposites.

As can be seen from the presented data, an increase in the annealing temperature of nanocomposites leads to an increase in the contribution of the zeeman sextet characteristic of an

ordered magnetic structure, while at temperatures above 800°C a complete displacement of the quadrupole doublet is observed, which indicates structure ordering, and the absence of disordered areas related to amorphization or destruction of samples. The second type of changes is associated with changes in the shape and width of spectral lines, indicating ordering of the superfine magnetic parameters with increasing structural ordering of the synthesized composites. The decrease in the contribution from the quadrupole doublet characteristic of the disordered regions confirms the results of the X-ray phase analysis of the investigated samples.

Figure 4 shows the results of the relationship between the magnitude of structural ordering according to X-ray diffraction data and the ratio of intensities ($I_{doublet}/I_{sextet}$), which characterizes the degree of magnetic ordering in the structure.

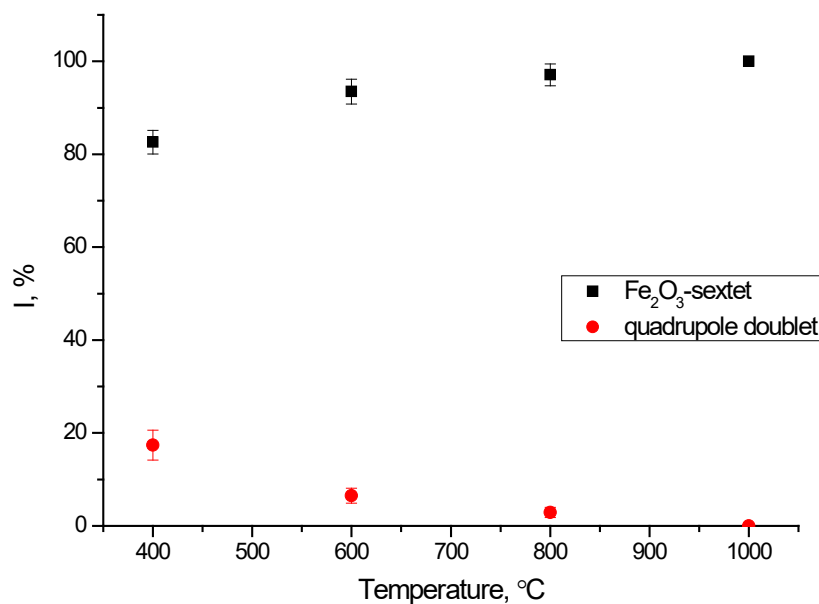


Figure 3 – Change of the ratio of Zeeman sextet and quadrupole doublet intensities.

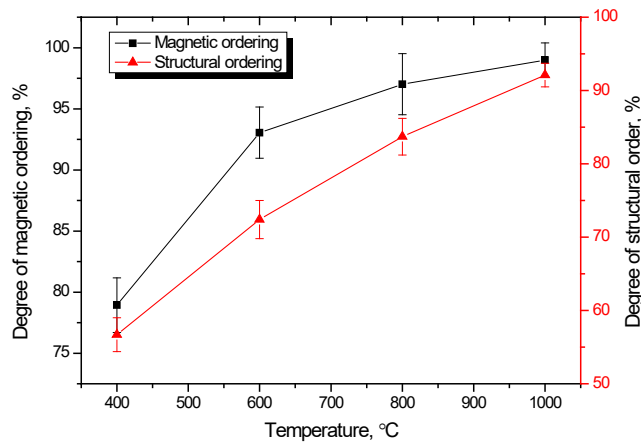


Figure 4 – Results of changes in the values of structural and magnetic ordering.

As can be seen from the presented data, an increase in the annealing temperature leads to structural and magnetic ordering by a similar mechanism, consisting in the fact that a decrease in the defect fraction in the structure due to substitution processes and subsequent formation of the NdFeO_3 phase leads to an increase in the degree of crystallinity and a decrease in amorphous inclusions in the structure. In turn, the reduction of the contribution in the Mössbauer spectra of the quadrupole

doublet, which is characteristic of the paramagnetic state of the substance, indicates an ordering of the magnetic texture, as well as a change in the value characteristic of the superfine magnetic field. Figure 5 shows the results of the relationship between the change in the value of the structural ordering of the crystal lattice of the phases under study and the value of the superfine magnetic field characteristic of the Zeeman sextet.

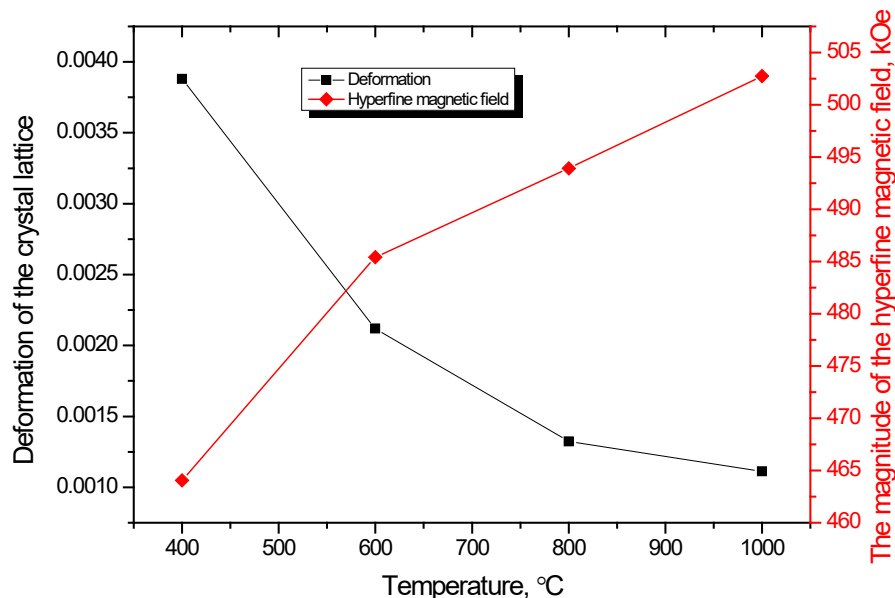


Figure 5 – Results of crystal lattice deformation and superfine magnetic field values.

From the data presented in Figure 5 it can be seen that the decrease in the lattice deformation is more pronounced in the temperature range 400-800°C, which is characteristic of the phase ordering and displacement of the Fe_2O_3 phase and the subsequent

dominance of the NdFeO_3 phase. Meanwhile, in the temperature range of 800-1000°C the deformation contribution reduction is insignificant, which indicates the reduction of the deformation contribution in the structure, as well as the

completion of the phase transformations and subsequent transformations. At the same time, the change in the phase composition of nanocomposites leads to an increase in the value of the superfine magnetic field, which also indicates the ordering of the magnetic textures of samples.

Conclusion

This article is devoted to the study of the correlation between structural and magnetic ordering as a result of phase transformations in $\text{Fe}_3\text{O}_4/\text{Nd}_2\text{O}_3$ nanocomposites initiated by thermal annealing in the temperature range 400-1000°C. With the method of X-ray phase analysis the dynamics of phase transformations of the type $\text{Fe}_2\text{O}_3/\text{NdFeO}_3 \rightarrow \text{NdFeO}_3 \gg \text{Fe}_2\text{O}_3 \rightarrow \text{NdFeO}_3$ was established. The kinetics of the contributions change for the Zeeman sextet, which is typical of the structurally ordered magnetic phase, and the quadrupole doublet corresponding to the disordered regions and amorphous inclusions in the structure of $\text{Fe}_3\text{O}_4/\text{Nd}_2\text{O}_3$ nanocomposites have been established as a result of the investigations. It was determined that the quadrupole doublet contribution is completely displaced at annealing temperatures above 800°C, which corresponds to the ordering of the crystal structure and superfine magnetic parameters.

Further research will be aimed at studying the corrosion resistance of the synthesized nanostructures in order to determine their resistance to external influences.

Acknowledgments

This study was funded by the Ministry of Education and Science of the Republic of Kazakhstan (Grant No. AP09259184).

References

1. Liu, Xudong, et al. "Synthesis of covalently bonded reduced graphene oxide- Fe_3O_4 nanocomposites for efficient electromagnetic wave absorption." *Journal of Materials Science & Technology* 72 (2021): 93-103.
2. Du, Guan-Hua, et al. "Characterization and application of $\text{Fe}_3\text{O}_4/\text{SiO}_2$ nanocomposites." *Journal of Sol-Gel Science and Technology* 39.3 (2006): 285-291.
3. Tuo, Ya, et al. "Microbial synthesis of $\text{Pd}/\text{Fe}_3\text{O}_4$, $\text{Au}/\text{Fe}_3\text{O}_4$ and $\text{PdAu}/\text{Fe}_3\text{O}_4$ nanocomposites for catalytic reduction of nitroaromatic compounds." *Scientific reports* 5.1 (2015): 1-12.
4. Su, Jing, et al. " Fe_3O_4 -graphene nanocomposites with improved lithium storage and magnetism properties." *The Journal of Physical Chemistry C* 115.30 (2011): 14469-14477.
5. Khandanlou, Roshanak, et al. "Synthesis and characterization of rice straw/ Fe_3O_4 nanocomposites by a quick precipitation method." *Molecules* 18.6 (2013): 6597-6607.
6. Mahmoodabadi, A. Nayamadi, Ahmad Kompany, and Mansour Mashreghi. "Characterization, antibacterial and cytotoxicity studies of graphene- Fe_3O_4 nanocomposites and Fe_3O_4 nanoparticles synthesized by a facile solvothermal method." *Materials Chemistry and Physics* 213 (2018): 285-294.
7. Unal, B., et al. "Synthesis, structural and conductivity characterization of alginate- Fe_3O_4 nanocomposite." *Journal of nanoparticle research* 12.8 (2010): 3039-3048.
8. Kiziltaş, Hakan, Taner Tekin, and Derya Tekin. "Preparation and characterization of recyclable $\text{Fe}_3\text{O}_4@ \text{SiO}_2@ \text{TiO}_2$ composite photocatalyst, and investigation of the photocatalytic activity." *Chemical Engineering Communications* 208.7 (2021): 1041-1053.
9. Zhu, Kai, et al. "Chemical synthesis and coercivity enhancement of $\text{Nd}_2\text{Fe}_{14}\text{B}$ nanostructures mediated by non-magnetic layer." *Nano Research* 13.4 (2020): 1141-1148.
10. Kozlovskiy, A. L., et al. "Study of structural features and phase transformations in nanocomposites of $\text{Fe}_2\text{O}_3@ \text{NdFeO}_3$ type." *Journal of Materials Science: Materials in Electronics* 32.16 (2021): 21237-21247.
11. Khammarnia, Somaye, et al. "Enhanced catalytic activity of Pt-NdFeO_3 nanoparticles supported on polyaniline-chitosan composite towards methanol electro-oxidation reaction." *Journal of Nanostructures* 10.2 (2020): 239-257.
12. Yavari, Zahra, Meissam Noroozifar, and Mozghan Khorasani-Motlagh. "Presentation of anodic electrocatalyst for polymeric fuel cell: Pt nanoparticles immobilized on NdFeO_3 nanocrystals and carbon nanotubes." *Indian Journal of Chemical Technology (IJCT)* 26.1 (2019): 9-22.
13. Anajafi, Z., et al. " NdFeO_3 as a new electrocatalytic material for the electrochemical

monitoring of dopamine." *Analytical and bioanalytical chemistry* 411.29 (2019): 7681-7688.

14. Atta, Nada F., H. Ekram, and Ahmed Galal. "Evidence of core-shell formation between NdFeO₃ nano-perovskite and ionic liquid crystal and its application in electrochemical sensing of metoclopramide." *Journal of The Electrochemical Society* 163.7 (2016): B325.

15. Aparnadevi, N., et al. "Room temperature dual ferroic behaviour of ball mill synthesized NdFeO₃ orthoferrite." *Journal of Applied Physics* 120.3 (2016): 034101.

16. Atta, Nada F., et al. "Electrochemical sensing platform based on nano-perovskite/glycine/carbon composite for amlodipine and ascorbic acid drugs." *Electroanalysis* 31.3 (2019): 448-460.

17. Somvanshi, Anand, et al. "Structural modifications and enhanced ferroelectric nature of NdFeO₃-PbTiO₃ composites." *Applied Physics A* 127.6 (2021): 1-18.

18. Nguyen, Tien Anh, et al. "Co-doped NdFeO₃ nanoparticles: synthesis, optical and magnetic properties study." *Nanomaterials* 11.4 (2021): 937.

19. Yousefi, Mostafa, S. Zeid, and M. Khorasani-Motlagh. "Synthesis and characterization of nanostructured perovskite type neodymium orthoferrite NdFeO₃." *Current Chemistry Letters* 6.1 (2017): 23-30.

20. Mathur, Sanjay, et al. "Nanocrystalline orthoferrite GdFeO₃ from a novel heterobimetallic precursor." *Advanced Materials* 14.19 (2002): 1405-1409.

© This is an open access article under the (CC)BY-NC license (<https://creativecommons.org/licenses/by-nc/4.0/>). Funded by Al-Farabi KazNU.

Y. Myrzakulov^{1,2} , A. Sharlez¹ , D. Kenzhalin¹ ,
S. Myrzakul^{1,2,*} , G. Yergaliyeva¹ 

¹L.N.Gumilyov Eurasian National University, Nur-Sultan, Kazakhstan

²«Ratbay Myrzakulov Eurasian International Centre for Theoretical Physics» LLP, Nur-Sultan, Kazakhstan

*e-mail: smyrzakul@gmail.com

(Received 11 March 2022; received in revised form 18 May 2022; accepted 30 May 2022)

Starobinsky model with a viscous fluid

Abstract. The article considers some cosmological solutions of the Starobinsky model for a flat inhomogeneous viscous Universe. The first section contains a brief of the $F(R)$ theory of gravity. One of the most common examples of $F(R)$ gravity with a high degree of curvature is the Starobinsky model. For the Starobinsky $F(R) = \alpha R + \beta R^2$ model, the cosmological model of a flat and homogeneous Universe is considered. For the Friedmann-Robertson-Walker metric, the Lagrange function is defined, and the corresponding equations are determined by the Euler-Lagrange equations and the Hamilton energy condition. Using the equation of state for inhomogeneous viscous fluid, we considered two cases of the viscosity parameter when the state parameter is constant. Next, using the results obtained, we determined the dynamics of the Hubble parameter H . At constant viscosity, $\xi = \xi_0$ has a negative value of the Hubble parameter and decreases with time along a hyperbola, while $\xi = 3H$ has a positive value decreases along a hyperbola.

If we compare it with the well-known de Sitter solution describing the accelerated expansion of the Universe and take into account that time in physics should only be positive, then the change in the Hubble parameter for the viscosity $\xi = 3H$ occurs later. An analysis of this solution shows that at a certain point in time the acceleration of the Universe turns into a process of instantaneous compression. However, at the end, the result is similar to the de Sitter solution tends to zero, i.e. the Universe stops accelerating. Based on the results obtained, a graph was constructed with respect to the de Sitter solution. The analysis was carried out according to the graph. These results are useful for describing the accelerated expansion of the modern Universe and do not contradict modern astronomical observations.

Key words: viscous fluid, cosmology, Starobinsky model, FRW metric, $F(R)$ gravity.

Introduction

The general theory of relativity is the basic theory describing gravitational phenomena in nature. The correctness of this theory is confirmed by various experiments and observations. However, the general theory of relativity does not fully describe some aspects of the evolution of the Universe, for example, the current accelerated expansion of the Universe [1, 2]. The best theory to explain this expansion of the Universe is dark energy [3-5], but the nature of dark energy is still unknown.

The latest cosmological data limit the state parameter ω of dark energy to $\omega = -0.972 + 0.061 - 0.060$ so that various forms of dark fluid (phantom, quintessence, inhomogeneous fluids, etc.) can satisfy the corresponding equation of state. The study of non-ideal fluids in the Friedman-Robertson-Walker (FRW) universe can be justified by various arguments. First of all, even though many macroscopic physical systems, such as the large-scale structure of baryonic matter and radiation in the Universe, can be approximated as ideal fluids (with the equation of state $p = \omega\rho$, ω is constant), the description of dark energy does not

exclude a more complex equation of state, since its nature is still unknown.

Moreover, interest in modified theories of gravity has increased in recent years. Such theories suggest changing not only the nature of dark energy, but also a different approach to Einstein's spacetime or gravity by replacing the curvature of spacetime in the classical Hilbert-Einstein formula with more generalized variants (Riemann tensor, Weyl tensor, Ricci tensor, etc.). One of the most common examples of modified gravity is the model Starobinsky. Various applications of Starobinsky models in cosmology are presented in the literature [17].

In this paper, we study the dynamics of a viscous fluid [18-20] in the Starobin gravitational field. The corresponding equations of motion are determined and the evolution of the Hubble parameter for two types of viscous fluids is obtained. Moreover, the results obtained are compared with de Sitter's solution and allow us to describe the late evolution of the universe.

It should be noted that we fully adopt the natural system of units by taking $8\pi G=c=h=1$. Indices i,j,l run from 1 to 4 throughout this paper.

Action and equations of motion

In this section, we consider the Starobinsky model for FRW metric. In the general case, the action $F(R)$ gravity can be written as follows

$$S = \int d^4x \sqrt{-g} \left(\frac{1}{2k} F(R) + L_m \right), \quad (1)$$

where $k = \frac{8\pi G}{c^4}$, g is the determinant of the metric tensor $g_{\mu\nu}$, $F(R)$ is some function of the Ricci scalar R , L_m is the Lagrangian matter. The dependence of the function $F(R)$ on the Ricci scalar is given in this paper similarly to the Starobinsky model $F(R) = \alpha R + \beta R^2$, where $\alpha, \beta = \text{const}$.

Then consider the FRW metric with action (1)

$$ds^2 = -dt^2 + a^2(t)(dx^2 + dy^2 + dz^2), \quad (2)$$

where $a(t)$ is a scale factor that depends only on time t . For this metric, we obtain the following equations

$$\sqrt{-g} = a^3, \quad R = 6 \left(\frac{\ddot{a}}{a} + \frac{\dot{a}^2}{a^2} \right),$$

where the dot denotes the differentiation in time t .

Therefore, for metric (2) action (1) can be rewritten as follows

$$S = \int d^4x a^3 \left[\alpha R + \beta R^2 - \lambda \left(R - 6 \frac{\ddot{a}}{a} - 6 \frac{\dot{a}^2}{a^2} \right) \right]. \quad (3)$$

If we take a variation of this action with respect to R , we can determine the Lagrange multiplier λ

$$\lambda = \frac{dF(R)}{dR} = \alpha + 2\beta R.$$

Thus, we can write the point-like Lagrangian as follows

$$L = \beta R^2 a^3 + 12a^2 \dot{a} \beta \dot{R} + 6(\alpha + 2\beta R) a \dot{a}^2. \quad (4)$$

Using the Euler-Lagrange equation, we find the pressure for the considered model as follows

$$p = -2\dot{H} - 3H^2 = \frac{-\frac{\beta R^2}{2} + 2\beta \ddot{R} + 4\beta \dot{R}H}{\alpha + 2\beta R}. \quad (5)$$

Using the energy condition, we define our energy density as follows

$$\rho = 3H^2 = \frac{R^2 \beta}{2(\alpha + 2\beta R)} - \frac{6H\beta \dot{R}}{\alpha + 2\beta R}, \quad (6)$$

where $H = \frac{\dot{a}}{a}$ is the Hubble parameter.

If we equate equations (5) and (6), we obtain the following equation

$$\dot{R} - \frac{1}{12H} R^2 + HR + \frac{\alpha}{2\beta} H = 0. \quad (7)$$

Model of inhomogeneous viscous fluid

The pressure p introduced into the Friedmann equations and the energy density ρ must satisfy the following conservation law

$$\dot{\rho} + 3H(\rho + p) = 0. \tag{8}$$

For our model, we study the general form of the equation of state for an inhomogeneous viscous fluid [17-20]

$$p = \omega(\rho)\rho - B(a(t), H, \dot{H}, \dots), \tag{9}$$

where $\omega(\rho)$ parameter of the equation of state can depend on the energy density, and the mass viscosity $B(a(t), H, \dot{H}, \dots)$ is a function of its arguments. Consider $B(a(t), H, \dot{H}, \dots) = \xi(H)$ for a viscous fluid

$$p = \omega(\rho) - 3H\xi(H), \tag{10}$$

thus, $\xi(H)$ – is the bulk viscosity.

Thus, if we substitute the pressure in equation (5) to the law of conservation of energy (6), we will obtain an additional equation of motion describing a viscous fluid. As a result, we obtain a system of equations of motion

$$\dot{\rho} + 3H\rho(1 + \omega(\rho)) = 3H\xi(H), \tag{11}$$

$$\rho = 3H^2 = \frac{\beta R^2 - 6H\beta\dot{R}}{\alpha + 2\beta R}, \tag{12}$$

$$R = 6\dot{H} + 12H^2, \tag{13}$$

$$p = -2\dot{H} + 3H^2 = \frac{\left(-\frac{\beta R^2}{2} + 2\beta\ddot{R} + 4\beta\dot{R}\right)}{(\alpha + 2\beta R)}. \tag{14}$$

Now consider two cases related to these given equations of motion. Let's transform these received formulas.

Cosmological solution

For thermodynamic reasons $\xi(H)$ is usually chosen to be positive. Therefore, various forms of viscosity can be used to numerically or accurately solve the Hubble parameter. Next, consider two types of viscosity parameter $\xi(H)$.

First case: $\omega = const$, $\xi(H) = const$

In this case, for $\xi(H) = \xi_0 = const$, we obtain the following equation using equations (11)-(14)

$$\dot{H} = -\frac{3}{2}(\omega + 1)H^2 + 3\xi_0H, \tag{15}$$

as a result, we get the following solution

$$H = \frac{2\xi_0}{1 + \omega - e^{-3\xi_0(t-t_0)}}. \tag{16}$$

If we consider $\omega = -1$ and the early Universe for vacuum, then the time $t_0 \cong 0$, i.e.

$$H = -\frac{2\xi_0}{e^{-3\xi_0 t}}, \tag{17}$$

Having determined the dependence of the scalar curvature on time, substituting this solution (13) and solving equation (7) $\alpha = 1$, $\beta = 1$, $\xi_0 = 1$, we determine the Hubble parameter for the Starobinsky model

$$H = -10 \frac{\left(-18e^{-3t} + \sqrt{6}\sqrt{e^{-3t}(55e^{-3t} - 120)}\right)e^{3t}}{-120 + e^{-3t}}. \tag{18}$$

Second case: $\omega = const$, $\xi = 3H$

Consider the case where the equation of state parameter for vacuum is $\omega = -1$ and the bulk viscosity depends only on the Hubble parameter, then

$$H = \frac{2}{3(\omega - 2)(t - t_0)}. \tag{19}$$

After some actions, analogous to the previous case, we define the Hubble parameter for the Starobinsky model

$$H = -\frac{2}{3} \frac{-12 + 12t + \sqrt{24t^4 - 152t^3 + 342t^2 - 384t + 160}}{(3t^2 - 16t + 8)t} \tag{20}$$

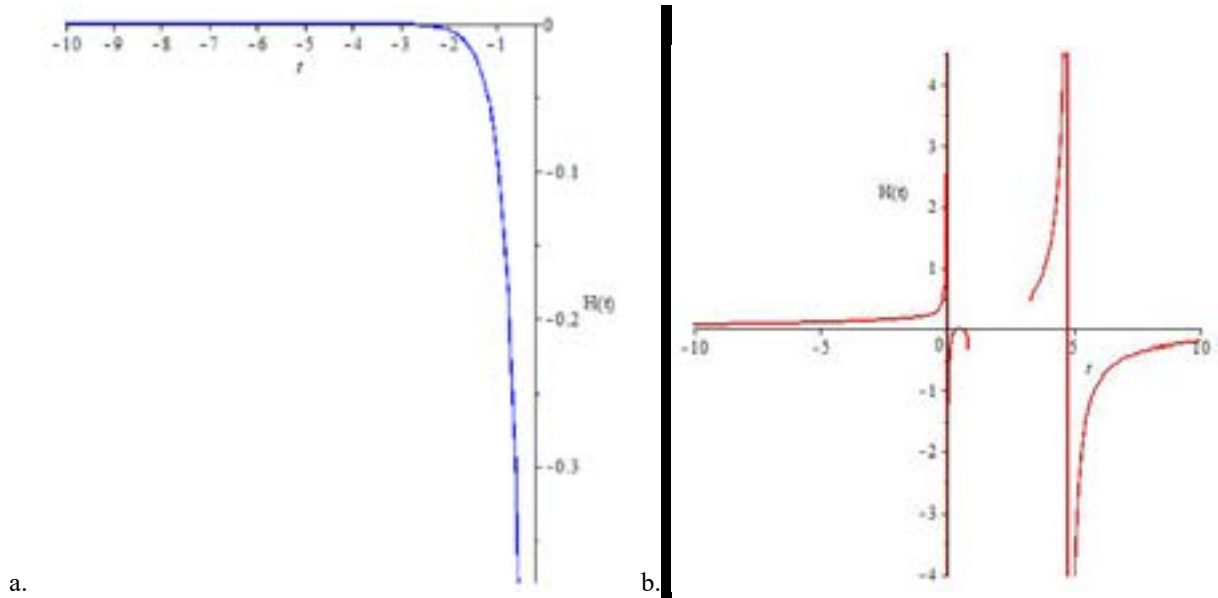


Figure 1 – Hubble parameter dynamics for cases: a. $\xi = \xi_0$, b. $\xi = 3H$

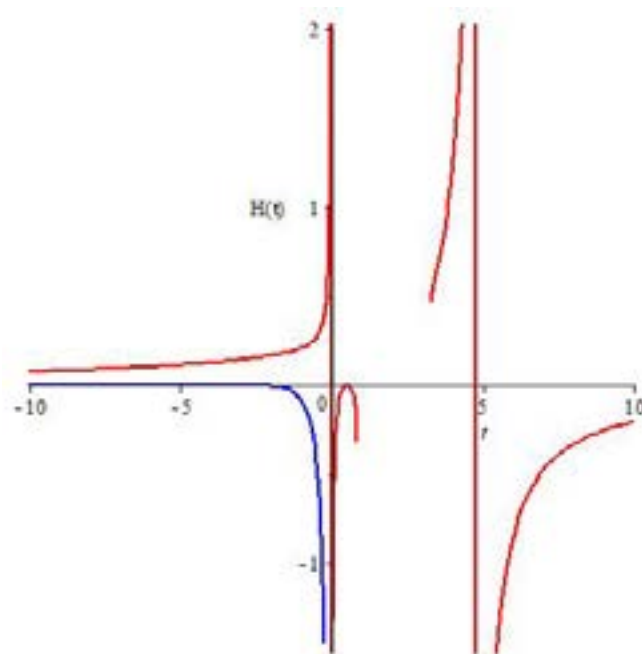


Figure 2 – Dynamics of the Hubble parameter for different solutions for $\xi = \xi_0$ indicated by a blue line, for $\xi = 3H$ red line.

Conclusion

Thus, in this work, we have considered some cosmological solutions of the Starobinsky model for the flat and homogeneous Universe. In the first section we give a brief introduction to the theory of gravitation. For the FRW metric, the Lagrange function is defined, and the corresponding equations of motion are determined using the Euler-Lagrange equations and the Hamilton energy condition. As you can see, these equations are non-linear differential equations of high order, the solution of which is a difficult task. Next, using this result, we determined the Hubble parameter H and the equation of motion R .

Finally, as you can see in Fig. 2, the Hubble parameter is negative for the $\xi = \xi_0$ condition and decreases with time along the hyperbola, while in the $\xi = 3H$ state it decreases to a positive value along the hyperbola. If we compare with the well-known de Sitter solution describing accelerated expansion that time is only positive according to the law of physics, then in the case of $\xi = 3H$ the Hubble change occurs later than the de Sitter solution, and the viscosity is $\xi \neq \xi_0$ variable. If we analyze the solution for a viscosity proportional to the Hubble parameter, then at a certain moment in time the acceleration of the Universe passes into the process of instantaneous compression. But as a result, the de Sitter solution seems to be infinitely close to zero, that is, the Universe stops accelerating.

Acknowledgements

The research work is supported by the grant project AP08052197 (2020-2022) from the Ministry of Science and Education of the Republic of Kazakhstan.

References

1. Perlmutter, S. et al. "Measurements of omega and lambda from 42 high-redshift supernovae." *The Astrophysical Journal* 517. (1999): 565-586.
2. Riess, A. et al. (1998) "Observational evidence from supernovae for an accelerating universe and a cosmological constant." *The Astrophysical Journal* 116 (1998):1009-1038.
3. Peebles, P.J.E., Ratra, B. "The cosmological constant and dark energy." *Reviews of Modern Physics* 75. (2003):559-606.
4. Copeland, E.J., Sami, M., Tsujikawa, S. "Dynamics of dark energy." *International Journal of Modern Physics D* 15. (2006):1753.
5. Chechin, L.M., Myrzakul, S.R. "The development of perturbations in the universe described by the nonstationary equation of state" *Russian Physics Journal* 52(3). (2009): 286–293
6. Myrzakul, S., Imankul, M., Arzimbetova, M., Myrzakul, T. R., F(T) gravity with scalar field viscous fluid" *Journal of Physics Conference Series* 1730. (2021): 012021.
7. Bamba, K., Lopez-Revelles, A., Myrzakulov, R., Odintsov, S. D., Sebastiani, L. "The universe evolution in exponential F(R)-gravity" *TSPU Bulletin* 2012 13. (2012): 22-27.
8. Razina, O.V., Tsyba, P.Yu., Myrzakulov, R., Meirbekov, B., Shanina, Z. "Cosmological Yang-Mills model with k-essence" *Journal of Physics: Conference Series* 1391(1). (2019): 012164.
9. Razina, O.V., Tsyba, P.Yu., Suikimbayeva, N. "Tachyonization Cosmological Model in the Framework of Linear Form-Invariance Transformations" *Eurasian Physical Technical Journal* 18(3). (2021): 93–100.
10. Tsyba, P., Razina, O., Suikimbayeva, N. "Analysis of cosmological tachyon and fermion model and observation data constraints" *International Journal of Modern Physics D* 30(15). (2021): 2150114.
11. Brevik, I., Myrzakulov K., Timoshkin, A. V., Zhadyranova, A. "Viscous coupled fluids in terms of a log-corrected equation-of-state" *International Journal of Geometric Methods in Modern Physics* 18(12). (2021): 2150198.
12. Razina, O., Myrzakulov, Y., Serikbayev, N., Myrzakul, S., "G-essence cosmologies with scalar-fermion interactions" *European Physical Journal Plus*, 2011, 126(9), стр. 1–5, 858 Khurshudyan, M., Chubaryan, E., Pourhassan, B. "Interacting Quintessence Models of Dark Energy" *International Journal of Theoretical Physics* 53. (2014):2370-2378.
13. Myrzakul, S., Myrzakulov, R., Sebastiani, L. "Coupled fluids model in FRW space-time" *Astrophysics and Space Science* 353(2). (2014):667–675.

14. Myrzakul, S., Myrzakulov, R., Sebastiani, L. “k -essence in Horndeski models.” *Astrophysics and Space Science* 361(8). (2016): 254.
15. Sebastiani, L., Myrzakul, S., Myrzakulov, R. “Reconstruction of k-essence inflation in Horndeski gravity” *European Physical Journal Plus*. 132(10). (2017): 433.
16. Jamil, M., Momeni, D., Serikbayev, N.S., Myrzakulov, R. “FRW and Bianchi type I cosmology of f -essence” *Astrophysics and Space Science* 339. (2012):37.
17. Myrzakul, S., Belisarova, F.B., Myrzakul, T., Myrzakulov K. “Dynamics of f -essence in frame of the starobinsky model” *News of the National Academy of Sciences of the Republic of Kazakhstan. Physical-mathematical series*. 5(315) (2017): 143-148.
18. Myrzakul, S., Myrzakulov, R., Sebastiani, L. “Inhomogeneous viscous fluids in FRW universe and finite-future time singularities” *Astrophysics and Space Science* 350(2). (2014): 845-853.
19. Myrzakul, S., Myrzakulov, R., Sebastiani, L. “Inhomogeneous fluids for warm inflation” *Astrophysics and Space Science* 357(2). (2015): 168.
20. Myrzakul, S., Arzimbetova, M., Imankul M., Myrzakulov, R. “Cosmology of f -essence with inhomogeneous viscous fluid” *Journal of Physics Conference Series* 1391. (2019): 012167.

© This is an open access article under the (CC)BY-NC license (<https://creativecommons.org/licenses/by-nc/4.0/>). Funded by Al-Farabi KazNU.

Contents

Editorial.....	3
B. Rysbaiuly, S.D. Alpar Experimental Data and the Nonlinear Inverse Problem of Heat Transfer	4
G.T. Balakayeva, Paul Ezhichelvan, M.K. Tursynkozha Analysis, Research and Development of an Innovative Enterprise Digitalization System for Remote Work	19
G.A. Ashirova, A.K. Manapova, A.O. Beketaeva Numerical Simulation of Particle Dynamics in the Hydrogen-Air Mixing Layer	30
Kh. Khompysh, A.A. Kabidoldanova An Initial-Boundary Value Problem for Kelvin-Voigt Equations with $(p(x), q(x) \delta m(x))$ Structure	41
D.B. Zhakebayev, A.S. Zhumali Simulation of Ternary Fluid Mixtures Separation by Phase-Field Free Energy LBM	48
M. Odsuren, G. Khuukhenkhuu, Ch. Saikhanbayar, S. Davaa, O. Odgerel, N. Baljinnyam Scattering phase shifts of lithium isotopes.....	55
Hayam F. Darweesh, Essam M. Abulwafa, Atalla M. El-Hanbaly Arbitrary amplitude nonlinear waves in a four-component quantum plasma.....	60
P.F. Kashaykin, E.A. Pospelova, I.E. Kenzhina, Zh.A. Zaurbekova, S.K. Askerbekov, M.Yu. Salgansky, A.A. Shaimerdenov, A.U. Tolenova, A.L. Tomashuk Gamma-radiation-induced attenuation of light in pure-silica core optical fiber in long-wavelength region.....	75
G.B. Suliyeva, K.A. Boshkayev, G. Nurbakyt, H. Quevedo, A.S. Taukenova, A.T. Tlemissov, Zh.A. Tlemissova, A. Urazalina Adiabatic theory of motion of bodies in the hartle-thorne spacetime.....	82
A.L. Kozlovskiy, K. Egizbek, K.K. Kadyrzhanov Effect of thermal annealing on phase transformations and ordering of the magnetic texture of Fe ₃ O ₄ /Nd ₂ O ₃ nanocomposites	91
Y. Myrzakulov, A. Sharlez, D. Kenzhalin, S. Myrzakul, G. Yergaliyeva Starobinsky model with a viscous fluid	99